SCALING SILICON NANOPHOTONIC INTERCONNECTS : SILICON ELECTROOPTIC MODULATORS, SLOWLIGHT & OPTOMECHANICAL DEVICES

by Sasikanth Manipatruni

SCALING SILICON NANOPHOTONIC INTERCONNECTS : SILICON ELECTROOPTIC MODULATORS, SLOWLIGHT & OPTOMECHANICAL DEVICES

A Dissertation
Presented to the Faculty of the Graduate School
of Cornell University
In Partial Fulfillment of the Requirements for the Degree of
Doctor of Philosophy

by
Sasikanth Manipatruni
August 2010

SCALING SILICON NANOPHOTONIC INTERCONNECTS: HIGH SPEED SILICON MICRO-RING MODULATORS, SLOW LIGHT & OPTO-MECHANICAL DEVICES

Sasikanth Manipatruni, Ph. D.
Cornell University 2010

The ability to manipulate light has enabled robust growth of communications over the past 50 years. The energy spent by interconnects is now a major consideration for high performance computing, datacom servers and low carbon footprint telecommunications. Hence, it is of great interest to pursue novel devices for manipulating light. Silicon nanophotonics, which is the exploration of optical devices based in silicon compatible materials, has emerged as a powerful solution for providing the bandwidth for future communications. This thesis attempts at scaling the silicon nanophotonic interconnects to meet the future needs.

The first key result of my thesis is an 18 Gbit/s micro-ring modulator. This is the fastest digital modulation speed shown in silicon micro-rings to date. In the first section of this thesis, I will show how to achieve very high speed modulation in silicon substrates using silicon micro-ring modulators. In the effort to optimize their performance I have shown the following key milestones:

1. *Speed*: 18 Gbit/s modulation in a silicon micro-ring modulator (MRM)

2. *Robustness*: 20 K temperature stability using a silicon micro-ring modulators
3. *Size*: 2.5 micron radius silicon micro ring modulator : Smallest MRM to date
4. *Scalability*: 50 Gbit/s modulation capacity using 4 WDM channels : Largest WDM modulation capacity using micro-rings
5. *Low Voltage Swing*: 150 mv swing voltage modulation in silicon micro-rings.
6. *Long Haul*: Error free transmission of 12.5 Gbit/s signal over 80 km on a standard single mode fiber.

The second part of my thesis is on slow and fast light in silicon. Using two micro-rings coupled in a coherent fashion, I have shown the following:

7. Superluminal propagation on a silicon chip using double ring cavities.
8. Designed, fabricated and tested electro-optically tunable optical delay on a silicon micro-chip, electro-optically tunable variable quality factor cavities.

The third part of my thesis explores the possibilities when MEMS and silicon photonics are put together. I have attempted two key problems :

9. Non-reciprocal devices in opto-mechanics.
10. Synchronization of frequency and phase in micromechanical devices using opto-mechanics.

BIOGRAPHICAL SKETCH

Sasikanth Manipatruni started his education in a tiny village in the coastal India. At 4, he quickly managed to disagree with his kinder garden teacher and was promoted a few classes to diffuse tensions. At 10, he went to a (co-ed) boarding school set on a beautiful hill-lock on the eastern sea board near the Bay-of-Bengal. Despite several (5 to be precise) successful and one failed attempt to run away from school, he was retained and groomed into a 'model' inmate. Then, in a purely stochastic event, which he is unable to explain to-date, he went to study at IIT Delhi. After several years of dabbling in robotics, energy systems and signal processing, trips to IUCAA, RRI, IISc and ETH, he decided to pursue his childhood dream, optics. This thesis is a result of that decision.

He was born on 1984, August 25th in the town of Vizianagaram in Andhra Pradesh. He graduated from Indian Institute of Technology (IIT), Delhi at the top of his class in Electrical Engineering in 2005. In 2004, he worked at Swiss Federal Institute of Technology (ETH-Zurich) at the Automatic Control Laboratory (IFA) developing multi-parametric optimal control algorithms. His bachelor thesis combining elements of control engineering and efficient power conversion methods was awarded the best undergraduate thesis award at IIT.

Earlier, he was a national science fellow of Indian Institute of Sciences (1999-2001) under the Kishore Vaigyanik Protsahan Yojana (KVPY). Under this program, he interned at the Inter-University Center for Astronomy and Astrophysics (IUCAA). Earlier, he studied at the Jawahar Navodaya

Vidyalaya, Vizianagaram on a beautiful campus at the foot hills of Eastern Ghats from 1994 to 1999. His working models on geo-thermal energy and solar sea water desalination have been featured twice in the Indian national science exhibitions.

He received a PhD in Electrical and Computer Engineering from Cornell in June 2010. He worked with Professor Michal Lipson at Cornell Nanophotonics Group studying silicon nanophotonics, high speed electro-optic modulation and novel phenomenon in micro-opto-mechanics. He also received a Master of Sciences from Cornell in 2009. He intends to continue exploring and enjoying optics, physics and robotics in the future.

To my Parents & Brother, who taught me how to live & dream and

To my advisor Michal & my Teachers, who taught me how to think & explore

ACKNOWLEDGMENTS

My schooling started in a tiny village in India. By fortune and the unconditional kindness of my family, friends and my advisor Prof. Michal Lipson, I could pursue my dream of studying optics. I thank you all for this journey & dedicate this dissertation to you.

I would like to thank my advisor Prof. Michal Lipson for giving me this opportunity. Michal's openness, energy and enthusiasm inspired me for the past 4 years. Michal also provided me immense freedom in research. The amount of time, effort and personal sacrifice she puts into running this group will be a model for me for years to come.

Perhaps the most important lesson I learnt from Michal is one of openness. Michal invariably remains open to every idea/bright eyed student that comes knocking on her door. I came to the US armed only with a book of problems in physics by I.E. Irodov [1], if any useful research may have happened in my PhD or will happen in the future, full credit should be given to Michal.

I would also like to thank my committee members, Prof. Alex Gaeta, Prof. Cliff Pollock for their counsel and support. Prof. Gaeta's lectures in non-linear optics happened at a critical stage of my PhD and led me to choose my research area. For that, I am very deeply thankful to Prof. Gaeta. Prof. Pollock, who was the head of the department at the time I started my PhD, created an open and welcoming department which allowed straying from my

original area of study. Prof. Pollock's lectures on teaching style and ideas on research provided a rare chance to connect personally to a teacher/scientist of his stature.

My special thanks must go to Prof. Tsuhan Chen, our director of ECE who always had a minute (at times hours) to give me advice and support me. His leadership style is truly refreshing and energizing. He and Prof. Pollock have created and sustained a collaborative and open department.

My special thanks also go to, Dr. Ian A. Young at Intel Component Research (CR), Dr. Ashok Krishna Moorthy at Sun Microsystems, for dedicating several hours of their valuable time in advising me. My special thanks to Scott Macfarlane (CCTEC), Sanjana Rao and Pradeep Machineni (Indian School of Business) with whom I had the opportunity to write and win business plans for Asia-Moot Corp, World Moot Corp, Eureka and Bangkok business challenges. I also thank Prof. Jacob Khurgin (JHU), Prof. DAB Miller (Stanford), Prof. John Bowers (UCSB), Prof. Keren Bergman (Columbia), Dr. Milos Popovic (Colorodo), Dr. Miriam Reshotko (Intel CR), Dr. Bruce Block (Intel CR), Dr. Kannan Raj (Sun Microsystems), Dr. Mehdi Asghari (Kotura), Dr. Paul Morton (Morton Photonics), Prof. Krishna Thyagarajan (IIT-D), Prof. Ajoy Ghatak (IIT-D), Prof. Saikat Ghosh (IISc), Prof. Geddam Vijay Prakash (IIT-D), Prof. Bhuvaneswari (IIT-D), Prof. Bhim Singh (IIT-D), Prof. Ehsan Afhsari (Cornell), Prof. Edwin Kan (Cornell), Prof. David Erickson (MAE) & Prof. Amit Lal (Cornell) for their feedback.

Professors Sunil Bhave, Farhan Rana, Sandeep Tiwari have always been an email/phone call away whenever I need help and advice. Prof. Rana remains my single most influential teacher in optics with his deeply thought out classes, problem sets. His patient advice on the last buses of route 93 filled me with awe and inspiration. Prof. Sandeep Tiwari was my philosophical sounding board through the past 4 years. His keen analysis and views informed me. Prof. Jose Renau (UCal Santacruz) provided the thermal imaging of AMD microprocessors for chapter on temperature insensitive modulators.

I would like to thank our group members for their support, comments and discussions. I believe some of the names from this list; will continue to be heard in optics for many years to come : Dr. Carl Poitras, Dr. Bradley Schmidt, Prof. Carlos Angulo Barrios, Prof. Qianfan Xu, Prof. Stefan Preble, Dr. Po Dong, Dr. Jacob Robinson, Dr. Long Chen, Dr. Alexander Gondarenko, Dr. Danilo Spadoti, Dr. Bernardo Kyotoku, Dr. Jaime Cardenas, Dr. Gustavo Wiederhecker, Prof. Amy Turner-Foster & Prof. Mark Foster, Dr. Mohammad Soltani, Dr. Michael Menard, Kyle Preston, Arthur Nitkowski, Jacob Levy, Nicolás Sherwood Droz, Hugo Lira, Debo Olaosebikan, Lian-Wee Luo, Lucas Gabrielli, Biswajeet Guha, Taige Hou and Mian Zhang. Carl and Brad's support and guidance early in my PhD have been of immense influence. My thanks also go to Ms. Lynn Martin, Ms. Cheryl Francis, Ms. Dorothy, Mr. Scott Coldren & Mr. Robert Roy.

I would also like to acknowledge the wonderful collaborations with Apsel group (wide temperature modulator work), Gaeta group (quantum optics),

Bergman group (Columbia, long haul silicon photonics) and Erickson group (micro-fluidics). I would especially like to thank Jacob and Gustavo for the collaborations in opto-mechanics; Carl, Kyle, Long, Hugo, Qianfan and Po for the collaborations on optical switching, poly-modulators, interconnect. Long really aced the fab and made the last batch of modulators for WDM and ultra small cavities. The work in long distance transmission with modulators was done in collaboration with Alexander 'Sasha' Biberman and Noam Ophir.

My next set of thanks goes to my closest friends: Suresh '*chal-saale*' Sridaran, Vivek 'Boa !' Venkataraman, Rajendran 'Carl-Max' Narayan and Kasturi 'Puma' Saha. Suresh, Vivek and Kasturi came from IIT Delhi, my alma mater. I can't imagine how the past 4 years would have been without them. Kasturi & Suresh extended warmth and support though my stay in Ithaca. I would also like to thank Faisal Ahmad, Jahan Dawlaty, Paul 'un-PC' George, Rajeev 'BSE' Dokania, Xiao 'PLL' Wang, Stueti 'BITS' Gupta, Sriram 'best Graphene' Sivaraman, Sudeep Mandal, Amit Singhai, Vennela Rao Thummula, with whom I had the most wonderful conversations. Faisal and I share a common world view which goes beyond academics. A *significant* list of *others* who kept things fun & interesting exists but should be reserved for a more informal account.

My most personal thanks go to, my first gurus: my mother *'baasu'* Krishnaveni, Father Ramakrishna Rao and my first friend, my brother *'banthi'* Srikanth and his wonderful family (Sailaja and Yamini). Yamini reminds me every day of the joy of innocence.

Finally, I am thankful to Minnaert [2], I.E. Irodov [1] and Feynman [3] who in no small measure have made me fall in love with optics with their irreverent style, joy of exploration. I wish I will one day see the world with their eyes.

1. I.E Irodov, Problems in General Physics. Mir Publishers 1981

2. M. Minnaert, Light and Color in the Outdoors (Springer-Verlag, New York, 1993).

3. Feynman R P. "Surely you're joking, Mr. Feynman!" Adventures of a curious character. New York: Norton, 1985

TABLE OF CONTENTS

LIST OF FIGURES

LIST OF TABLES

Chapter 1

Introduction:

SCALING SILICON NANOPHOTONIC INTERCONNECTS

Abstract: In this chapter, I briefly review the motivation for optical interconnects and the need for nanophotonic solutions to interconnect problems. I will then introduce and discuss figures of merit for nanophotonic interconnects.

Based on system level arguments, I will present 4 desirable features for silicon photonic interconnect devices: size (compactness), high speed, and multi-wavelength, *bit-lessness* as pre-requisites for silicon photonic chip/chip, inter-chip interconnects. We will also discuss the requirements in electrical energy, optical insertion losses, scalability, robustness and CMOS integration. In chapters 2 to 6, I will explore these ideas.

I will also present the motivation for exploring non-traditional interconnect devices for meeting secondary targets for optical integration such as giant tunability, interconnect latency, optical isolation and clock synchronization. In chapters 7 to 10, I will explore these ideas, namely: Optical delay & pulse advancing, optical diodes and Optical synchronization.

1.1 Introduction: The growing need for novel nanophotonic interconnects

Increasing bandwidth needs of microprocessors, datacom servers and bandwidth intensive applications [1-3] such as medical imaging [4, 5] & cloud computing [6] have created an immediate need for new interconnect solutions. Interconnects used in microprocessors [7], data centers [8, 9] and optical networks [10] are reaching a point where new technologies are essential to sustain this growth. Hence, it is of great interest to pursue novel methods for manipulating light to enable the next generation of connected world.

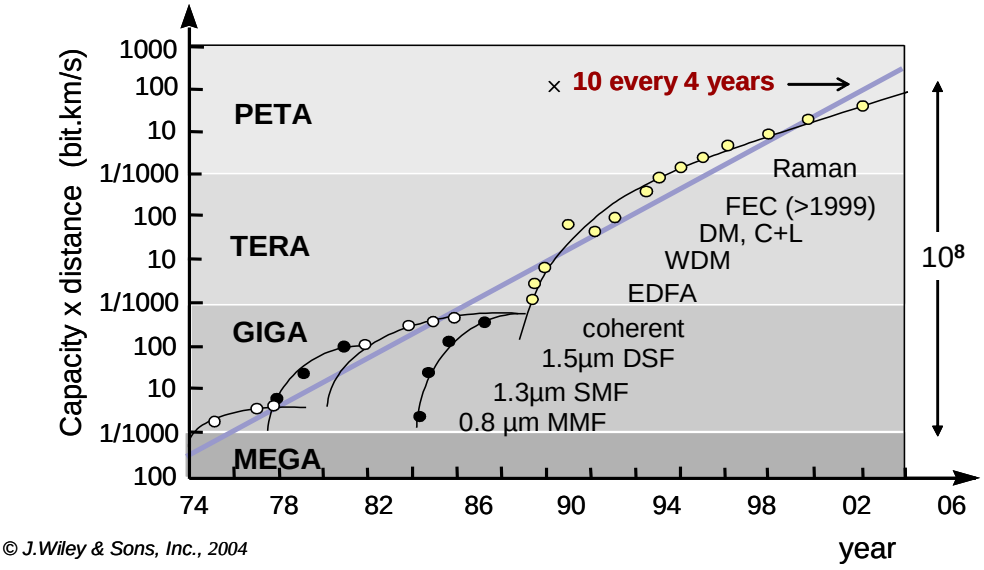

Figure 1.1 : Interconnect growth in telecom: Growth of Bandwidth Capacity

Multiple indicators across telecom, datacom and chip scale computing indicate a need for new optical technologies that are energy efficient, compact and compatible with existing technology infrastructure. In figure 1, I show the growth of bandwidth X distance capacity of internet over the past 3 decades. We can quickly identify a growth of 10X for every 4 to 5

years over the past 30 years roughly following an empirical trend given by $CxD = 5.178X2^{Y/1.053} Pb - km/s$ where Y is years since 2000 [3].

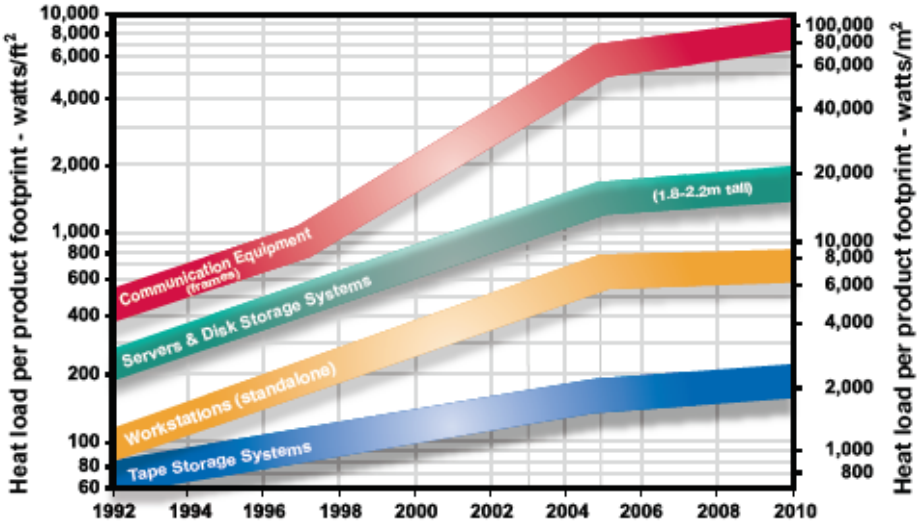

Figure 1.2: Datacom: Growth of Energy Density of a Datacom server farm

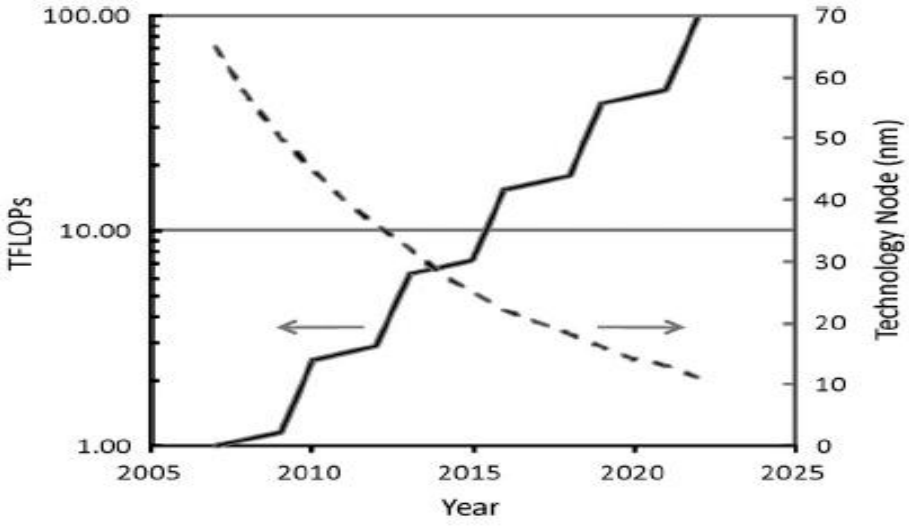

Figure 1.3: Microprocessor Bandwidth needs assuming 1 Byte/FLOP I/O

In figure 1.2, I show the heat density of existing datacom servers. In 2010, the heat density of datacom servers is expected to reach 100 kW/m^2

producing large stress on the HVAC requirements of data-servers. A third, indicator is shown in figure 3, where I show the number of floating point operations in a microprocessor as projected by ITRS [1]. Following the well-known Amdahl's balanced system law [11, 12], for an I/O bandwidth of 1 byte/FLOP, we arrive at a total interconnect bandwidth approaching a peta-bit/s. It is now well established that novel optical technologies can play a significant role in achieving these milestones [13-19].

1.2 Figures of merit for future nanophotonic interconnects and interconnect components

I will first establish figures-of merit for optical interconnects & interconnect components from the point of view of electronic-photonic integration [14].

a. Interconnect Density (β): Interconnect density is the bandwidth (B in bits/s) of an interconnect normalized for the width of the interconnect. The interconnect density on a microprocessor scales as the wire pitch of interconnects scale as per ITRS requirements. The limit of interconnect density for electrical interconnects due to signaling limits [20] is given by:

$$B_{electrical} < B_0 \left(\frac{\sqrt{A}}{L} \right)^2 \quad (1)$$

Which gives an electrical bandwidth density of,

$$\beta_{electrical} < B_0 \frac{h}{L^2} \quad (2)$$

Where $B_{electrical}$ is the electrical data bandwidth that can be transmitted through a metal interconnect of cross section A over a length L; B_0 is 10^{16}

bits/s resistive-capacitive lines on chip, 10^{17} to 10^{18} bits/s for off-chip equalized lines.; h is the height of the metal layer forming the interconnect. Typical ITRS projections for electrical interconnect density are in the order of 10-20 Gbit/s. μm.

The fundamental limit to optical interconnect density is greatly enhanced by the large central carrier frequency and the ability to multiplex large number of wavelengths allowing as high as 20 Tb/s on a single fiber [21, 22]. On a silicon nanophotonic waveguide, the bandwidth limit can be written as :

$$\beta_{Waveguide} = C_0 \frac{1}{nw} \tag{3}$$

Where C_o is a constant determined by the non-linear effects, waveguide dispersion and two photon absorption due to presence of large optical powers [23]; w=λ/15~ 103 nm is space rate of decay of the evanescent field of the waveguide [24] and n is the arbitrary factor chosen such that e^{-n} gives the factor by which the evanescent field decays. The typical pitch for placing two silicon nanophotonic waveguides can be estimated as 15λ/15 ~ 1550 nm. Novel CAD methods to separate the waveguides can reduce the effective pitch. Note that unlike electrical case, the bandwidth density is not a strong function of the length of propagation. L, the distance over which the transmission takes place only enters the analysis as a secondary effect over several meters of propagation even in presence of strong waveguide dispersion [25, 26]. The ability to send up to 1 Tb/s on a silicon waveguide have been tested experimentally [23], indicating bandwidth density limits of the waveguides exceeding 10^{18} bits/μm.s.

b. Single Wavelength Channel Bandwidth (f): Single channel bandwidth is decided by the operation speed of the receiver and transmitter at the end points of the interconnect. The limits to the optical device speed are given by the speed of modulators and detectors :

For free carrier dispersion modulators:

$$f_{optical} < \frac{1}{\tau_{\min}} = \frac{v_{sat}}{nw} \tag{4}$$

For kerr and pockel effect modulators:

$$f_{optical} < \frac{1}{\tau_{Kerr}} \tag{5}$$

For photoelectric effect detectors:

$$f_{optical} < \min(\frac{1}{\tau_{RC}}, \frac{v_{sat}}{nw}) = \min(\frac{1}{R_{inTIA} C_{inTIA}}, \frac{v_{sat}}{nw}) \tag{6}$$

Where vsat is the saturation velocity of carriers in the electro-optic material (set by the optical phonon dispersion curves), typical values of 107 cm/s. w=λ/15~ 103 nm is space rate of decay of the evanescent field of the waveguide [24] and n is the arbitrary factor chosen such that e-n gives the factor by which the evanescent field decays. The typical clearance for placing thin film planar doped regions next to silicon nanophotonic waveguides can be estimated at 3λ/15 ~ 310 nm. However, both modulators and detectors will be essentially limited by the speed of the driving electronics, set by the level of drive current and Ion per unit micron of the technology node being considered. Note that single channel speeds for electrical devices can be obtained by the limits given in previous section:

$$f_{electrical} = B_0 \left(\frac{\sqrt{A}}{L} \right)^2 \tag{7}$$

Or for a certain ITRS node, assuming that the propagation delay is the gate delay (1F04+ distributed wire delay 0.4RwCw) the interconnect bandwidth is given by

$$f_{electrical} = \frac{1}{3F04 + 1.2R_{wire}C_{wire}} \cdot \frac{AreaWidth}{wirepitch} \quad (8)$$

c. Interconnect Energy (Electrical + Optical) (E per bit):

Interconnect energy per bit for electrical interconnects is decided by the requirement to charge and discharge an electrical wire with specified capacitance and resistance (equivalent energy loss depending on the exact implementation for RLC or Non-linear transmission lines). The switching energy per bit for electrical interconnect is given by

$$E_{ElectricalSw} > CLV_r^2 \quad (9)$$

Where C is the capacitance of the section of line per unit length of the wire; L is the length of the interconnect for unrepeated lines and a constant L_{repeat} for repeated lines. V_r is the signaling voltage swing. Typical values for C are 200 aF/μm. The best case values for the optical interconnects show a strong dependence on the modal volume of the optical components and the operating voltages for the driver and receiver electronics.

The minimum bound for an optical interconnect's electrical energy per bit can be written as:

$$E_{total} = E_{source,Detect} + E_{EO} \quad (10)$$

Where E_{source} is the energy spent in the optical source signal generation; E_{EO-OE} is the energy spent in electro-optic and optoelectronic conversions. E_{source} can be written in terms of drive laser parameters and insertion losses as

$$E_{source,Detect} > \frac{\hbar\omega}{\eta_L \eta_D \kappa \alpha_m} . \frac{V_r C_d}{e} . e^{-L/l} \qquad (11)$$

Where Esource is the per bit optical energy for the light source, Cd is the capacitance of the detector, Vr is the minimum voltage to which the detector capacitance is to be charged, ηL , ηD are the quantum efficiencies of the laser and detector normalized to the maximum values, $\varkappa$ is the laser to waveguide coupling efficiency, α is the modulator insertion loss, l is the decay parameter or the waveguides. For an idealized detector capacitance of 10 fF and optimum conditions this indicates an optical energy of 8.3 fJ/bit. Note that waveguide losses, modulator insertion losses, input laser inefficiencies can quickly add up to as much as 100 fJ/bit of source laser power at nominal operation conditions (90 % coupling efficiency, 3 dB insertion loss, 0.5 W/A laser efficiency, 80 % detector responsitivity, 90 % modulator transmission).

The minimum electro-optic conversion energy per bit is given by

$$E_{EO} > \frac{V_m \Theta \Delta T}{\left(\frac{dn}{d\rho}\right)\left(\frac{dT}{dn}\right)} \qquad (12)$$

Where EEO is the electro-optic conversion energy per bit, assuming Vm modulator drive energy, Θ electro-optic modal volume, ΔT is the optical transmission change, dT/dn is the spectral sensitivity of the optical device, $dn/d\rho$ is the effective free carrier dispersion of the electro-optic device. Per

bit energies approaching 10 fJ/bit in depletion based, ultra low modal volume modulators can be expected in the near future.

Hence, the minimum bound to total interconnect energy with the tuning energy can be now obtained. In the presence of tuning power to compensate for device fabrication errors and thermal instabilities,

$$E_{total} > \frac{\hbar\omega}{\eta_L \eta_D \kappa \alpha_m} . \frac{V_r C_d}{e} . e^{-L/l} + \frac{V_m \Theta \Delta T}{\left(\frac{dn}{d\rho}\right)\left(\frac{dT}{dn}\right)} + \frac{1}{B} P_{tune} \quad (13)$$

Following the earlier arguments, this gives a minimum bound of interconnect energies at ~ 100 fJ/bit with state-of-the-art devices, including the tuning power for an optically optimized system operating at low voltages, small capacitances, ultra low modal volumes. We note that 50 fJ/bit energy is spent only in tuning the device on resonance, hence low modal volume, thermally robust devices or ultra efficient tuning mechanisms can play a critical role in reducing the interconnect energy. In order to scale the energy to sub 10 fJ/bit, new and break through devices need to be pursued while scaling the bit rate to reduce the contribution of the tuning power.

d. Areal Bandwidth Density (*D in bits/μm²*) :

The large mismatch between the optical component sizes (set by wavelength of operation and refractive indices) requires us to introduce a new figure of merit called the area bandwidth density. The area taken by the wires

themselves is separately accounted in the figure of merit, interconnect bandwidth density. The role of area bandwidth density is to quantify the footprint taken by optical components to provide a certain bandwidth density.

The modal volume of modulators as well as detectors enhanced by resonance effects are ultimately limited by diffraction limits, a notable exception being dielectric discontinuity enabled cavities [26].

$$D \equiv \frac{f}{Area}, \quad f_{optical} < \frac{1}{\tau_{\min}} = \frac{v_{sat}}{nw}, \tag{14}$$

$$D < \frac{B}{k\left(\frac{\lambda}{2N}\right)^2} \tag{15}$$

$$D_{optical} < \frac{v_{sat}}{nk\left(\frac{\lambda}{2N}\right)^3} \tag{16}$$

n is the arbitrary factor chosen such that e-n gives the factor by which the evanescentfield decays, N is the index refractive index of the guiding medium. k is an arbitrary factor more than 1. The density will have to be adjusted to allow for the driver and receiver circuits.

The bandwidth density for electrical interconnect will be dominated by the repeater electronic area given by,

$$A_{repeater} = 3K_{opt}h_{opt}L_n^2 \tag{17}$$

Where K_{opt} is the optimum number of repeaters with a value typically between 30-50 [27], h_{opt} is the optimum receiver size with a value typically between 25-50 for sub 1 micron width wires. Hence,

$$D_{electrical} = \frac{f_{electrical}}{3K_{opt}h_{opt}L_n^2} \quad (18)$$

$$D_{electrical} = \frac{1}{3K_{opt}h_{opt}L_n^2}\frac{1}{3F04+1.2R_{wire}C_{wire}}.\frac{AreaWidth}{wirepitch} \quad (19)$$

For a 2 Gbit/s link, with K_{opt}, H_{opt} =50 and a technology node of 22 nm, this implies a bandwidth density of 500 Tbit/s.mm^2.

Table 1.1 : Figures of merit for nanophotonic interconnects

Figure of Merit	Electrical	Optical
Interconnect Density (β)	$\beta_{electrical} = B_0\frac{h}{L^2}$	$\beta_{Waveguide} < C_0\frac{1}{nw}$
Single Wavelength Channel Bandwidth (f)	$f_{electrical} = \frac{1}{3F04+1.2R_{wire}C_{wire}}.\frac{W}{t}$	$f_{optical} < \min(\frac{1}{\tau_{RC}}, \frac{v_{sat}}{nw})$
Interconnect Energy (E)	$E_{ElectricalSw} > CLV_r^2$	$E_{total} > \frac{\hbar\omega}{\eta_L\eta_D\kappa\alpha_m}.\frac{V_rC_d}{e}.e^{-L/l} + \frac{V_m\Theta\Delta T}{\left(\frac{dn}{d\rho}\right)\left(\frac{dT}{dn}\right)} + \frac{1}{B}P_{tune}$
Areal Bandwidth Density	$D_{electrical} = \frac{f_{electrical}}{3K_{opt}h_{opt}L_n^2}$	$D_{optical} < \frac{v_{sat}}{nk\left(\frac{\lambda}{2N}\right)^3}$

System level requirements for nanophotonic interconnect:

Hitless Operation and Inter-channel Interference: Hitless operation is an essential condition for co-operation of a multi wavelength optical network

on chip. By ensuring that the modulators, switches, filters and other photonic components are spectrally specific we can avoid signal degradation due to operation of components at nearby wavelengths. Novel spectral design of optical components is essential for avoiding cross talk between optical wavelengths in a potential WDM system.

a. CMOS Compatibility: The requirement of a light isolating oxide layer of 3 micron thickness imposes a strong limitation on the CMOS compatibility of optical components in silicon. Electronic oxide layer thicknesses are lower than 100 nm for allowing large thermal conductivity. It is therefore essential to come up with new techniques to allow for optical integration.

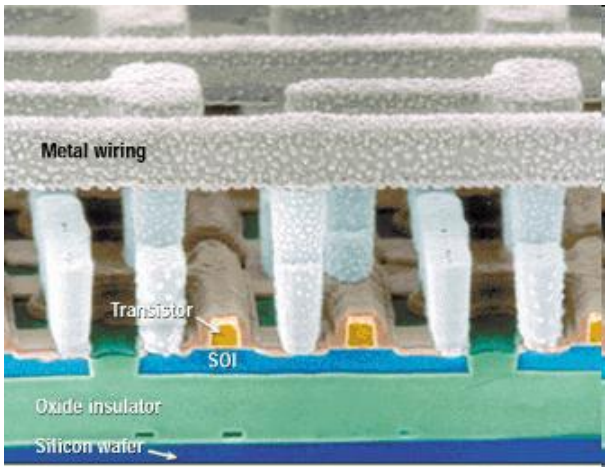

Figure 1.4: Cross section of an SOI electronic chip; oxide thickness and thermal budgets can impose strict design restictions for optics.

Two possible methods have been actively pursued a)Substrate removal b) 3D integration using deposited polysilicon/SiN materials. I will outline the 3D integration technique using deposited materials briefly in the next section.

b. CMOS Electrical Compatibility (Low Current, Low Voltage): To allow for the CMOS length scaling, the peak high speed voltages available on chip have been scaling down rapidly. The present generation CMOS already uses sub 1V voltage swing for CMOS logic and the voltage is expected to scale to 600 mV in the future. Hence, it is important to pursue new methods for low voltage switching.

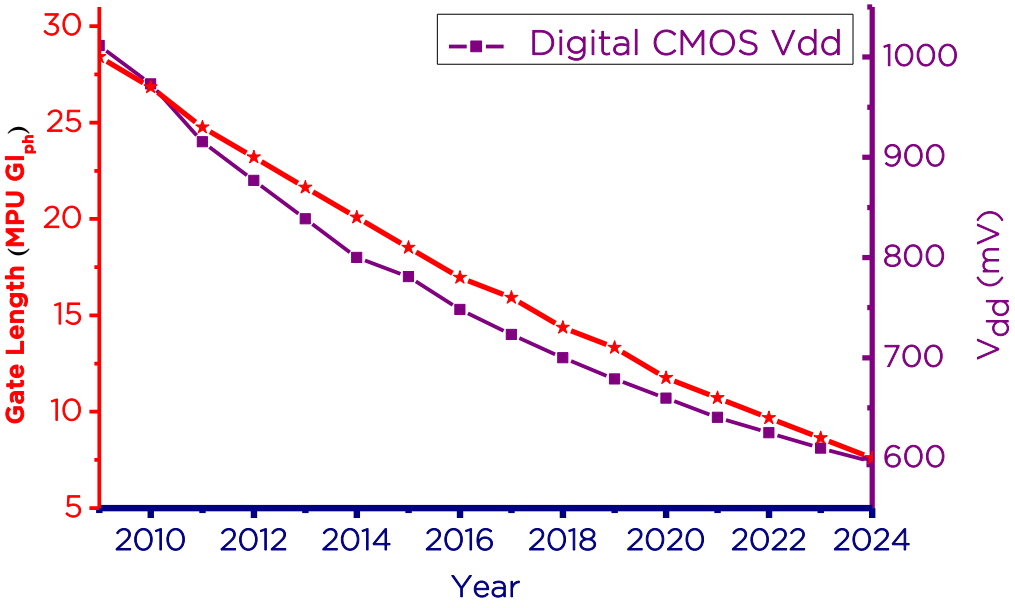

Figure 1.5: Voltage and technology node scaling in CMOS [1]

c. Scalability: The proposed interconnect scheme should allow a simple, low complexity, low operational overhead multiplexing scheme. As I will demonstrate later, a multiplexing scheme is essential for optics to compete with electronic interconnects due stringent requirements of bandwidth density per unit pitch length.

d. Temperature Robustness: The proposed modulator should be robust to variations in temperature for operating computational environments. 1) Run-time operating temperature shift of 20 K 2) Quiescent temperature shifts of >60 K.

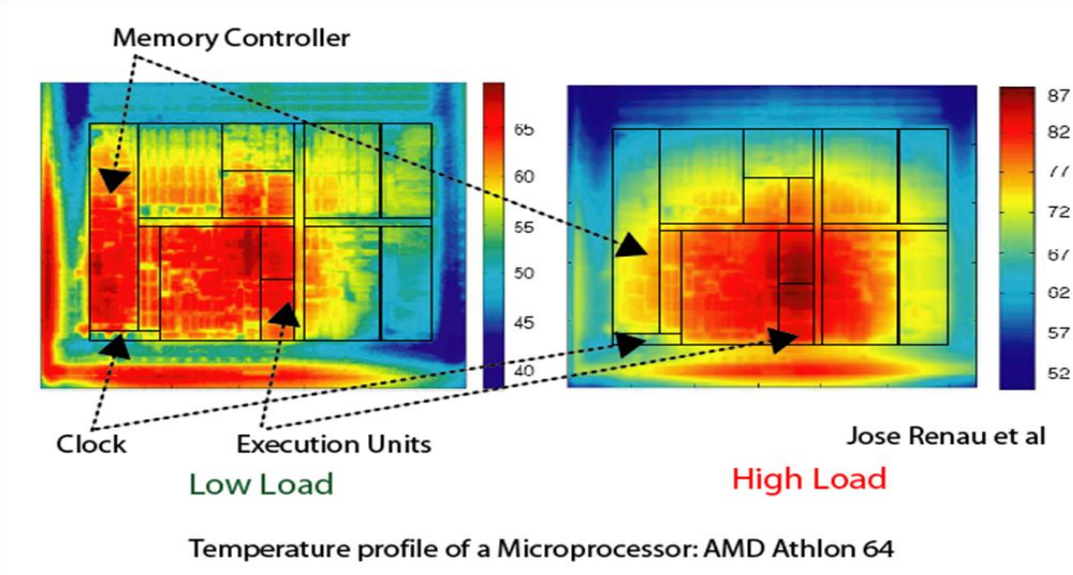

Figure 1.6: Spatial Temperation Variation on a CMOS Microprocessor [28] [Courtesy: Prof. Jose Renau, UC Santa Cruz]

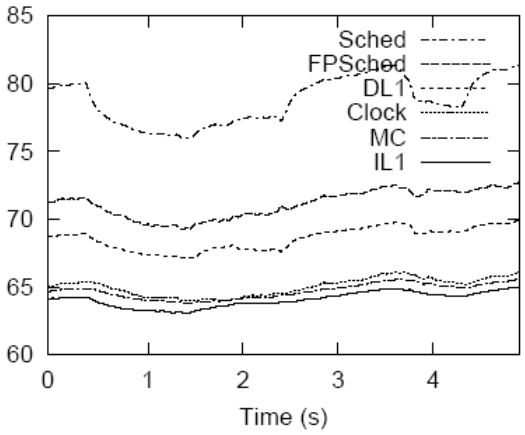

Figure 1.7: Temporal Temperation Variation on a CMOS Microprocessor [28] [Courtesy: Prof. Jose Renau, UC Santa Cruz]

It may be possible to tradeoff modal volume with temperature stability. However, the energy/bit constraints will limit the on-chip devices to small

modal volumes. Hence, viable low power tuning mechanisms need to be pursued to reduce the tuning power spent per bit.

1.3. Compact, Multi-wavelength, High speed, CMOS Silicon Photonic Interconnect Components

Based on the figures of merit proposed earlier, I will present a minimal set of optical components that can enable a scalable architecture. Four rules for optical components on chip can be realised from the presented figures of merit.

Table 1.2: Minimal Features of nanophotonic interconnects

Property	Description	FOM Target
Compact	Size of modulators, detectors, switches	A > 100 Tbps/mm^2 Modal Volume ~ 1 μm^3 Detector C_d< 10 fF
High Speed	Data Rate per channel	f~ 10-40 Gbps*
Multi-wavelength	Multiple Wavelength networks	Interconnect Density (B) > 50 Gbps/ μm
CMOS compatible	Low voltage, low current	V_{dd} < 600 mV

We identify 4 essential features of silicon photonic interconnect components. These are compactness, broadband operation (High speed), Multiple-wavelength compatibility, CMOS electronic compatibility. CMOS compatibility in drive currents and voltages must be ensure so that future technology nodes may allow for direct logic drive operation of the interconnect components.

a. Compact: The dimensions of modulator, detector, switches and delays directly contribute to the areal density of interconnects. Small devices also enable lower modal volumes, capacitances and reduce the energy per bit for modulation and detection. The target sizes of the modulators and detectors are less than 1 μm^3.

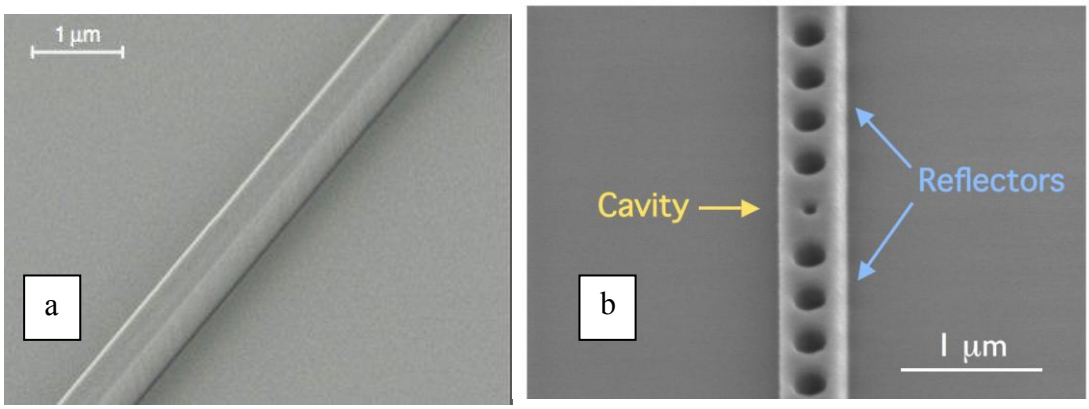

Figure 1.8 a) Silicon Nanophotonic waveguide b) An Ultra small modal volume optical cavity [29]

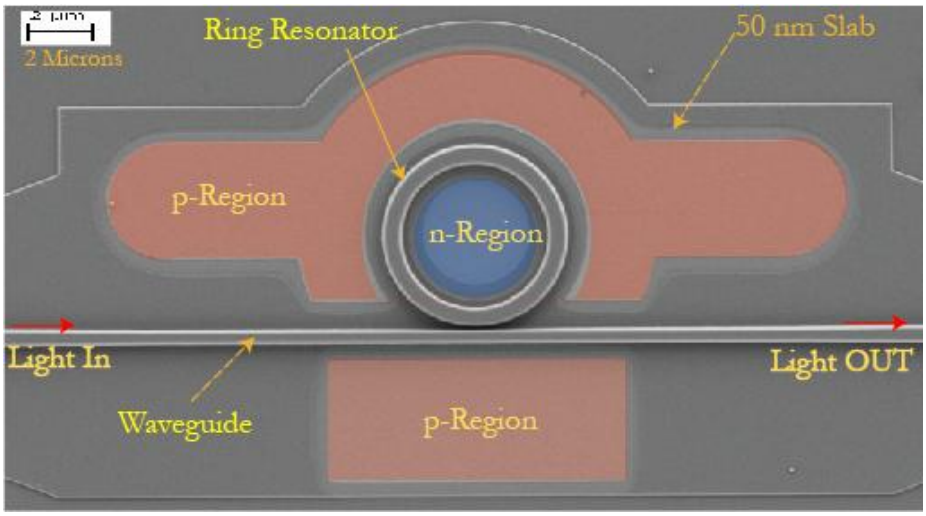

Figure 1.9 A silicon microring of radius 2.5 microns and modal volume 1 μm^3 embedded in a PIN electrical structure [30]

b. High speed, Broadband Devices: Higher speed of operation will allow large interconnect densities and off set the tuning power to reduce the energy/bit. Target speeds are in 10 to 40 Gbps for modulators with switch bandwidths to allow switching of 40 Gbit/s signals.

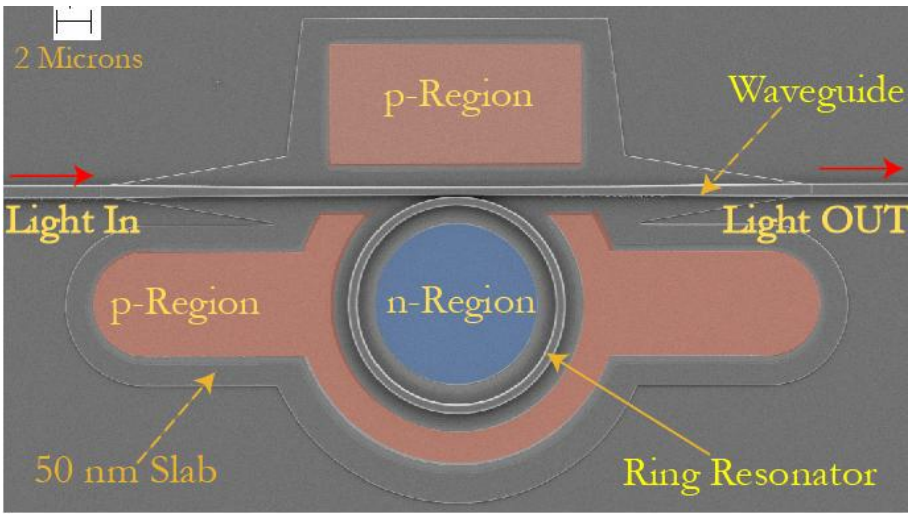

Figure 1.10 An 18 Gbit/s single channel modulator in silicon [31]

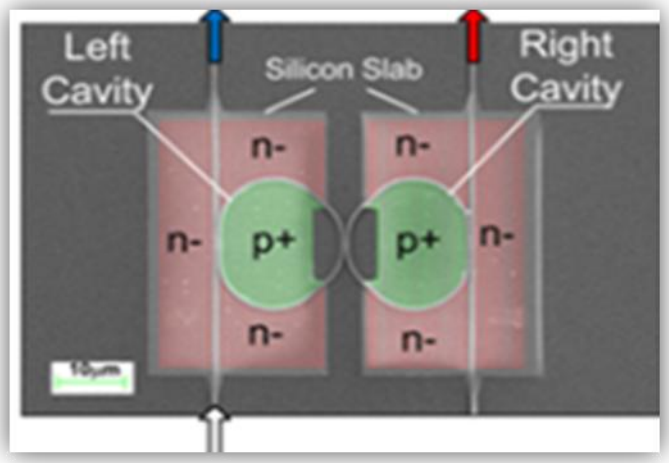

Figure 1.11 A 40GHz broad band hitless electro-optic switch [32]

c. Multi-wavelength: Multiple wavelength operation is essential for the interconnect density scaling since the pitch for the optical waveguides is on

the scale of the optical Wavelength Divison Multiplexing (WDM) is ideally suited for an on-chip optical interconnect due to complexity, foot print and optical insertion loss considerations. This can be arrived at, as follows: in general, three basic multiplexing schemes can be conceptualized for an on-chip optical interconnect

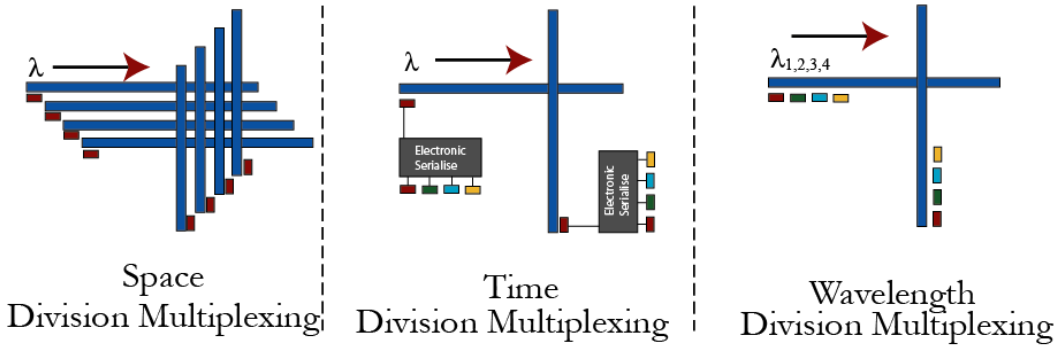

Figure 1.12: Methods for scaling optical interconnect modulation bandwidths. Three basic methods a) space division multiplexing (SDM) b) Time divison multiplexing (TDM) c) Wavelength division multiplexing (WDM). Footprint and waveguide crossings prohibit an aggressive SDM. Serialise and deserialise operations limit TDM.

a) Space Divison Multiplexing (SDM) b) Time Divison Multiplexing (TDM) c) Wavelength Divison Multiplexing (WDM). The scalability of SDM and TDM are severely limited on an on chip planar integrated circuit. SDM scalability is limited by the problem of efficiently crossing multiple waveguides, multiple times with low cross talk and insertion losses [34, 35]. TDM based systems (relying on free carrier dispersion) are limited fundamentally by the speed of carrier response in the semiconductors and the foot print and power requirements of serialize and de-serialize circuits. A second, critical functionality of WDM can be in routing the signals spatially based on the wavelength thus avoiding complex network routing algorithms.

Figure 1.13: 50 Gbit/s WDM modulator band formed by 4 , 12.5 Gbit/s modulators [33]

d. CMOS Compatibility: The modulators, detectors, switches must operate with available voltage and current requirements of digital CMOS to enable direct low complexity driving circuits. Sub 1V modulation with current drive requirements with in the digital logic current drives can enable easy CMOS integration.

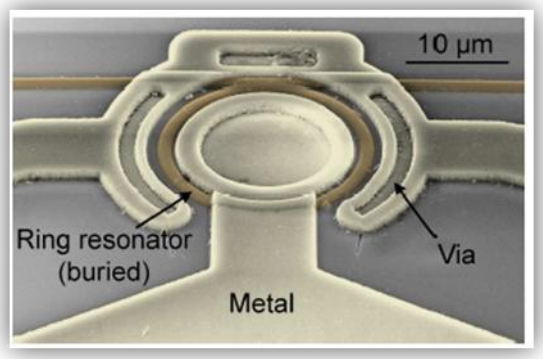

Figure 1.14: 3D integrated polysilicon electro-optic modualtor at 1 Gbit/s [36]

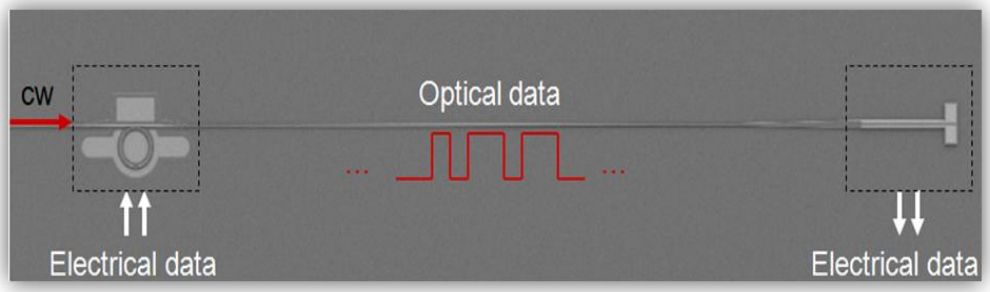

Figure 1.15: A 4 Gbit/s short range optical interconnect with integrated detectors [37]

e. Spatially and Spectrally Hitless Devices:

In order to scale the total bandwidth on chip, it is essential to avoid any interference between the optical wavelength channels and signals passing in different directions (North, East, South, and West). This has to be achieved both spatially to allow for spatial scaling of the interconnect as well as spectrally to achieve non-interfering filters.

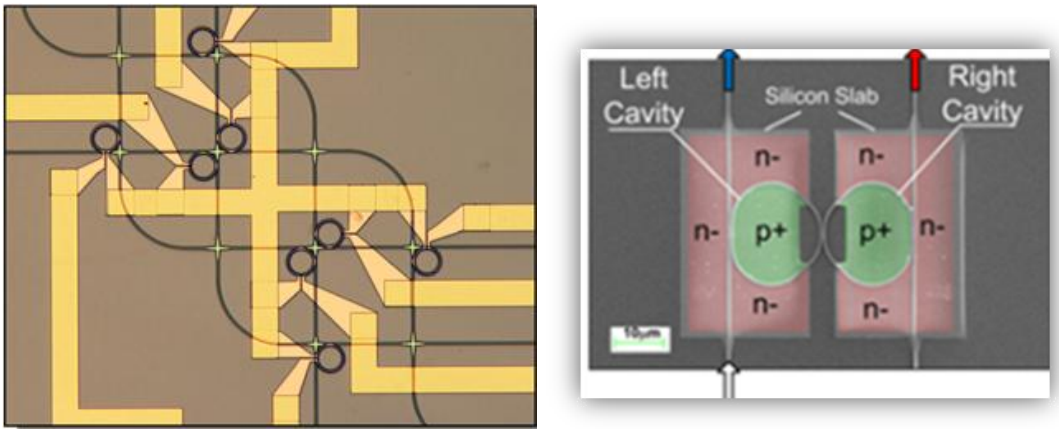

Figure 1.16: a) A spatially hit-less router (Image Courtesy: Nicolas Sherwood), allowing an 4 directional switch [38] b) a spectrally hitless broadband switch [32]

Table 1.3: System Level Features of nanophotonic interconnects

Property	Description	Target
Hit-less	Multiple Wavelength networks	Allow more than 100 Channels
Temperature Robustness	Large temperature robustness	T Є (0, 100) °C ΔT>20 K
Scalability	CAD compatible, Design Libraries	CAD tools & Device Libraries
Packaging	Pin density and packaging	Large I/O Pin density, Low cost packaging

1.4 Emerging Interconnect Devices & Outstanding problems

Substantial problems in architectures remain even with the most aggressively scaled optics over the next few years [14]. These problems can be broadly classified into the following categories:

a. **Efficient Tuning of optical devices over large range:** Tuning becomes a necessity due to a) Fabrication tolerances b) Ambient temperature condition changes c) Chip operating condition changes. As we saw earlier the total per bit energy is at least :

$$E_{total} > \frac{\hbar\omega}{\eta_L \eta_D \kappa \alpha_m} . \frac{V_r C_d}{e} . e^{-L/l} + \frac{V_m \Theta \Delta T}{\left(\frac{dn}{d\rho}\right)\left(\frac{dT}{dn}\right)} + \frac{1}{B} P_{tune} \quad (20)$$

The tuning power can form a significant part of the total energy even with the most aggressively scaled devices. Hence it is essential to reduce the tuning power per nm of the optical devices.

b. **Signal Timing control, Clock distribution, Synchronisation:** Some of these problems pertain to timing control on the chip [41, 42] due problems associated with large latency. Timing problem can be closely related to generation of synchronised signals over a long range.

c. Isolators and Circulators to protect the input lasers: Isolation of the laser sources is essential for any interconnect architecture [43]. Efficient low loss isolators and surge protectors can enhance the operational time of

the optical sources, reducing the cost and increasing the mean time to failure of the microprocessor architecture.

1.4.1 Efficient Tuning of optical devices over large range:

a. Thermo-optic effect in Silicon : Silicon (like most other semiconductors) exhibits a strong positive thermo-optic effect due to the sensitivity of band gap to temperature [44], attributed to lattice dilation with temperature. The change in the band gap is translated into a change in the refractive index following the Moss law for semiconductors [45, 46].

$$\frac{\partial n}{\partial T} = -\frac{n}{4E_g}\frac{\partial E_g}{\partial T} \tag{21}$$

Using the appropriate model for band-gap dependence with temperature [46]

$$\frac{\partial n}{\partial T} = \frac{nS\langle\hbar\omega\rangle^2}{8E_g kT^2 \sinh^2\left(\langle\hbar\omega\rangle/2kT\right)} = 1.8X10^{-4}K^{-1} \tag{22}$$

Where S=1.49 is a dimensionless coupling constant related to the strength of electron-phonon interaction, and $\langle\hbar\omega\rangle$=25.5 meV is the average phonon energy, E_g=1.557 is the bandgap at 300 K, n is the refractive index at 300 K. (See appendix B, for a detailed description). This corresponds to a wavelength shift of 0.1 nm/K in silicon on insulator waveguides.

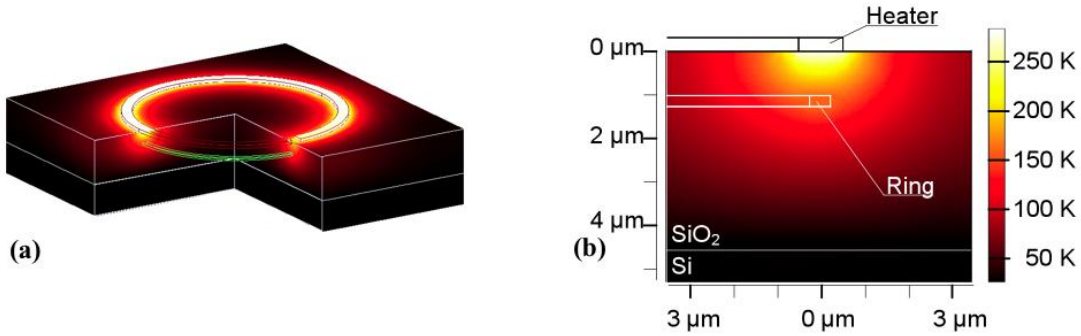

Figure 1.17: a) An integrated micro-heater b) Temperature profile of the waveguide cross section (Image Courtesy: Nicolas Sherwood)

b. Thermo-optic tuning in Silicon via micro-heaters: By efficient integration of micro-heaters it is possible to achieve sub mW/nm tuning efficiency in silicon on insulator substrates [38, 47]. It is important to achieve low power tuning to compensate for various factor since the tuning power directly adds to the bit energy. The best efficiency shown so far is 550 µW/nm [47]. However, even the best efficiencies shown so far will average a 500 fJ/bit tuning power at 10 Gbit/s for tuning range of 10 K. Hence, it is of great interest to pursue alternate tuning methods.

c. Controlled Thermo-optic tuning in Silicon via self heating effect: Another efficient method for controlling the temperature of a waveguide is by using the joule heating from the carriers across a PIN junction to control the waveguide temperature [48]. Due to the efficient overlap of the generated heat with the waveguide, this method can produce the best heating efficiency per mW spent power.

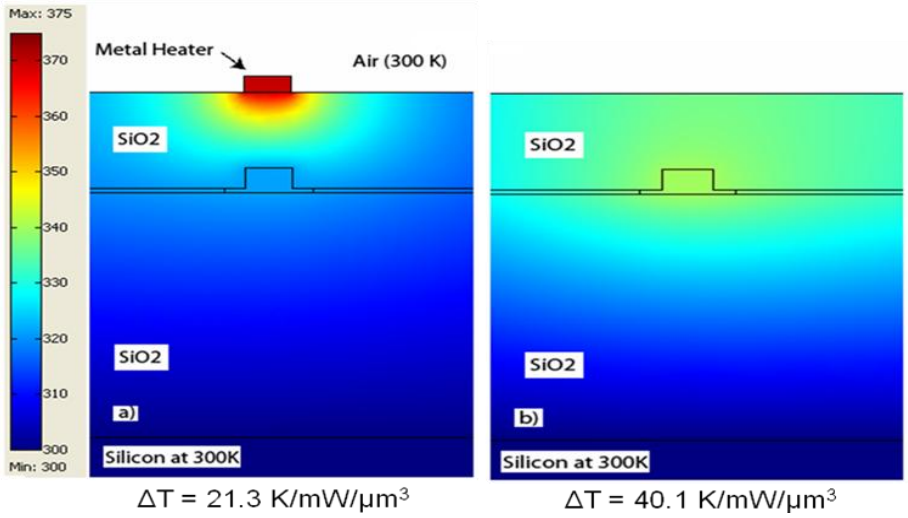

Figure 1.18: a) Temperature profile with a microheater integrated on top b) Self-heating of PIN junction device [48]

d. Direct tuning by mechanical reconfiguration in Silicon: Optical structures can exhibit large sensitivity to mechanical reconfiguration [49]. The actuation mechanisms to move the structure can be a direct mechanical actuation [49], or an electro-static mechanism [50] or using radiation forces to reconfigure the devices [51] which can be extended to large tuning ranges using very closely placed optical structures [52]

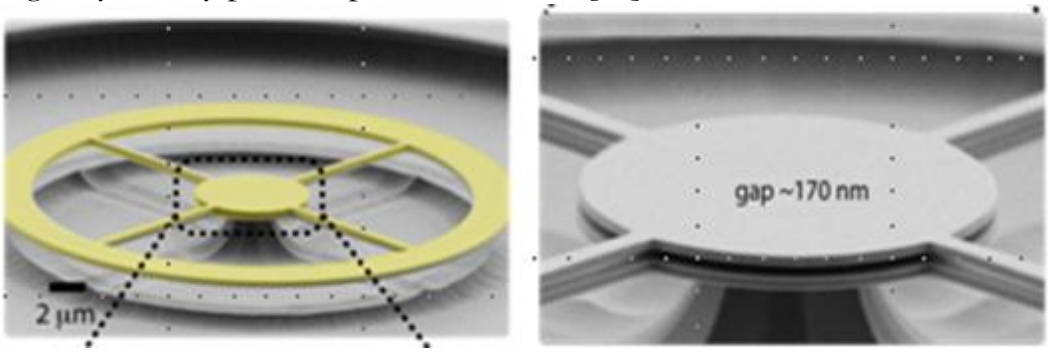

Figure 1.19: a) Optomechanical structure for large tuning range of photonic structures. The small gap allows for very strong perturbation to the optical mode creating large tuning range with mW optical powers [G.Weiderhecker, S. Manipatruni, M. Lipson CLEO'10].

Table 1.4: Wide range tuning methods in silicon photonics

Technique	Description	Tuning Hold Power
Thermal	Micro-heaters	550 μW/nm
Self Heating	Joule Heating of Active Devices	500 μW/nm
Carrier Based	Carrier Dispersion Compensation	Limited Range*
Optomechanical	Near Field Perturbation	~ 100 μW/nm
Electro-mechanical	Near Field Perturbation	Negligible
Mechanical	Near Field Perturbation	Negligible

1.4.2 Timing (Latency) Control on Chip:

Optics can play a critical role in timing and latency control on chip. The ability to control the speed of optical pulses can enable clock and data synchronisation for optical interconnects [53].

The following functionalities have been attempted for timing control using optics.

a. Deliver and retain precise timing of pulses [54]
b. Reducing interconnect latency [55]
c. Skew and jitter removal [56]
d. Reduction of number of levels in a clock distribution network [57]

a. Delays and Pulse Advances on chip using micro-cavities:

To enable high level functionalities described above, it is essential to start with a on chip microphotonic method to delay and advance optical pulses.

Coherently coupled optical cavities have been proposed and electrically integrated to generate controllable delays and pulse advances [39, 40].

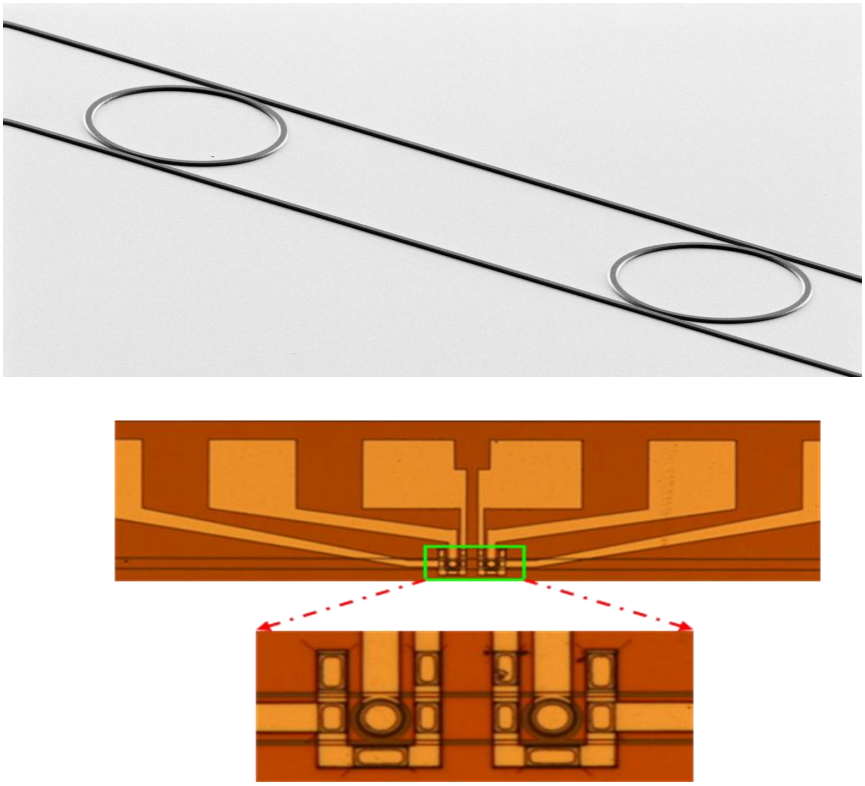

Figure 1.20: a) A coherent supermode cavity for slow light applications [39]
b) electrically integrated slow light device [40]

b. Synchronisation on Chip: Non-linear optomechanical frequency pulling for generating low noise, phase locked clock signals

Synchronisation, the phenomenon of spontaneous emergence of coherence among non-linear systems [58] can be exploited to create controlled oscillators [59]. Synchronization of on chip systems can enhance the quality of clock distribution. However, so far micro-scale mechanical coupling and synchronization between cavities has been limited due to the non-directionality of acoustic radiation, anchor topologies, substrate leakage/material phonon losses as well as restrictions of neighbourhood in

coupling. Hence, it is of great interest to purse alternate mechanisms for coupling and synchronizing distributed micro-mechanical systems.

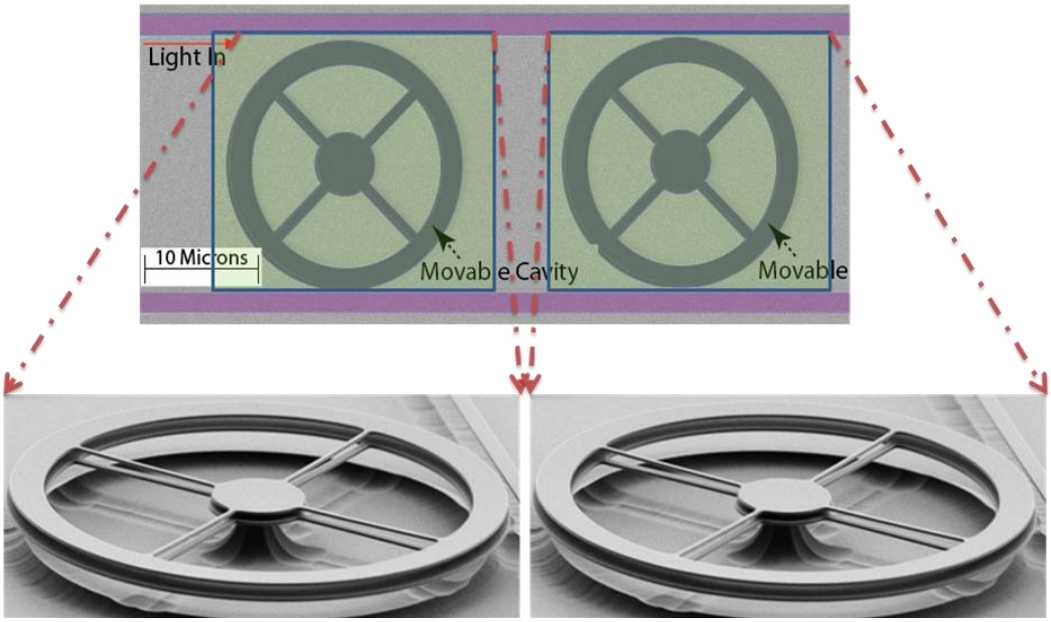

Figure 1.21: a) Mechanical coupling between micro-opto-mechanical oscillator mediated by radiation forces [61]

A method for radiation force mediated coupling and synchronisation of micro-scale mechanical resonators is shown in figure 1.21. Unlike mechanical coupling, coupling due to optical radiation forces can be achieved when the resonators are separated by a long distance. Optomechanical coupling can enable new level of control due to the ability to manipulate optical modes over a large range of time scales [60]. It is possible to show that long range coupling and synchronisation between mechanical cavities can be achieved by coupling the optomechanical devices [61].

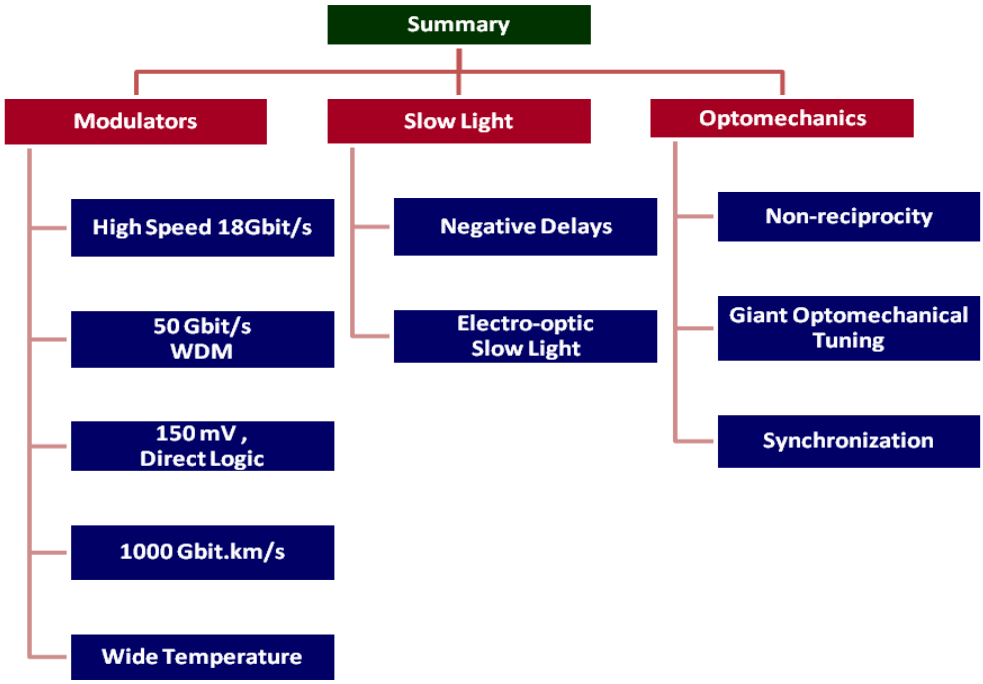

Figure 1.22: Thesis Organisation

1.4.3 Isolation and Non-reciprocity: Isolation and protection of lasers is a critical step in any optical interconnect. The cost and complexity to integrate isolators and protectors for a large number of wavelength sources for on-chip and off-chip communication can add up very quickly.

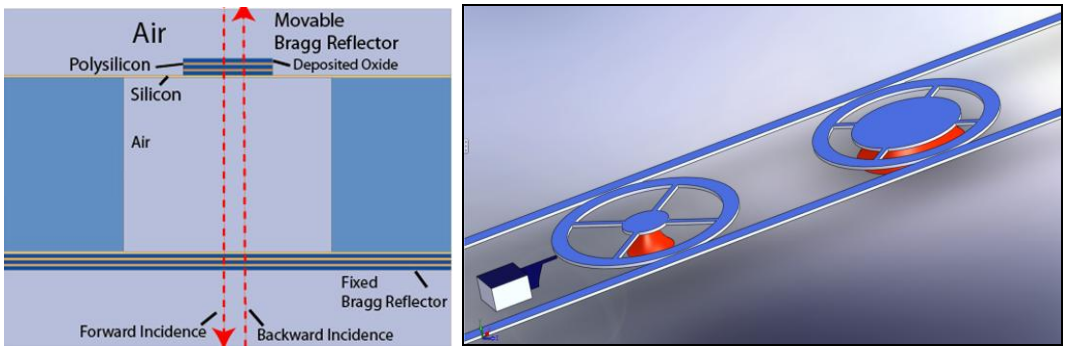

Figure 1.23: a) Theoretical proposal for breaking reciprocity on a microphotonic chip [62]

Breaking the reciprocity of light on-chip can lead to an important new class of optical devices such as isolators, which are critical for the development of photonic systems. Novel optomechanical structures have been proposed to utilise the direction dependent mechanical reconfiguration of optical structures to create non-reciprocal devices [62].

1.5. Thesis organisation

This thesis is organised into three generic sections on 1) Modulators 2) Delay Devices 3) Optomechanical Devices. Chapters 2 to 6 concentrate on various ways of scaling the modulators to meet the interconnect challenges. Chapters 7, 8 concentrate on the delay devices. Chapters 9 and 10 concentrate on alternate technologies to achieve some of the most challenging goals of micro-photonics: i.e Giant tunability, Optical isolation and optomechanical synchronisation.

REFERENCES

1. International Technology Roadmap for Semiconductors (ITRS 2009).

2. Moore, Gordon E. (1965). "Cramming more components onto integrated circuits" . Electronics Magazine. pp. 4. Retrieved 2006-11-11.

3. Emmanuel B. Desurvire, "Capacity Demand and Technology Challenges for Lightwave Systems in the Next Two Decades," J. Lightwave Technol. 24, 4697-4710 (2006)

4. P. C. Hammel, "Imaging: Nanoscale MRI", Nature , 2009, 458, 844.

5. Degen, C. L., Poggio, M., Mamin, H. J., Rettner, C. T. & Rugar, D., "Nanoscale magnetic resonance imaging", Proc. Natl Acad. Sci. USA 106, 1313–1317 (2009).

6. Michael R. Nelson, "Building an Open Cloud", (26 June 2009) Science 324 (5935), 1656. [DOI: 10.1126/science.1174225]

7. N. Magen, A. Kolodny, U. Weiser, and N. Shamir, "Interconnect-power dissipation in a microprocessor", in Proc. 2004 Int. Workshop System Level Interconnect Prediction (ACM, 2004) Session Interconnect Anal. SoCs Microprocess., pp. 7–13.

8. L. A. Barroso and U. Ho¨lzle, "The case of energy-proportional computing", IEEE Computer, vol. 40, pp. 33–37, Dec. 2007.

9. J. G. Koomey, "Estimating total power consumption by servers in the U.S. and the world. Available:
http://enterprise.amd.com/Downloads/svrpwrusecompletefinal.pdf

10. Katharine Gammon. Networking: Four ways to reinvent the internet. Nature, 463(7281):602–604, February 2010

11. Amdahl, Gene "Validity of the Single Processor Approach to Achieving Large-Scale Computing Capabilities" AFIPS Conference Proceedings (30): 483–485. (1967)

12. J. Gray and P. Shenoy, BRules of thumb in data engineering,[in Proc. Int. Conf. Data Engineering (ICDE'00), 2000.

13. Young, I.A.; Mohammed, E.; Liao, J.T.S.; Kern, A.M.; Palermo, S.; Block, B.A.; Reshotko, M.R.; Chang, P.L.D.; , "Optical I/O Technology for Tera-Scale Computing," Solid-State Circuits, IEEE Journal of , vol.45, no.1, pp.235-248, Jan. 2010

14. D. A. B. Miller, "Device Requirements for Optical Interconnects to Silicon Chips," Proc. IEEE **97**, 1166 - 1185 (2009)

15. A. V. Krishnamoorthy, et al, "The integration of silicon photonics and VLSI electronics for computing systems intra-connect", Proc. SPIE 7220, 72200V (2009).

16. C. Batten, et al, "Building Manycore Processor-to-DRAM Networks with Monolithic Silicon Photonics," High-Performance Interconnects, Symposium on, pp. 21-30, 16th IEEE Symposium on High Performance Interconnects, 2008.

17. R. Beausoleil, et al, "A Nanophotonic Interconnect for High-Performance Many-Core Computation," in Integrated Photonics and Nanophotonics Research and Applications, (Optical Society of America, 2008), paper ITuD2

18. Shacham, K. Bergman, and L. P. Carloni, "On the Design of a Photonic Network-on-Chip," in Networks-on-Chip (2007), pp. 53-64.

19. Kirman, N.; et al, "Leveraging Optical Technology in Future Bus-based Chip Multiprocessors," Microarchitecture, 2006. MICRO-39. 39th Annual IEEE/ACM International Symposium on , vol., no., pp.492-503, 9-13 Dec. 2006

20. D. A. B. Miller and H. M. Ozaktas, BLimit to the bit-rate capacity of electrical interconnects from the aspect ratio of the system architecture,[J. Parallel Distrib. Comput., vol. 41, p. 4252, 1997.

21. A. H. Gnauck, R. W. Tkach, A. R. Chraplyvy, and T. Li, "High-capacity optical transmission systems", J. Lightw. Technol., vol. 26, pp. 1032–1045, 2008.

22. A. H. Gnauck, G. Charlet, P. Tran, P. J. Winzer, C. R. Doerr, J. C. Centanni, E. C. Burrows, T. Kawanishi, T. Sakamoto, and K. Higuma, "25.6-Tb/s WDM transmission of polarization-multiplexed RZ-DQPSK signals", J. Lightw. Technol., vol. 26, pp. 79–84, 2008.

23. B. G. Lee, X. Chen, A. Biberman, X. Liu, I-W. Hsieh, C.-Y. Chou, J. I. Dadap, F. Xia, W. M. J. Green, L. Sekaric, Y. A. Vlasov, R. M. Osgood, Jr., K. Bergman, "Ultrahigh-Bandwidth Silicon Photonic Nanowire Waveguides for On-Chip Networks," IEEE Photonics Technology Letters 20 (6) 398-400 (May 15, 2008).

24. J. T. Robinson, S. F. Preble, and M. Lipson, "Imaging highly confined modes in sub-micron scale silicon waveguides using transmission-based near-field scanning optical microscopy", Opt. Express, vol. 14, 10588 (2006)

25. H. K. Tsang, C. S. Wong, T. K. Liang, I. E. Day, S. W. Roberts, A. Harpin, J. Drake, and M. Asghari, "Optical dispersion, two-photon absorption and self-phase modulation in silicon waveguides at 1.5 μm wavelength", Appl. Phys. Lett. 80, 416-418 (2002).

26. J. T. Robinson, C. Manolatou, L. Chen, and M. Lipson, "Ultrasmall mode volumes in dielectric optical microcavities," Phys. Rev. Lett., vol. 95, 143901 (2005)

27. Magdy A. El-Moursy, Eby G. Friedman, Optimum wire sizing of RLC interconnect with repeaters, Integration, the VLSI Journal, Volume 38, Issue 2, December 2004, Pages 205-225, ISSN 0167-9260, DOI: 10.1016/j.vlsi.2004.04.001.

28. Francisco-Javier Mesa-Martinez, Michael Brown, Joseph Nayfach-Battilana, Jose Renau, "Measuring Power and Temperature from Real Processors", The Next Generation Software (NGS) Workshop (NGS08) held in conjunction with IPDPS, April 2008.

29. B. Schmidt, Q. Xu, J. Shakya, S. Manipatruni, and M. Lipson, " Compact electro-optic modulator on silicon-on-insulator substrates using cavities with ultra-small modal volumes," Opt. Express 15, 3140-3148 (2007)

30. S. Manipatruni, L. Chen, K. Preston, and M. Lipson, "Ultra Low Voltage (150 mVpp) Electro-Optic Modulator on Silicon," Manuscript in preparation

31. S. Manipatruni, Q. Xu, B. Schmidt, J. Shakya, and M. Lipson, "High Speed Carrier Injection 18 Gb/s Silicon Micro-ring Electro-optic Modulator," LEOS 2007, IEEE LEOS 2007 Annu. Meeting, Paper WO2, 537-538 (2007).

32. Hugo L. R. Lira, Sasikanth Manipatruni, and Michal Lipson, "Broadband hitless silicon electro-optic switch for on-chip optical networks," Opt. Express 17, 22271-22280 (2009)

33. S. Manipatruni, L. Chen, and M. Lipson, "50 Gbit/s wavelength division multiplexing using silicon microring modulators," in Proceedings of 6th IEEE International Conference on Group IV Photonics (IEEE 2009), pp. 244–246.

34. Popovic, M.A.; Ippen, E.P.; Kartner, F.X., "Low-Loss Bloch Waves in Open Structures and Highly Compact, Efficient Si Waveguide-Crossing Arrays," Lasers and Electro-Optics Society, 2007. LEOS 2007. The 20th Annual Meeting of the IEEE , vol., no., pp.56-57, 21-25 Oct. 2007

35. S. G. Johnson, C. Manolatou, S. Fan, P. R. Villeneuve, J. D. Joannopoulos, and H. A. Haus, "Elimination of cross talk in waveguide intersections," Opt. Lett. 23, 1855-1857 (1998)

36. Kyle Preston, Sasikanth Manipatruni, Alexander Gondarenko, Carl B. Poitras, and Michal Lipson, "Deposited silicon high-speed integrated electro-optic modulator," Opt. Express 17, 5118-5124 (2009)

37. Long Chen, Kyle Preston, Sasikanth Manipatruni, and Michal Lipson, "Integrated GHz silicon photonic interconnect with micrometer-scale modulators and detectors," Opt. Express 17, 15248-15256 (2009)

38. Nicolás Sherwood-Droz, Howard Wang, Long Chen, Benjamin G. Lee, Aleksandr Biberman, Keren Bergman, and Michal Lipson, "Optical 4x4 hitless slicon router for optical networks-on-chip (NoC)," Opt. Express 16, 15915-15922 (2008)

39. Sasikanth Manipatruni, Po Dong, Qianfan Xu, and Michal Lipson, "Tunable superluminal propagation on a silicon microchip," Opt. Lett. 33, 2928-2930 (2008)

40. Sasikanth Manipatruni, Carl B. Poitras, Qianfan Xu, and Michal Lipson, "High-speed electro-optic control of the optical quality factor of a silicon microcavity," Opt. Lett. 33, 1644-1646 (2008)

41. D. Agarwal , G. A. Keeler , C. Debaes , B. E. Nelson , N. C. Helman and D. A. B. Miller "Latency reduction in optical interconnects using short optical pulses", IEEE J. Sel. Topics Quantum Electron., vol. 9, pp. 410 2003.

42. G. A. Keeler , B. E. Nelson , D. Agarwal and D. A. B. Miller "Skew and jitter removal using short optical pulses for optical interconnection", IEEE Photon. Technol. Lett., vol. 12, pp. 714 2000.

43. G. A. Keeler , B. E. Nelson , D. Agarwal and D. A. B. Miller "Skew and jitter removal using short optical pulses for optical interconnection", IEEE Photon. Technol. Lett., vol. 12, pp. 714 2000.

44. Y. P. Varshni, Temperature dependence of the energy gap in semiconductors", Physica (Amsterdam) 34, 149 (1967).

45. T. S. Moss, Optical Properties of Semiconductors. Butterworths, London, 1961.

46. D.Y. Lin, C.F. Li, Y.S. Huang, Y.C. Jong, Y.F. Chen, L.C. Chen, C.K. Chen, K.H. Chen and D.M. Bhusari, "Temperature dependence of the direct band gap of Si-containing carbon nitride crystalline films", Phys. Rev. B 56 (1997), p. 6498

47. M. R. Watts, W. A. Zortman, D. C. Trotter, G. N. Nielson, D. L. Luck, and R. W. Young, "Adiabatic Resonant Microrings (ARMs) with Directly Integrated Thermal Microphotonics," in Conference on Lasers and Electro-Optics/International Quantum Electronics Conference, OSA Technical Digest (CD) (Optical Society of America, 2009), paper CPDB10.

48. Sasikanth Manipatruni, Rajeev K. Dokania, Bradley Schmidt, Nicolás Sherwood-Droz, Carl B. Poitras, Alyssa B. Apsel, and Michal Lipson, "Wide temperature range operation of micrometer-scale silicon electro-optic modulators," Opt. Lett. 33, 2185-2187 (2008)

49. Peter T. Rakich, Milos A. Popovic, Michael R. Watts, Tymon Barwicz, Henry I. Smith, and Erich P. Ippen, "Ultrawide tuning of photonic microcavities via evanescent field perturbation," Opt. Lett. 31, 1241-1243 (2006)

50. Ian W. Frank, Parag B. Deotare, Murray W. McCutcheon, and Marko Lončar, "Programmable photonic crystal nanobeam cavities," Opt. Express 18, 8705-8712 (2010)

51. G. S. Wiederhecker, S. Manipatruni, and M. Lipson, "Giant optomechanical tuning of optical cavities," in Conference on Lasers and Electro-Optics/International Quantum Electronics Conference, OSA Technical Digest (CD) (Optical Society of America, 2010), paper CThJ6.

52. Wiederhecker, G. S., Chen, L., Gondarenko, A. & Lipson, M. Controlling photonic structures using optical forces. Nature 462, 633–636 (2009).

53. Yoshitomo Okawachi, Mark Foster, Jay Sharping, Alexander Gaeta, Qianfan Xu, and Michal Lipson, "All-optical slow-light on a photonic chip," Opt. Express 14, 2317-2322 (2006)

54. G. A. Keeler , B. E. Nelson , D. Agarwal , C. Debaes , N. C. Helman , A. Bhatnagar and D. A. B. Miller "The benefits of ultrashort optical pulses in optically-interconnected systems", IEEE J. Sel. Topics Quantum Electron., vol. 9, pp. 477 2003.

55. D. Agarwal , G. A. Keeler , C. Debaes , B. E. Nelson , N. C. Helman and D. A. B. Miller "Latency reduction in optical interconnects using short optical pulses", IEEE J. Sel. Topics Quantum Electron., vol. 9, pp. 410 2003.

56. G. A. Keeler , B. E. Nelson , D. Agarwal and D. A. B. Miller "Skew and jitter removal using short optical pulses for optical interconnection", IEEE Photon. Technol. Lett., vol. 12, pp. 714 2000.

57. J. H. Collet , F. Caignet , F. Sellaye and D. Litaize "Performance constraints for onchip optical interconnects", IEEE J. Sel. Topics Quantum Electron., vol. 9, pp. 425 2003.

58. S. Strogatz, Sync: The Emerging Science of Spontaneous Order (Hyperion, New York, 2003).

59. Mancini, V. Giovannetti, D. Vitali, and P. Tombesi, Phys. Rev. Lett. 88, 120401 (2002).

60. P. Dong, S. F. Preble, J. T. Robinson, S. Manipatruni, and M. Lipson, Phys. Rev. Lett. 100, 033904 (2008).

61. S. Manipatruni, G. S. Wiederhecker, and M. Lipson, "Synchronization in optomechanical structures," Manuscript in preparation

62. S. Manipatruni, J. T. Robinson, and M. Lipson, Phys. Rev. Lett. 102, 213903 (2009).

Chapter 2

HIGH SPEED MICRORING MODULATORS IN SILICON :

Scaling Single Channel Bandwidth

Abstract: In this section, I show an 18 Gbit/s micro-ring modulator with a radius of 6 microns made on a silicon-on-insulator substrate. To the best of our knowledge, this is the fastest performance for a micro-ring modulator with digital data.

The high speed operation is enabled by engineering the carrier dynamics to overcome the restrictions imposed due to carrier lifetime. Together with the multiplexing scheme, that will be presented in the next chapter (50 Gbit/s), this method enables bandwidth density per micron pitch comparable to ITRS predictions for 2020. Based on electro-dynamic simulations, I also propose an electro-optic device which operates at the photon lifetime limit of the micro-ring cavity. The proposed device can operate at 40 Gbit/s with 12 dB extinction ratio and 2.25 fJ/bit/micron-length power dissipation.

2.1. Introduction

An electro-optic modulator provides a key functionality for delivering large bandwidths using optical interconnects by acting as an interface between electronics and optical interconnections. Efficient, compact and robust, electro-optic modulators can be critical 1) for enhancing the computational functionality of future micro-processors [1] 2) for meeting the energy and bandwidth capacity requirements of future datacom/telecom/consumer electronic requirements [2]. In this chapter, I will present a modulator which

achieves large single channel data rates and modulation density (bandwidth encoded per unit footprint area), to make optical interconnects competitive.

An all-silicon electro-optic modulator can play a critical role in making silicon photonics a viable candidate for on-chip/off-chip interconnects. Since, Silicon lacks the traditional electro-optic functionalities originating from electronic non-linearities; carrier dispersion based mechanisms have been actively pursued. Carrier-dispersion-based electro-optic modulators on silicon-on-insulator (SOI) substrates have been demonstrated based on a MOS capacitor [3], a PIN diode [4-7] or a PN junction [8, 9]. Several key developments have been reportedly recently in integration of electro-optic modulators into electronic circuits.

2.2. Figures-of-Merit of compact electro-optic modulators for interconnect applications

I will first establish figures-of merit for electro-optic modulators from a point of view of electronic-photonic integration.

a. **Speed:** High data rate modulation for a given single optical wavelength is essential for the optical modulators to keep up with the growing bandwidth requirements of the electronic chips. However, data rates need not be scaled to the limits of device speed since there is a penalty associated with data serialization and de-serialization operations.
b. **Scalability:** The proposed modulator should allow a simple, low complexity, low operational overhead multiplexing scheme. As I will demonstrate later, a multiplexing scheme is essential for optics to

compete with electronic interconnects due stringent requirements of bandwidth density per unit pitch length.

c. **Temperature Robustness:** The proposed modulator should be robust to variations in temperature for operating computational environments. 1) Run-time operating temperature shift of 20 K 2) Quiescent temperature shifts of >60 K.
d. **Size:** Compact modulators with operating areas <10 μm^2 are essential to meet the modulation rate to footprint Ratio or bandwidth capacity/(mm^2) for future on-chip optical networks.
e. **Electrical Energy per bit:** The total electrical energy of a modulator including switching energy, state-hold energy, tuning energy must be <100 fJ/bit for meeting the requirements of chip-chip/on-chip interconnects. More conservative estimates must include the energy from the optical insertion loss/bit and transmitter drive electronics.
f. **Optical Insertion Loss (Optical Energy per bit):** The optical insertion loss of the modulator (Optical Power level in ON state/Laser Power) can emerge as the most dominant factor when the electrical energy is optimized. To keep the total system energy low, it is essential to consider the optical insertion losses.

In this thesis, over the next few chapters, I will show experimental demonstration of high speed (18 Gbit/s), scalable (50 Gbit/s, 4 channel WDM), robust (to 20K run time variation), compact (2.5 μm radius), low insertion loss (<0.5 dB device in to out), low energy (<10 fJ/bit switching energy, <300 fJ/bit total energy) modulators.

2.3 Silicon micro-ring electro-optic modulator

Silicon micro-ring modulators are uniquely suited for the needs of chip-chip/on-chip optical interconnect. The unique properties of silicon micro-ring modulators are the size, operating energy, low insertion loss and easy adaptability to a wave length division multiplexing scheme.

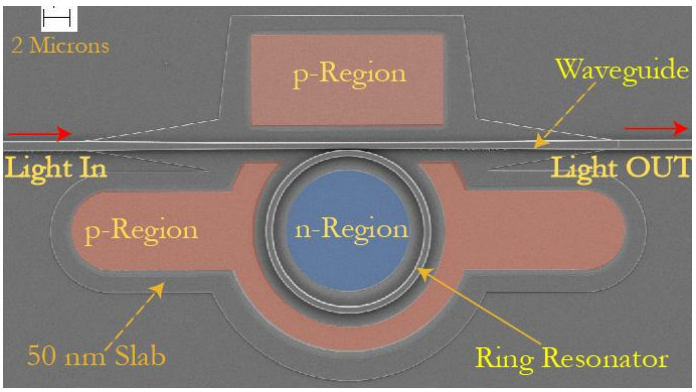

Figure 2.1 SEM image of a 6 μm silicon micro-ring modulator created by embedding a micro-ring in a PIN junction. A 50 nm slab is used to electrically contact the waveguide for carrier transport.

A silicon micro-ring electro-optic modulator is formed by embedding the optical micro-ring cavity in an electrical structure. The electrical structure used in this section is a PIN junction integrated around the micro-ring cavity. The typical ring radii for the micro-ring modulators are between 6 μm and 2.5 μm. The waveguide dimensions forming the cavity are typically 250 nm X 450. The buried oxide thickness is 2-3 μm with a large silicon substrate to provide mechanical support. A 50 nm slab is left in the modulator region to allow for electrical contact to the waveguide. Typical quality factors ($Q = \lambda_0/\Delta\lambda$) range between 5,000 to 40,000. An SEM image of the device is shown in figure 2.1. A schematic of the device is shown in figure 2.2. A

second waveguide can be used as a drop port or to control the optical quality factor when the waveguide losses are pre-determined by the fabrication process.

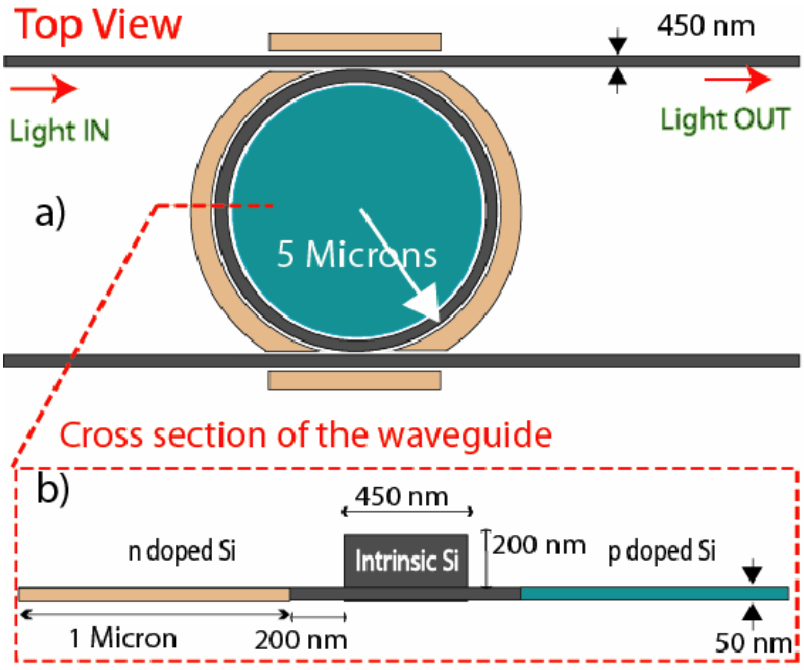

Figure 2.2: Schematic of the micro-ring electro-optic modualtor;
A second waveguide can be coupled to the micro-ring to adjust the optical quality factor for ring for a given cavity intrinsic quality factor

2.4 Modeling a silicon micro-ring electro-optic modulator

The electro-optic modeling for the modulator consists of analyzing the electrical response of the electrical PIN structure and the optical response of the micro-cavity. Among other parameters, the key parameters determining the response are the cavity photon lifetime and carrier recombination lifetime in the wave-guiding region of the diode.

The electrical modeling was carried out in SILVACO device simulation software [10]. The software models the internal physics of the device by numerically solving the Poisson and charge continuity equations. The suitability of SILVACO for simulation of these characteristics has been established by prior works [11-13]. We included Shockley Read Hall (SRH), Auger and direct recombination models. We outline the models and parameters used in Table 2.2; the modeling method is shown in figure 2.3.

Table 2.1 : Typical Device Parameters

Parameter	Typical Value
Micro-ring Radius	10 - 1.5 μm
Waveguide Dimensions	450 nm x 250 nm
Quality Factor ($\lambda_0/\Delta\lambda$)	5000 to 40,000
Slab Height	50 nm
Coupling Distance (Edge to Edge)	200 nm
Carrier Recombination Lifetime (μs)	~ 1 ns -100 ps

The transient optical response of the device is calculated by finite time difference iterative solution of the micro-cavity optical field. The free carrier dispersion of silicon is modeled by the following equations for the refractive index and absorption coefficient for a wavelength of 1.55 μm in silicon [14].

$$\Delta n = \Delta n_e + \Delta n_h = -(8.8\times10^{-22}\Delta n + 8.5\times10^{-18}(\Delta p)^{0.8})$$
$$\Delta\alpha = \Delta\alpha_e + \Delta\alpha_h = 8.5\times10^{-18}\Delta n + 6.0\times10^{-18}\Delta p$$

where Δn is the change in refractive index, Δα is the change in absorption coefficient of intensity, Δn is the injected electron density per cm^3, and Δp is

the injected hole density per $cm^{3.}$ The deviation from the classical Drude model is included in the 0.8 power dependency on the hole concentration which arises due to the non-parabolic shape of the band structure of silicon [15].

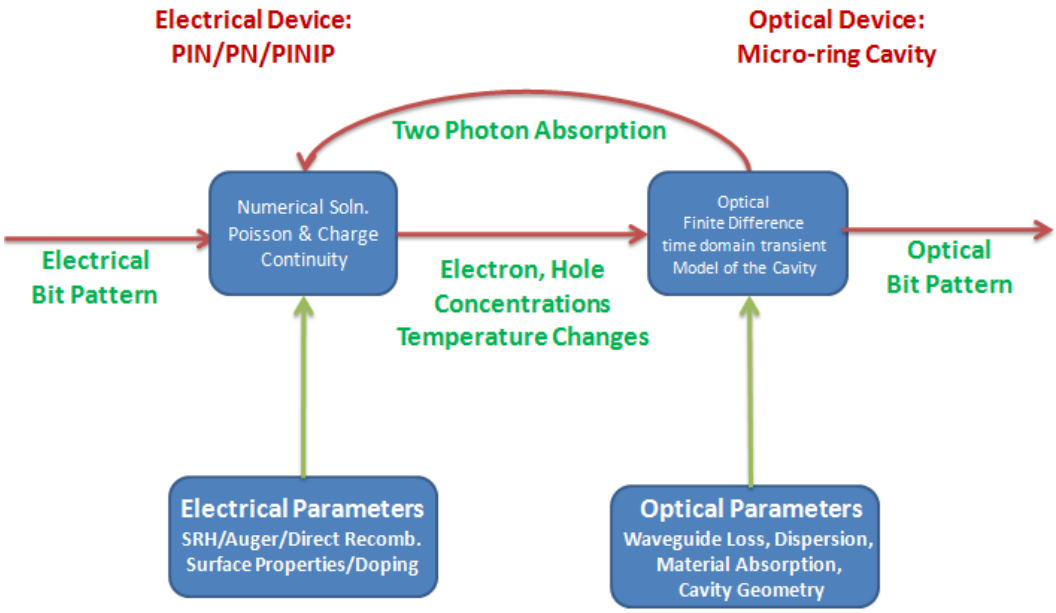

Figure 2.3: Schematic of the eletro-optic modeling scheme.

2.5 18 Gbit/s Operation: Optimizing the speed of a silicon micro-ring electro-optic modulator

The high speed operation of the carrier-injection modulator is enabled by engineering the carrier dynamics to achieve optimal charge injection into the device. In this section, I describe the process through which we can overcome the speed limits imposed by carrier dynamics on injection mode modulators.

Table 2.2 : Electro-optic Simulation Parameters

Electrical Parameter	Typical Value
Intrinsic region doping	$5x10^{15}/cm^3$
N region doping	$10^{19}/cm^3$
P region doping	$10^{19}/cm^3$
N region width	600 nm
Waveguide dimensions (width x height)	450 nm x 250 nm
Bulk silicon electron lifetime (μs)	3 [16]
Bulk silicon hole lifetime (μs)	10 [16]
Carrier surface recombination velocity (cm/s)	10^4 (un-passivated), 100 (passivated) [17, 18]
Carrier surface recombination velocity (cm/s)	10^4 (un-passivated), 100 (passivated) [17, 18]
Interface trap density (cm^{-2} eV^{-1})	10^{10} [18]

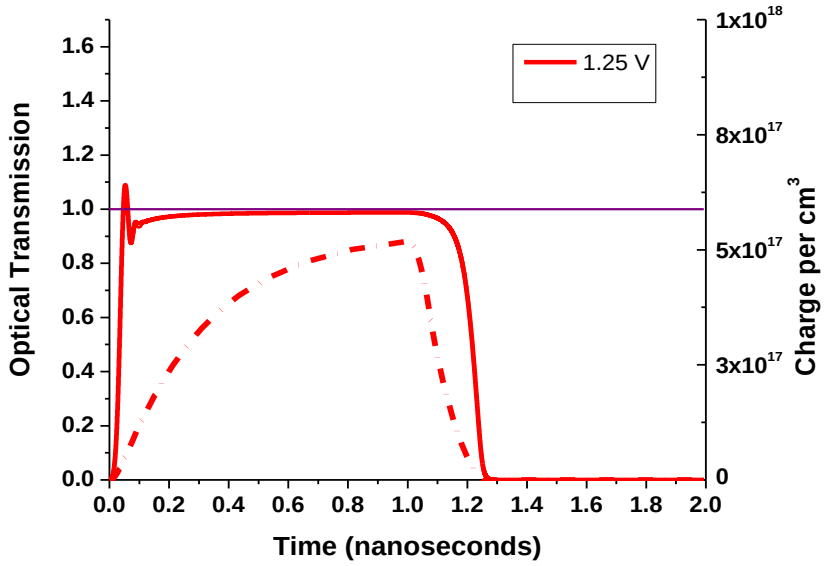

Figure 2.4: Electro-optic response of the micro-ring modualtor; Free carriers in the waveguide are shown in dotted line.

The limitation imposed by carrier dynamics over the operation of carrier injection modulators can be understood as follows: A large turn-on voltage is necessary to enable fast OFF-State to ON-State optical transitions. However, large ON-state voltage leads to excessive injection of the free-carriers. This excessive free carrier concentration reduces the speed of the response due to mobility degradation as well as the requirement to extract the excessive charge. The electro-optic response of the micro-ring modulator to a 1 ns voltage pulse of amplitude 1.25 V is shown in figure 2.4. We see injected carrier density of $5X10^{17}/cm^3$ for electrons and holes.

The electro-optic turn-on transient of the modulator is shown in Figure 2.5. At an applied voltage of 1.25 V, one can see that the optical turn-on can be achieved at 50 ps from the beginning of the transients. To achieve, a 25 ps

turn-on time, we can increase the applied voltage to 2.5 V. However, this significantly affects the turn-off transients, limiting the maximum operation speed of the modulator.

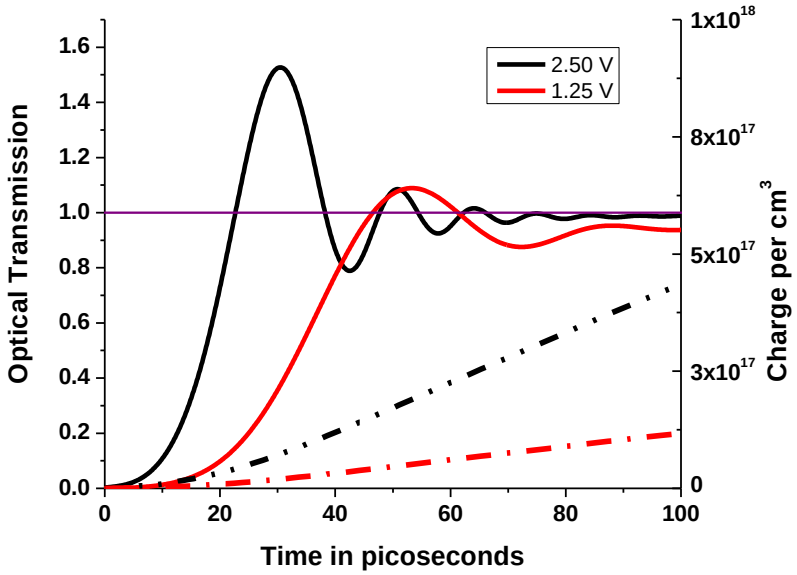

Figure 2.5: The transient optical response is shown by the solid line. The transient at the leading edge is due to the interference between light leaking from the cavity with the light coupled straight through the cavity

As the electro-optic turn ON voltage is increased to obtain faster turn-ON, time taken to extract the free carriers increases (due to mobility degradation) leading to limited speed. We overcome this problem by decoupling the rise and fall time transients.

We achieve simultaneous fast turn-ON and fast turn-OFF by controlling the amount of charge injected into the modulator. By limiting, the injected charge and applied voltage to a value sufficient for fast turn-on, we can decouple the turn-ON and turn-OFF transients.

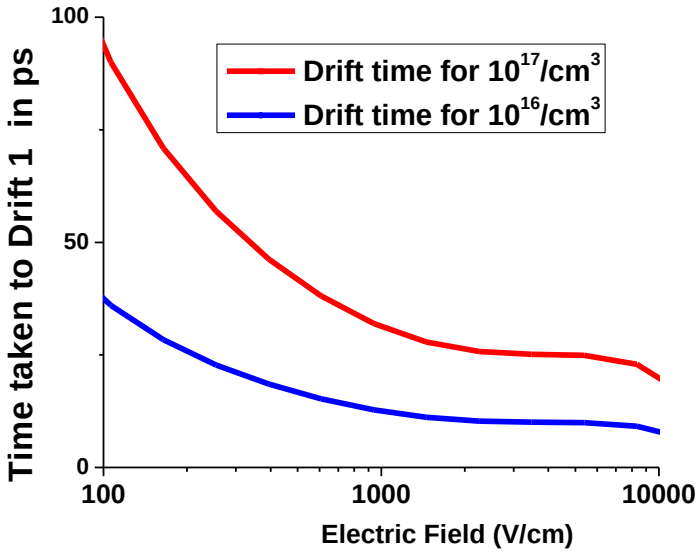

Figure 2.6: Time taken to extract the free carriers for a given applied electric field

We achieve control over the injected charge by engineering the applied voltage into a pre-pulsed Non-Return-Zero pre-pulsed form. The high speed pulse shaping of the applied voltage is achieved as follows.

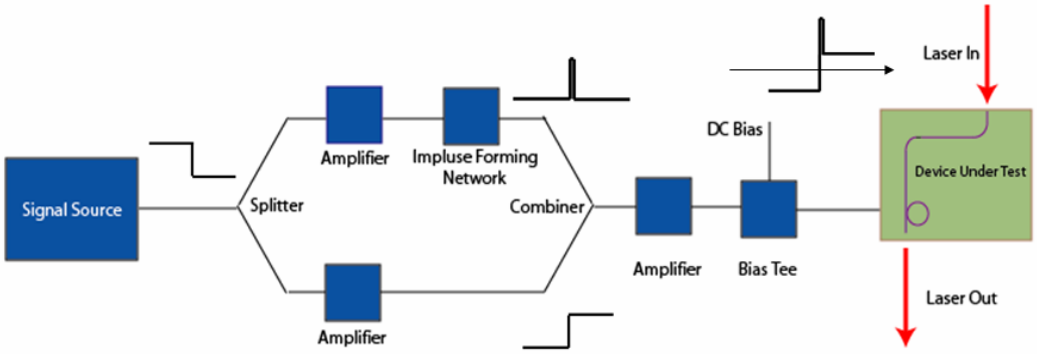

Figure 2.7: Driving mechanism for decoupling carrier rise and fall times of an injection modulator

We implemented a dual-edge pre-emphasis with sub bit period driving circuitry using discrete micro-wave components. For an analog electronic implementation of a pre-emphasis method on silicon at 90 nm technology node please see [1], Page 239. We generated the pre-pulse signals suing an impulse forming network (IFN 5201 [39]) with a transfer function

(Vout=Tc * dVin/dt), where Tc is the derivative time constant. The digital drive signals were pre-amplified using two modulator drivers (JDSU H301) of similar gain and dispersion graphs to amplify the signal in each of the arms. We also used two micrometer controlled low insertion loss 20 GHz delay lines (for e.g SHF 2000DEL) to match the signals in time. The signals were then added with a passive 6 dB coupler. Since, the contact resistance of the PIN diodes is only 500 Ω, we have eliminated the final amplifying stage. However, a 20 Gbps amplifier with a large swing voltage (SHF 826 H [40]) can be used if the contact resistance were to be higher. The eye diagrams and bit patterns at 18 Gbit/s are shown below :

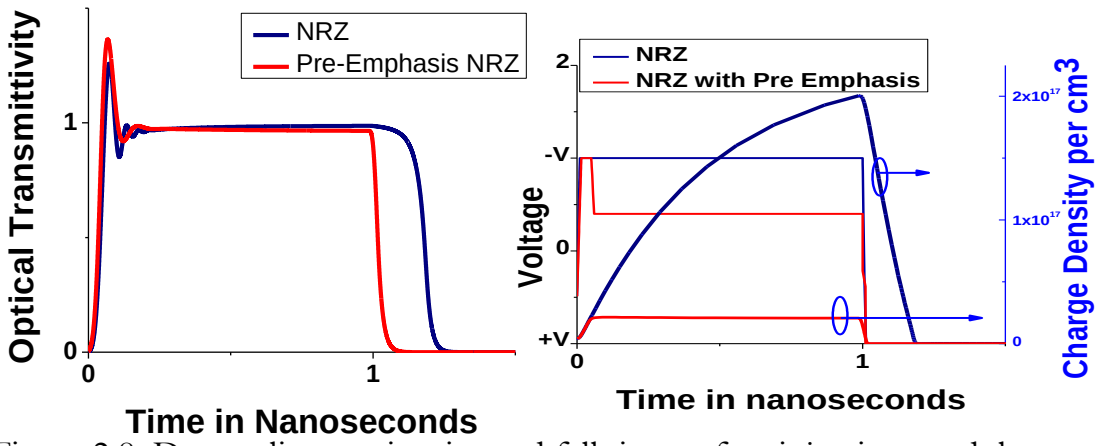

Figure 2.8: Decoupling carrier rise and fall times of an injection modulator

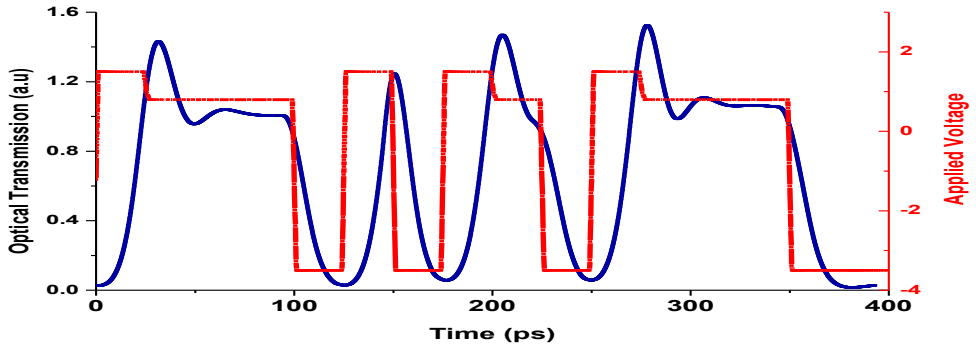

Figure 2.9: 40 Gbit/s operation with pre-pulsing

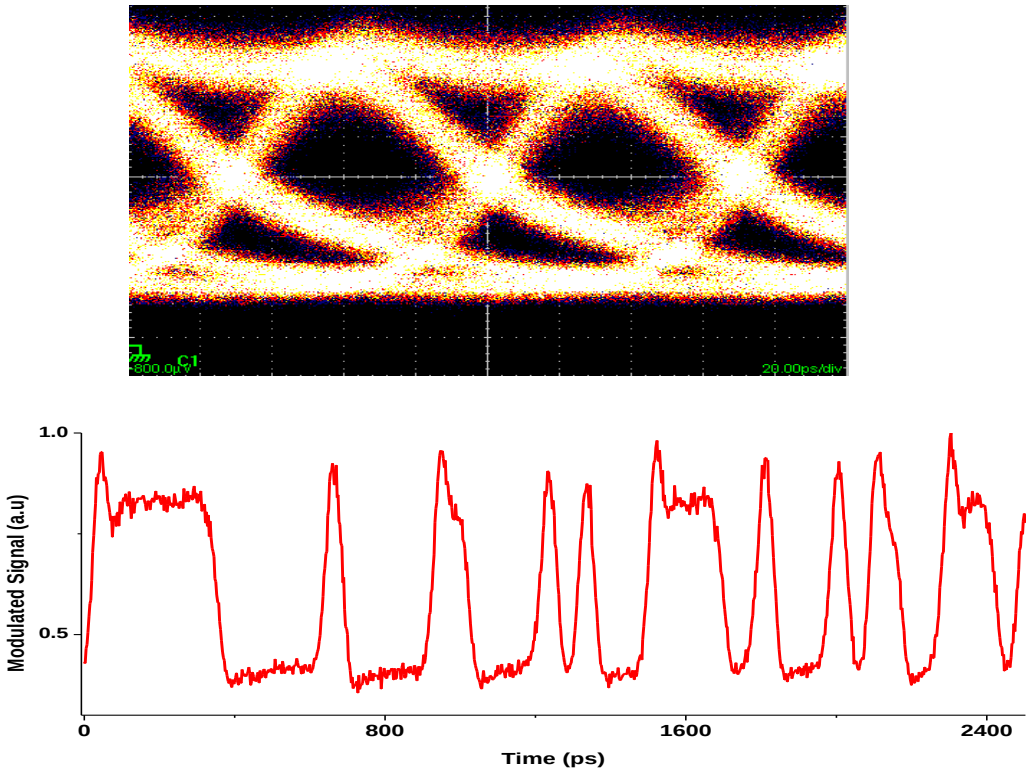

Figure 2.10: a) Measured 18 Gbit/s Modulated Eye Diagram; b) Measured optical bit-pattern at 18 Gbit/s [19]. This operation speed is the fastest digital modulation shown in a micro-ring to date [19]

2.6 Achieving Controlled Charge Injection at the Device Level: Novel modulator geometry for ultra high speed operation

In this section, I extend the idea of controlled charge injection to a device level [20]. I propose an electro-optic device that has an inbuilt charge controlled injection. The proposed device consists of a waveguide embedded in a PINIP device (see Figure. 2.12). The PINIP device provides high speed transitions of carrier density in the waveguide. The refractive index of the waveguide is modulated due to the carrier dispersion effect in silicon. The device cross section is shown in Figure 2.11.

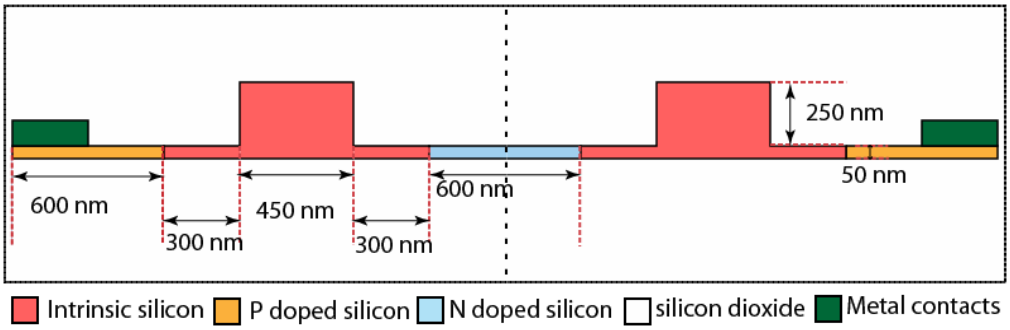

Figure. 2.11 Proposed PINIP device; the device is symmetric about the central dotted line.

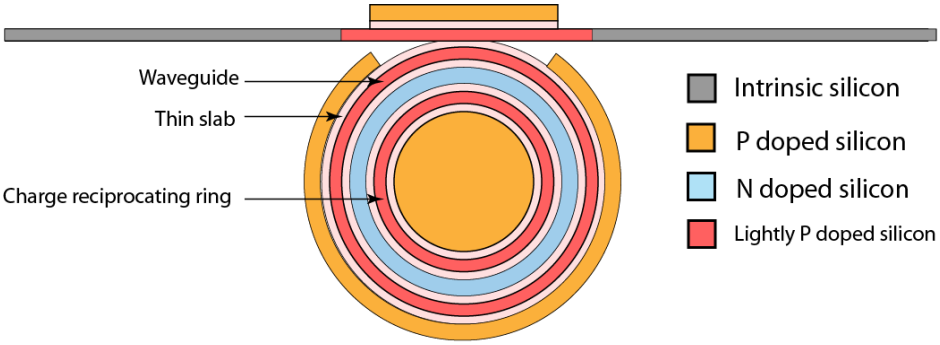

Figure. 2.12 A ring resonator integrated into a PINIP structure

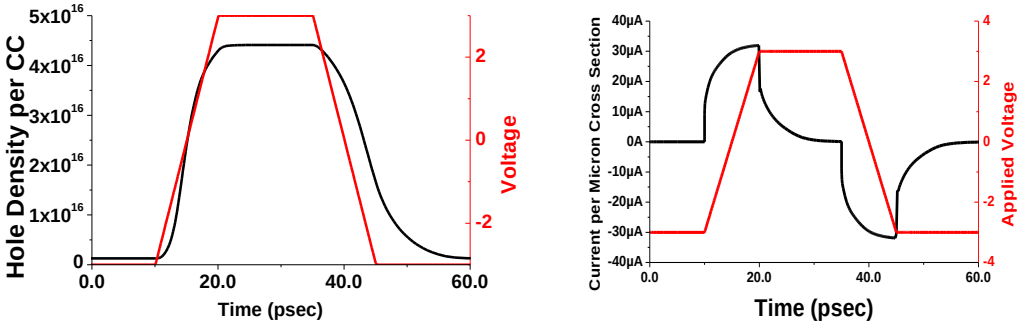

Figure. 2.13 Carrier Density in the center of the ridge, Figure. 2.b Anode Current

The proposed PINIP device consists of two adjacent diodes in opposite directions. The charge transport takes place only during the turn-on and turn-off times of the diodes resulting in fast carrier density changes. The turn-on and turn-off times of the diodes are determined by the time taken for the carriers to form the depletion region as they are swept under high

electric fields. The carriers are accelerated to the carrier terminal velocity in silicon (10^7 cm/s) under electric fields exceeding 10^4 V/cm. By using a symmetric electrical structure for the diodes we produce fast transients during the build up of and depletion of carriers.

The proposed PINIP device operates as a high field transport device where carriers are accelerated through the intrinsic region at the saturation velocity in silicon. This structure has been traditionally used for study of high field behavior of electrons (NIPIN) and holes (PINIP) [21]. Here we propose to use the high field, near saturation velocity transport in PINIP for electro-optic modulation in an SOI photonic device. One of the two ridges shown in Figure. 2.12 is used for guiding light; the other ridge is used as a charge reciprocating structure.

The double ridge structure creates symmetry in the electrical response of the PINIP device. The charge injecting regions are connected to the strip waveguide through a 50 nm thick slab of intrinsic silicon. The entire structure is clad in SiO_2. The charge injecting regions have uniform doping concentrations of $10^{19}/cm^3$. The wave guiding regions are slightly p doped with a typical dopant concentration of $5x10^{16}/cm^3$ so that the carrier density changes are unipolar. This significantly decouples the performance of the device from the time response of recombination of electrons and holes. This is important in order to avoid pattern dependency and timing jitter associated with carrier dispersion devices due to recombination effects.

We simulated the transient electrical and optical characteristics of the device. The electrical transient characteristics show that the PINIP device conducts only during the transition time of the applied voltage thus creating fast electrical transitions. In Figure. 2.13 (a) we show the carrier density at the center of the waveguide for an applied voltage of ± 3 V with 10 ps rise and 15 ps fall times. In Figure. 2.13 (b) we show the anode current per micron length of the device.

The asymmetry in the rise and fall times is due to the non- uniform distribution of the electric field in the intrinsic region. The rise time is determined by the transit time of carriers from the thin slab region to the center of the waveguide region. The electric field in the slab region is higher than the electric field in the waveguide region, leading to a faster rise time (10 ps) as compared to the fall time.

2.6.1. High bit rate operation

We have simulated the structure and showed electro-optic modulation at 40 Gbit/s in an NRZ scheme with a resonator of quality factor 5,000. A relatively low quality factor resonator is used since in the absence of electrical fall time limitations, the speed of modulation is now given only by the cavity ring–down time.

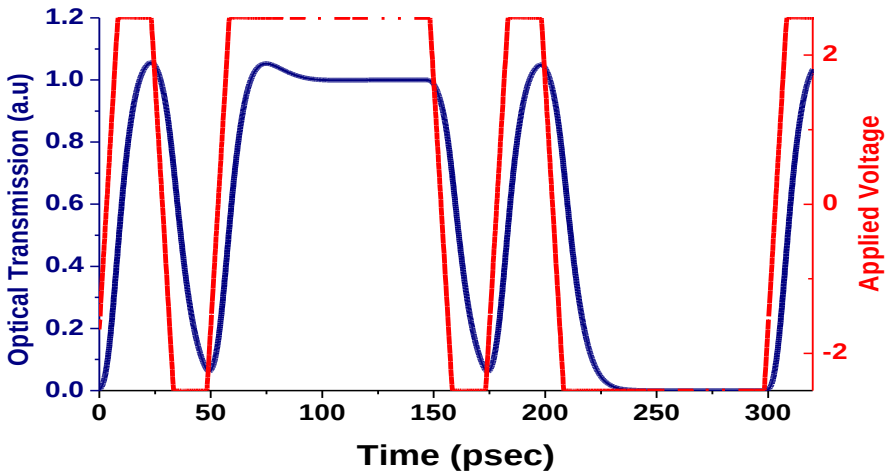

Figure. 2.17. Optical output for a Non-Return to Zero coded bit stream at 40 Gbit/s.

The proposed device extends the speed of carrier injection modulators from a few Gb/s to as high as 40 Gb/s. Figure 2.17 shows the applied voltage and corresponding optical transmission profile for an arbitrary bit sequence modulated with an extinction ratio (defined as 10 $\log_{10}$ (P_{high}/P_{low})) of 12 dB at 40 Gbit/s. We assumed a loss of 8 dB/cm in the ring under critical coupling conditions. The insertion loss is 3 dB at 40 Gbit/s with a peak injection of 5 x 10^{16} cm^{-3}. The insertion loss and extinction ratio can be improved by optimizing the doping profiles or by designing the filter shape using multiple rings [28, 29] or a single add-drop ring filter [30].

The maximum sequence of ones (logic high bits) that the device can modulate is >>1000 bits. The length of identical bit sequence is limited only by the storage time of carriers determined by the leakage current of the device making this an ideal component for on- chip modulation for intra chip communication. The estimated power dissipation of the device is 2.25

fJ/bit/micron length. The energy per bit is estimated from the total charge injected per bit per micron length of the waveguide (0.9 fC/bit/micron) multiplied by the switching voltage (5 V) and the bit transition probability (0.5). The modulator does not draw current while the state is being held except for the parasitic leakage current. This is in contrast to PIN devices where the recombination of carriers has to be compensated with a steady state current inversely proportional to the carrier lifetime. The compact size also avoids the need for traveling wave electrodes and reduces the drive current requirements. The modulator can be driven by an analog CMOS driving circuit made on the same SOI substrate [31]. Hence, the PINIP device can increase the modulation rate beyond 40 Gbit/s limited only by the photon lifetime of the cavity. The device shows electrical transitions of 10 ps which is close to the fundamental limit imposed by carrier saturation velocity in silicon for the dimensions dictated by the index contrast in an SOI system. We show 40 Gbit/s operation with a 12 dB extinction ratio and 2.25 fJ/micron energy dissipated per bit in a 10 micron-sized device limited only by the photon lifetime of the structure.

2.7. Conclusion

In summary, methods for increasing the speed of operation of silicon micro-ring modulators are presented here. I have shown a 18 Gbit/s modulation in a silicon micro ring as well as a novel device to achieve 10 ps transition times allowing for ultra high speed modulation limited only by the saturation velocity of free carriers in silicon.

REFERENCES

1. International Technology Roadmap for Semiconductors (ITRS 2009).

2. Emmanuel B. Desurvire, "Capacity Demand and Technology Challenges for Lightwave Systems in the Next Two Decades," J. Lightwave Technol. 24, 4697-4710 (2006)

3. A. Liu, R. Jones, L. Liao, D. Samara-Rubio, D. Rubin, O. Cohen, R. Nicolaescu, and M. Paniccia, "A highspeed silicon optical modulator based on a metal-oxide-semiconductor capacitor," Nature 427, 615-618 (2004).

4. Q. Xu, B. Schmidt, S. Pradhan, and M. Lipson, "Micrometre-scale silicon electro-optic modulator ", Nature, 435, pp. 325-327, (2005)

L. Zhou and A. W. Poon, "Silicon electro-optic modulators using p-i-n diodes embedded 10-micron-diameter microdisk resonators," Opt. Express 14, 6851-6857 (2006)

5. B. Schmidt, Q. Xu, J. Shakya, S. Manipatruni, and M. Lipson, " Compact electro-optic modulator on silicon-on-insulator substrates using cavities with ultra-small modal volumes," Opt. Express 15, 3140-3148 (2007)

F. Gan and F. X. Kärtner, "High-Speed Electrical Modulator in High-Index-Contrast (HIC) Si-Waveguides," in Conference on Lasers and Electro-Optics, Technical Digest (CD) (Optical Society of America, 2007), CMG1.

6. G. Gunn, "CMOS photonicsTM - SOI learns a new trick," in Proceedings of IEEE International SOI Conference Institute of Electrical and Electronics Engineers, New York, (2005), 7-13.

7. A. Liu, L. Liao, D. Rubin, H. Nguyen, B. Ciftcioglu, Y. Chetrit, N. Izhaky, and M. Paniccia, "High-speed optical modulation based on carrier depletion in a silicon waveguide," Opt. Express 15, 660-668 (2007)

8. SILVACO International, 4701 Patrick Henry Drive, Bldg. 1, Santa Clara, CA 94054

9. C. A. Barrios, V. R. Almeida, R. Panepucci, and M. Lipson, "Electrooptic modulation of silicon-on-insulator submicrometer size

waveguide devices," J. Lightwave Technol. 21, 2332 - 2339 (2003).

10. P. D. Hewitt and G. T. Reed, "Improved modulation performance of a silicon p-i-n device by trench isolation," J. Lightwave Technol. 19, 387 (2001).

11. B. Jalali, O. Boyraz, D. Dimitropoulos, V. Raghunathan, "Scaling laws of nonlinear silicon nanophotonics" Proc. SPIE, 5730, 41-51 (2005).

12. R. Soref, B. Bennett, "Electrooptical effects in silicon," IEEE J. Quantum Electron., 23, 123- 129 (1987)

13. H. C. Huang, S. Yee, and M. Soma, " Quantum calculations of the change of refractive index due to free carriers in silicon with nonparabolic band structure," J. Appl. Phys. , (1990) -- 67, Issue 4, 2033-2039

14. T. Kuwayama, M. Ichimura, E. Arai, "Interface recombination velocity of silicon-on-insulator wafers measured by microwave reflectance photoconductivity decay method with electric field," Appl. Phys. Lett. 83, 928-930, (2003)

15. Palais, A. Arcari, "Contactless measurement of bulk lifetime and surface recombination velocity in silicon wafers," J. Appl. Phys. 93, 4686-4690, (2003)

16. Pierret, R. F. Advanced Semiconductor Fundamentals. 1987 Addison-Wesley Longman Publishing Co., Inc.

17. S. Manipatruni, Q. Xu, B. Schmidt, J. Shakya, and M. Lipson, "High Speed Carrier Injection 18 Gb/s Silicon Micro-ring Electro-optic Modulator," LEOS 2007, IEEE LEOS 2007 Annu. Meeting, Paper WO2, 537-538 (2007).

18. S. Manipatruni, Q. Xu, and Michal Lipson, "PINIP based high-speed high-extinction ratio micron-size silicon electrooptic modulator," Opt. Express 15, 13035-13042 (2007).

19. H. W. Lutz, , a, A. Schwanhäußerb, M. Eckardtb, L. Robledob, G. Döhlerb and A. Seilmeier, "High-field electron transport in

GaAs/AlxGa1−xAs p–i–n–i–p-structures investigated by ultrafast absorption changes", Physica E: Low-dimensional Systems and Nanostructures 13, Issues 2-4, (2002), 802-805

20. V. R. Almeida, C. A. Barrios, R. R. Panepucci, and M. Lipson, Nature 431, 1081 (2004).

21. A. Yariv, "Universal relations for coupling of optical power between micro resonators and dielectric waveguides" Electron. Lett., 36, 4 (2000)

22. Q. Xu, S. Manipatruni, B. Schmidt, J. Shakya, and M. Lipson, " 12.5 Gbit/s carrier-injection-based silicon micro-ring silicon modulators," Opt. Express 15, 430-436 (2007)

23. Bedair, S.M.; McDermott, B.T.; Reid, K.G.; Neudeck, P.G.; Cooper, J.A., Jr.; Melloch, M.R., " Extremely low-leakage GaAs P-i-N junctions and memory capacitors grown by atomic layer epitaxy" Electron Device Letters, IEEE 11, Issue 6, (1990) 261 – 263

24. Yamada, K.; Nakamura, K.; Horikawa, H. , "Electroabsorption modulator with PINIP structure", Electron. Lett., 34, Iss.3, (1998) 304-306

Little, B.E.; Chu, S.T.; Haus, H.A.; Foresi, J.; Laine, J.-P. , "Microring resonator channel dropping filters", J. Lightwave Technol., 15, Iss.6, (1997) 998-1005

25. Emelett, S. & Soref, R. Analysis of dual-microring-resonator cross-connect switches and modulators. Opt. Express 13, 7840–7853 (2005).

26. Little, B.E.; Foresi, J.S.; Steinmeyer, G.; Thoen, E.R.; Chu, S.T.; Haus, H.A.; Ippen, E.P.; Kimerling, L.C.; Greene, W. , "Ultra-compact Si-SiO2 microring resonator optical channel dropping filters", IEEE Photon. Technol. Lett., IEEE, 10, Iss.4, (1998) 549-551

27. T.K. Woodward; A.V. Krishnamoorthy; K.W. Goossen; J.A. Walker; B. Tseng; J. Lothian; S. Hui; R. Leibenguth, "Modulator-driver circuits for optoelectronic VLSI", IEEE Photon. Technol. Lett., 9, Issue 6, (1997) 839 – 841

Chapter 3

50 GBIT/S WAVELENGTH DIVISON MULTIPLEXING USING SILICON MICRORING MODULATORS:

Scaling the interconnect density of nanophotonic interconnects

Abstract— we demonstrate 50 Gbit/s modulation using four silicon micro-ring modulators within a footprint of 500 $(\mu m)^2$. This is the highest total modulation capacity shown in silicon using compact micro-ring modulators.

3.1 Scaling the data rates of nano-photonic interconnects

On-chip optical networks in silicon are evolving as enablers for highly scalable multi-core multi-processors [1-6]. Data rate of interconnects must scale aggressively to meet the bandwidth density (Gbit/s·micron) and footprint requirements of on-chip networks [7-8]. Hence, it is of great interest to pursue scaling techniques for bandwidths achievable on a single optical link using compact modulators.

Here, we show 50 Gbit/s per waveguide modulation capacity in a silicon photonics platform with a footprint of less than 500 $(\mu m)^2$. We use four wavelength specific silicon micro-ring based modulators each operating at 12.5 Gbit/s. Multi Gbit/s silicon electro-optic modulators have been demonstrated based on a MOS capacitor [9], a PIN diode [10-13] or a PN junction [14-16]. However, single electro-optic device data rates are fundamentally limited owing to carrier transport [17], photon lifetime [18]

and signal integrity limits [19]. Here, we extend the high speed modulation abilities of compact silicon microrings to multiple wavelengths to scale the bandwidth per waveguide beyond single device limits.

We show an interconnect bandwidth density (bandwidth of interconnect/width of interconnect) of ~25 Gbit/s·micron (50 Gbit/s/2 μm). This is several times the bandwidth density requirements for global interconnects for a 32 nm node in 2015 as per ITRS (assuming 96 nm wide metal interconnects at 2 Gbit/s) [1]. This is also exceeds the bandwidth density of optimally repeated global on-chip electrical interconnects today by at least an order of magnitude [20, 21].

The modulation rate to footprint ratio, a critical figure of merit for optical networks on chip, of this scheme is three orders of magnitude higher than previously demonstrated by using a parallel bank of Mach-Zhender modulators [22]. These modulation rate to foot print ratios (100 Tbit/s·mm^2) can meet the aggressive real estate demands for optical networks for multi-chip multi-processors [4].

3.2 Wavelength Divison Multiplexing for On-chip Interconnects

Wavelength Divison Multiplexing (WDM) is ideally suited for an on-chip optical interconnect due to complexity, foot print and implementation considerations. This can be arrived at, as follows: in general, three basic multiplexing schemes can be conceptualized for an on-chip optical interconnect viz. a) Space Divison Multiplexing (SDM) b) Time Divison

Multiplexing (TDM) c) Wavelength Divison Multiplexing (WDM). The scalability of SDM and TDM are severely limited on an on chip planar integrated circuit. SDM scalability is limited by the problem of efficiently crossing multiple waveguides, multiple times with low cross talk and insertion losses [23, 24]. TDM based systems are limited fundamentally by the speed of response of the semiconductors [17] and the foot print and power requirements of serialize and de-serialize circuits.

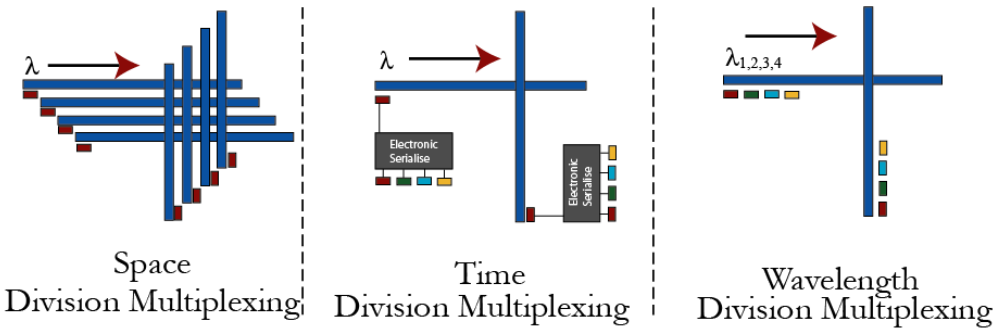

Figure 3.1: Methods for scaling optical interconnect modulation bandwidths. Three basic methods a) space division multiplexing (SDM) b) Time divison multiplexing (TDM) c) Wavelength division multiplexing (WDM). Footprint and waveguide crossings prohibit an aggressive SDM. Serialise and deserialise operations limit TDM.

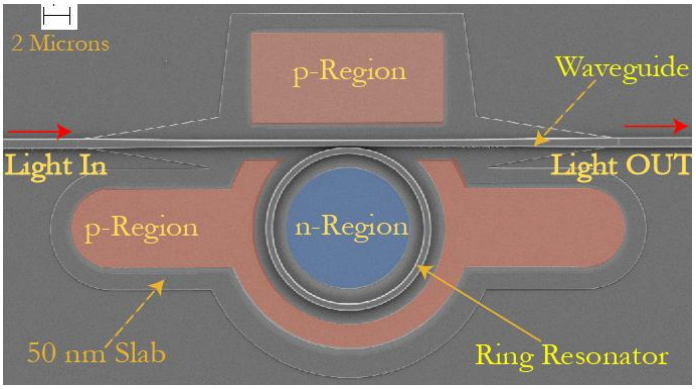

Figure 3.2: SEM image of a 6 μm silicon micro-ring modulator created by embedding a micro-ring in a PIN junction.

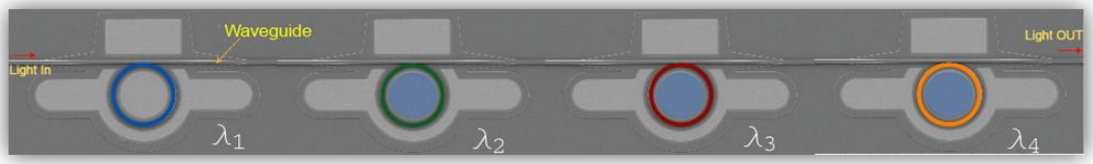

Figure 3.3: 4 microring modulators in an array

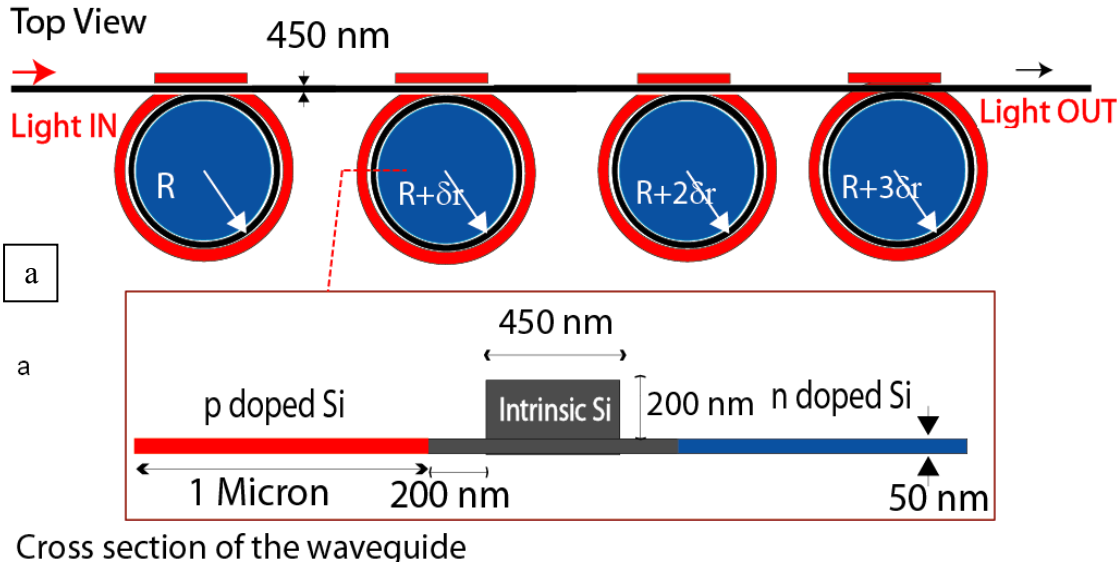

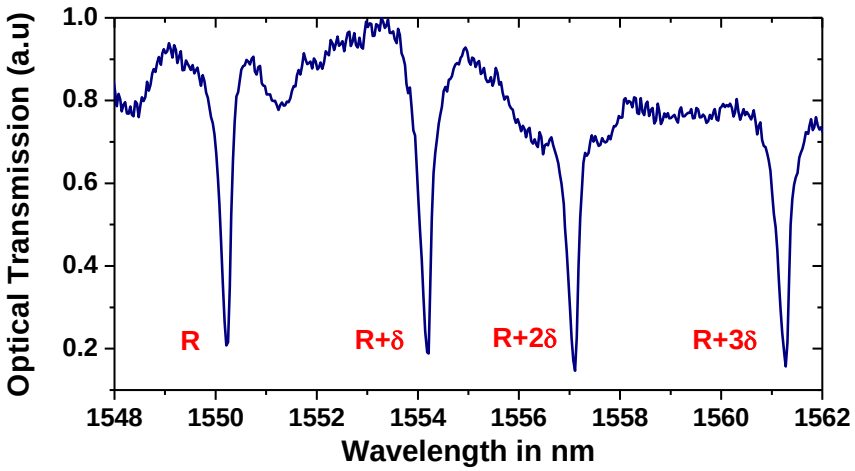

Figure 3.4: a) Schematic of 4 microring modulators coupled to a single waveguide. b) Transmission spectra of 4 microring modulators for quasi-TE polarised light.

Silicon microrings are well suited for WDM due to the wavelength selectivity

of the microrings [25] A silicon micro-ring modulator utilizes free carrier dispersion of silicon to modulate an optical carrier of a specific wavelength decided by the ring geometry. A complete WDM interconnect can be implemented by using a resonator embedded detector.

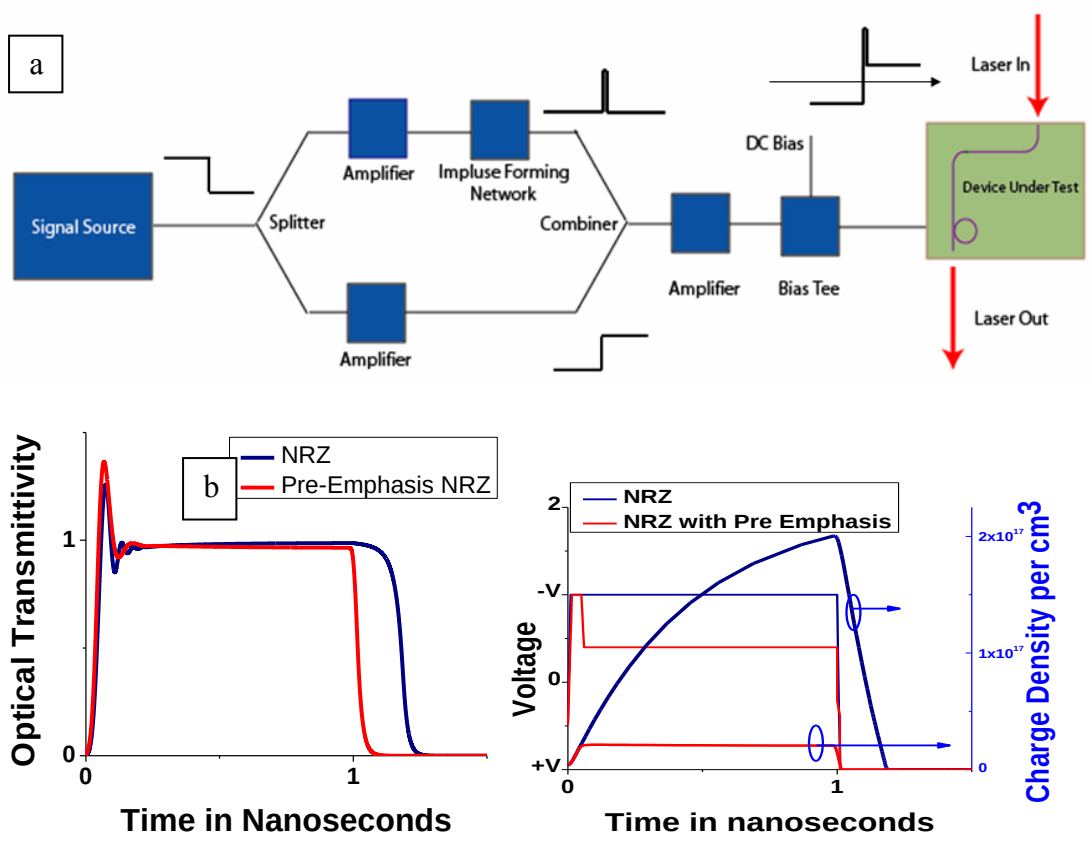

Figure 3.5: a) Driving mechanism for decoupling carrier rise and fall times of an injection modulator b) Carrier density dynamics inside the silicon waveguide b) Driving voltage applied to the modulator with a peak-peak voltage swing of 3V.

We use micro-rings of varying radii to obtain 4 modulators operating at distinct wavelengths. The radii of the rings are controlled through fabrication of sets of 20, 40 and 60 nm differences in circumference (Figure. 3). These microrings are defined on an SOI substrate. The top silicon layer (260 nm thick) is used for the passive waveguides and the electro-optical microring modulator. The patterning steps are all performed with electron-beam

lithography (JEOL 9300). We defined the silicon waveguides and the ring resonator lithographically and then partially etched the silicon layer to a depth of 210 nm. Another lithography step was used to cover the modulator region and continue the silicon etch, leaving the 50 nm slab only around the modulator for the PIN diodes. After the etching we deposited 20 nm SiO_2 for silicon passivation. Next, we performed the implantation steps for the p-region (outside the rings, BF_2, dose $3X10^{15}/cm^2$ at 45 keV) and n-region (inside the ring, Phosphorous, dose $2X10^{15}/cm^2$ at xx) respectively. A relatively low temperature anneal (650°C Rapid Thermal Anneal (RTA) for 120s) was subsequently used to activate the dopants. Nickel Silicide was then used for the electrical contacts to the modulator, with 15 nm evaporated nickel and 50 s RTA at 550°C. We then deposited 1 μm SiO_2 top cladding, and patterned via holes and contact pads connecting to the electrodes of the modulator and detector respectively. The sample was then diced and facet-polished to sub-wavelength roughness for testing.

Each modulator is driven by a pre-emphasis method to decouple the injection and extraction times of the device [26]. The driving scheme and applied pre-pulsed signals are shown in figure 4 a. A peak to peak driving voltage of 3 V is used to obtain 12.5 Gbit/s operation on each of the four devices. Figure 4 b shows the carrier density dynamics inside the waveguide simulated using SILVACO device simulator [18]. One can see that pre-pulsing allows for both a fast turn-on as well as a fast turn-off.

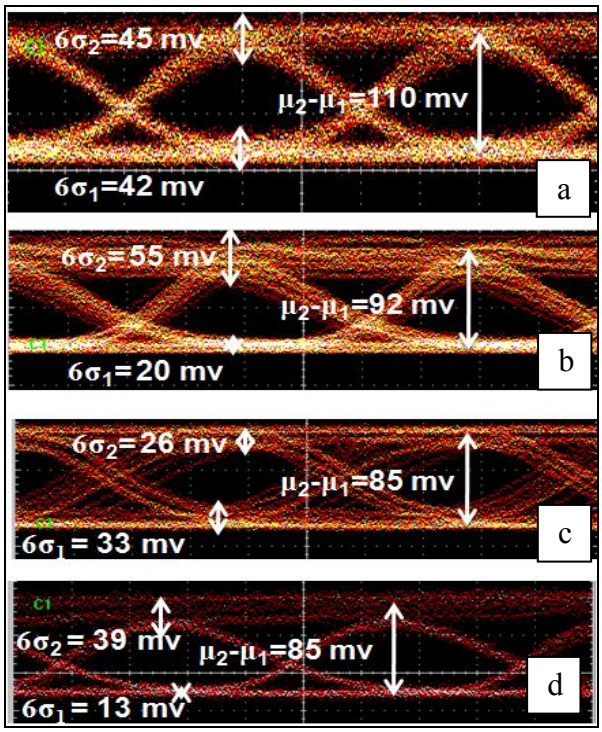

Figure 3.6: Optical eye diagrams at 12.5 Gbit/s for 4 micro-ring modulators at a)1562.29 nm b)1558.14 nm c)1554.97 nm d) 1550.74 nm. The variances in the optical high and low state and difference in powers are measured to estimated the quality factor of the eye diagrams.

We implemented a dual-edge pre-emphasis with sub bit period driving circuitry using discrete micro-wave components. For an analog electronic implementation of a pre-emphasis method on silicon at 90 nm technology node please see [7], Page 239. We generated the pre-pulse signals suing an impulse forming network (IFN 5201 [29]) with a transfer function (Vout=Tc * dVin/dt), where Tc is the derivative time constant. The digital drive signals were pre-amplified using two modulator drivers (JDSU H301) of similar gain and dispersion graphs to amplify the signal in each of the arms. We also used two micrometer controlled low insertion loss 20 GHz delay lines (for e.g SHF 2000DEL) to match the signals in time. The signals were then added with a passive 6 dB coupler. Since, the contact resistance of

the PIN diodes is only 500 Ω, we have eliminated the final amplifying stage. However, a 20 Gbps amplifier with a large swing voltage (SHF 826 H [30]) can be used if the contact resistance were to be higher. We drove the modulators with 50 Ohm terminated high speed probes. Each modulator is driven by a pre-emphasis method to decouple the injection and extraction times of the device. A peak to peak driving voltage of 3 V is used to obtain 12.5 Gbit/s operations on each of the four devices. We note that 3 V drive voltage pre-emphasized signals have been achieved with 1.8V driver supply voltage at 60 nm technology node for high speed operation [1]. The driver biases & pre-emphasis levels are adjusted for each modulator. The extinction ratios for the four-rings are given by the extinction ratios of the static optical transmission measurements (Figure 4).

3.3 Conclusion

We show optical modulation at 4 different wavelengths each at 12.5 Gbit/s. The quality factors of the eye diagrams are estimated as $Q = |\mu_2 - \mu_1|/(\sigma_2 + \sigma_1)$, 7.58, 7.36, 8.64, 9.80 all corresponding to very low bit error rates [31,32]. In conclusion, we show 50 Gbit/s modulation using four silicon microring modulators within a foot print of 500 $(\mu m)^2$. We show interconnect bandwidth density of 25 Gbit/s·micron and modulation bandwidth density of 100 Tbit/s· micron^2, both are critical figures of merit for optical networks on chip. With recent developments towards thermally robust resonant modulators [33-36], scalable modulation methods based on micro-rings may meet the requirements of on-chip optical networks [1-8].

REFERENCES

1. R. Beausoleil, et al, "A Nanophotonic Interconnect for High-Performance Many-Core Computation," in Integrated Photonics and Nanophotonics Research and Applications, (Optical Society of America, 2008), paper ITuD2

2. Haurylau, M. et al, "On-Chip Optical Interconnect Roadmap: Challenges and Critical Directions," Selected Topics in Quantum Electronics, IEEE Journal of , vol.12, no.6, pp.1699-1705, Nov.-dec. 2006

3. A. Benner, M. Ignatowski, J. A. Kash, D. M. Kuchta, M. B. Ritter, "Exploitation of optical interconnects in future server architectures," IBM J. Res. & Dev. 49 (4/5), pp. 755-775 (2005).

4. A. Shacham, K. Bergman, and L. P. Carloni, "On the Design of a Photonic Network-on-Chip," in Networks-on-Chip (2007), pp. 53-64.

5. A. V. Krishnamoorthy, et al, "The integration of silicon photonics and VLSI electronics for computing systems intra-connect", Proc. SPIE 7220, 72200V (2009).

6. Kirman, N.; et al, "Leveraging Optical Technology in Future Bus-based Chip Multiprocessors," Microarchitecture, 2006. MICRO-39. 39th Annual IEEE/ACM International Symposium on , vol., no., pp.492-503, 9-13 Dec. 2006

7. International Technology Roadmap for Semiconductors (ITRS 2007).

8. Davis, J.A.; et al, "Interconnect limits on gigascale integration (GSI) in the 21st century," Proceedings of the IEEE , vol.89, no.3, pp.305-324, Mar 2001

9. A. Liu, et al, "A highspeed silicon optical modulator based on a metal-oxide-semiconductor capacitor," Nature 427, 615-618 (2004).

10. Q. Xu, B. Schmidt, S. Pradhan, and M. Lipson, "Micrometre-scale silicon electro-optic modulator ", Nature, 435, pp. 325-327, (2005)

11. L. Zhou and A. W. Poon, "Silicon electro-optic modulators using p-i-n diodes embedded 10-micron-diameter microdisk resonators," Opt. Express 14, 6851-6857 (2006)

12. B. Schmidt, Q. Xu, J. Shakya, S. Manipatruni, and M. Lipson, " Compact electro-optic modulator on silicon-on-insulator substrates using cavities with ultra-small modal volumes," Opt. Express 15, 3140-3148 (2007)

13. S. J. Spector, et al, "CMOS-compatible dual-output silicon modulator for analog signal processing," Opt. Express 16, 11027-11031 (2008)

14. G. Gunn, "CMOS photonicsTM - SOI learns a new trick," in Proceedings of IEEE International SOI Conference Institute of Electrical and Electronics Engineers, New York, (2005), 7-13.

15. A. Liu, et al, "High-speed optical modulation based on carrier depletion in a silicon waveguide," Opt. Express 15, 660-668 (2007)

16. Watts, M.R.; Trotter, D.C.; Young, R.W.; Lentine, A.L., "Ultralow power silicon microdisk modulators and switches," Group IV Photonics, 2008 5th IEEE International Conference on , vol., no., pp.4-6, 17-19 Sept. 2008

17. Silicon carrier dispersion modulators are ultimately limited by the free carrier–optical phonon interactions. In silicon optical phonon's limit the maximum speed of carriers to 10 ps/μm which limits the maximum bandwidth to ~100 Gbit/s/(transverse carrier transit distance in microns).

18. S. Manipatruni, Q. Xu, and Michal Lipson, "PINIP based high-speed high-extinction ratio micron-size silicon electrooptic modulator," Opt. Express 15, 13035-13042 (2007).

19. Caignet, F.; Delmas-Bendhia, S.; Sicard, E., "The challenge of signal integrity in deep-submicrometer CMOS technology," Proceedings of the IEEE , vol.89, no.4, pp.556-573, Apr 2001

20. C. Batten, et al, "Building Manycore Processor-to-DRAM Networks with Monolithic Silicon Photonics," *High-Performance Interconnects, Symposium on*, pp. 21-30, 16th IEEE Symposium on High Performance Interconnects, 2008.

21. B. Kim and V. Stojanovic, "Equalized interconnects for onchip networks: Modeling and optimization framework". Int'l Conf. on Computer Aided Design, 2007.

22. A. Liu; et al, "200 Gbps photonic integrated chip on silicon platform," Group IV Photonics, 2008 5th IEEE International Conference on , vol., no., pp.368-370, 17-19 Sept. 2008

23. Popovic, M.A.; Ippen, E.P.; Kartner, F.X., "Low-Loss Bloch Waves in Open Structures and Highly Compact, Efficient Si Waveguide-Crossing Arrays," Lasers and Electro-Optics Society, 2007. LEOS 2007. The 20th Annual Meeting of the IEEE , vol., no., pp.56-57, 21-25 Oct. 2007

24. S. G. Johnson, C. Manolatou, S. Fan, P. R. Villeneuve, J. D. Joannopoulos, and H. A. Haus, "Elimination of cross talk in waveguide intersections," Opt. Lett. 23, 1855-1857 (1998)

25. Q. Xu, B. Schmidt, J. Shakya, and M. Lipson, "Cascaded silicon micro-ring modulators for WDM optical interconnection," Opt. Express 14, 9431-9435 (2006)

26. S. Manipatruni, Q. Xu, B. Schmidt, J. Shakya, and M. Lipson, "High Speed Carrier Injection 18 Gb/s Silicon Micro-Ring Electro-Optic Modulator" in Proceedings of IEEE Conference on Lasers and Electro-Optics , Lake Buena Vista , 2007. paper WO2

27. I. Shake, H. Takara, and S. Kawanishi, "Simple Measurement of Eye Diagram and BER Using High-Speed Asynchronous Sampling," J. Lightwave Technol. 22, 1296- (2004)

28. S. Manipatruni, et al, "Wide temperature range operation of micrometer-scale silicon electro-optic modulators," Opt. Lett. 33, 2185-2187 (2008).

29. http://www.picosecond.com/product/product.asp?prod_id=94

30. http://www.shf.de/en/communication/products/rf_broadband_amplifier/40_gbps_rf_amplifier/

31. Shake, H. Takara, and S. Kawanishi, "Simple Measurement of Eye Diagram and BER Using High-Speed Asynchronous Sampling," J. Lightwave Technol. 22, 1296- (2004)

32. A. Biberman*, N. Ophir, K. Bergman, S. Manipatruni*, L. Chen, and M. Lipson, "First Experimental Bit-Error-Rate Validation of 12.5-Gb/s Silicon Modulator Enabling Photonic Networks-on-Chip," in Optical Fiber Communication Conference, OSA Technical Digest (CD) (Optical Society of America, 2010), paper OMI1. (Equal contribution)

33. S. Manipatruni, R. K. Dokania, B. Schmidt, N. Sherwood-Droz, C. B. Poitras, A. B. Apsel, and M. Lipson, "Wide temperature range operation of micrometer-scale silicon electro-optic modulators," Opt. Lett. 33, 2185-2187 (2008)

34. M. Watts, W. Zortman, D. Trotter, G. Nielson, D. Luck, and R. Young, "Adiabatic resonant microrings (ARMs) with directly integrated thermal microphotonics," In Conference on Lasers and Electro-Optics / Quantum Electronics and Laser Science Conference (CLEO/QELS'09), CPDB10, Baltimore, May 31-June 5 (2009).

35. B. Guha, B.B. C. Kyotoku, and M. Lipson, "CMOS-compatible athermal silicon microring resonators," Opt. Express 18, 3487-3493 (2010)

36. P. Dong, S. Liao, D. Feng, H. Liang, R. Shafiiha, N-Ning Feng, G. Li, X. Zheng, A. V. Krishnamoorthy, M. Asghari, "Tunable High Speed Silicon Microring Modulator," In Conference on Lasers and Electro-Optics / Quantum Electronics and Laser Science Conference (CLEO/QELS'10),CTHJ5, San Jose, (2010)

Chapter 4

150 mVpp, 2.5 μm SILICON MICRO-RING MODULATOR: Scaling the voltage and Areal bandwidth density

Abstract: We demonstrate ultra-low swing voltage (150 mV peak-peak) electro-optic modulation in a 2.5 μm radius silicon ring modulator. These results can enable low complexity direct CMOS digital logic driven modulators. These results can enable low complexity drivers using standard CMOS digital drive electronics employing low rail voltages. This is the smallest swing voltage modulation on silicon to-date.

4.1 Introduction

Integration of silicon photonic components with CMOS electronics is an important requirement for on-chip & chip-chip optical interconnect applications [1-7]. In particular, silicon electro-optic modulator operating voltages must scale aggressively as rail voltages (Vdd) for digital VLSI are scaled to 600 mV in future CMOS platforms [8-11]. Hence, it is of great interest to pursue low voltage modulation methods that are silicon compatible. A low voltage swing modulation scheme can significantly reduce the total transmitter energy and footprint by reducing the drive electronic complexity compared to the existing schemes [12]. In this letter, we show GHz modulation in a 2.5 μm radius silicon micro-ring, with only 150 mV peak-peak drive voltage and an electro-optic modal volume of only 2 μm^3.

4.2 Operating Principle for Low Voltage Switching

We achieve the low drive voltage and ultra low switching energy operation by operating the modulator near an optimum charge injection efficiency point of the electro-optic device. This feature is unique to PIN injection modulators enabling ultra low voltage operation in contrast with other techniques for electro-optic structures [13-20]. We support the proposed scheme via electro-optic simulations and analytic models matched closely with transient/steady state modulator measurements. The ultra low driving voltage scheme, combined with the small size of the micro-ring (2.5 μm) can enable low RF switching powers driven directly by scaled CMOS digital logic.

4.3 Ultra Low Voltage Operation

We use a micro-ring of radius 2.5 μm, close to the bending loss limited foot-print of micro-rings [21]. The micro-ring is formed with a waveguide of width 500 nm coupled to 350 nm wide silicon waveguides (figure 1.a). The micro-ring modulators are fabricated on silicon on insulator substrate. The top silicon layer (260 nm thick) is used for the passive waveguides and the electro-optic micro-ring modulator. The patterning steps are all performed with electron-beam lithography (JEOL 9300). We defined the silicon waveguides and the ring resonator and partially etched the silicon layer to a depth of 210 nm. Another lithography step was used to cover the modulator region and continue the silicon etch, leaving the 50 nm slab only around the modulator for the PIN diodes. After the etching, we deposited 20 nm SiO_2 for silicon passivation. Next, we performed the implantation steps for the p-

region (outside the rings, BF_2, dose $3X10^{15}/cm^2$ at 45 keV) and n-region (inside the ring, Phosphorous, dose $2X10^{15}/cm^2$ at 33 keV) respectively. A relatively low temperature anneal (650°C Rapid Thermal Anneal (RTA) for 120s) was subsequently used to activate the dopants. Nickel Silicide was then used for the electrical contacts to the modulator, with 15 nm evaporated nickel and 50 s rapid thermal anneal (RTA) at 550°C. We then deposited 1 μm SiO_2 top cladding, and patterned vias and contact pads connecting to the electrodes of the modulator. The sample was then diced and facet-polished to sub-wavelength roughness for testing. The device and NRZ modulation waveforms are shown in Figure 4.1 where we drove the modulator with Non-Return-to-Zero data at 4 Gbit/s with a peak-peak voltage of 1.4 V biased at 0.5 V.

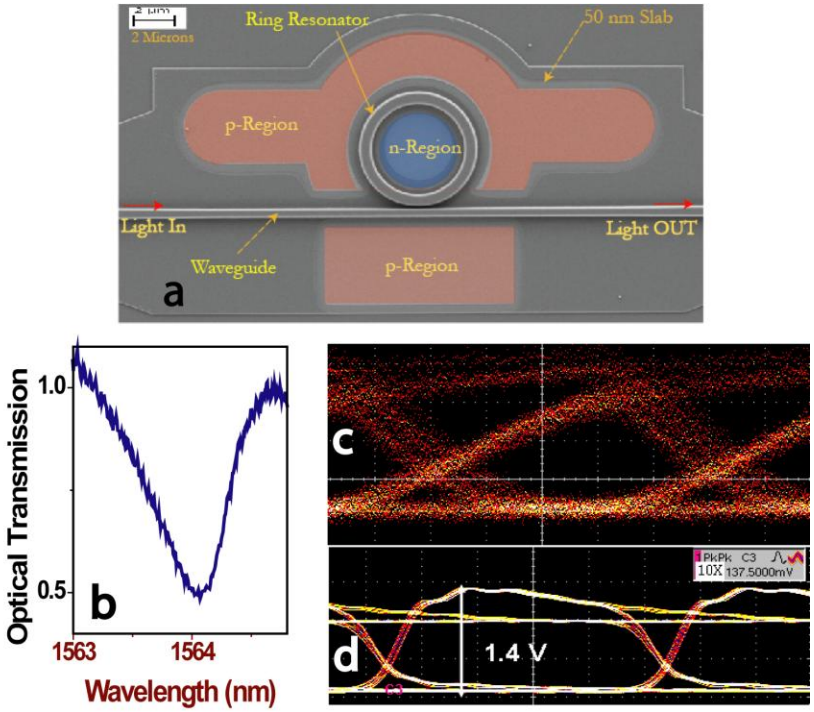

Figure. 4.1 a : SEM image of a 2.5 μm radius silicon micro-ring modulator created by embedding a micro-ring in a PIN junction. b) Optical Transmission Spectrum of the Micro-ring c) NRZ optical eye diagrams at 4 Gbps c) NRZ electrical driving signal at 1.4 V peak-peak biased at 0.5 V.

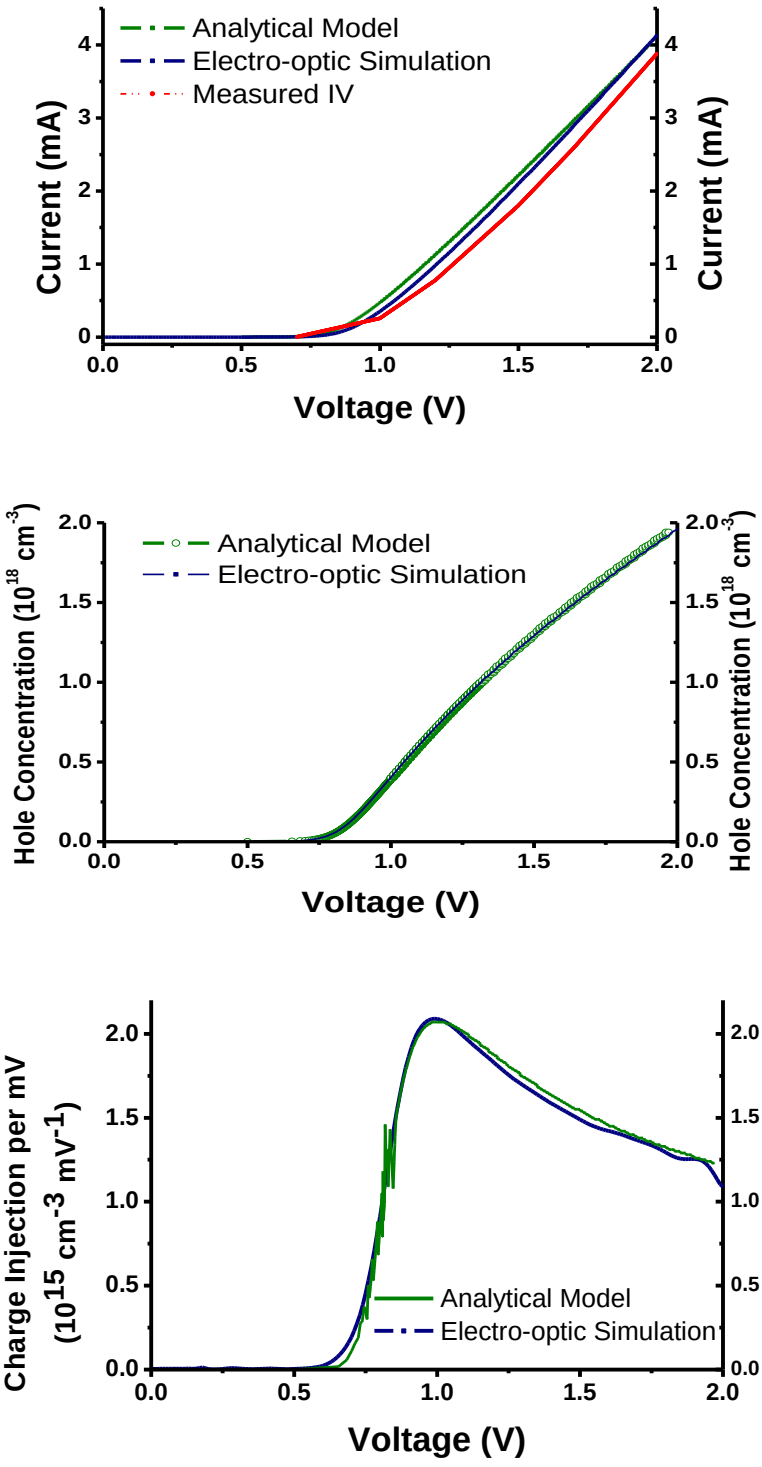

Figure. 4.2 a: Measured and simulated device I-V characteristics (red). b: Electron and hole concentrations in the waveguide (blue) c: Carrier injection per unit voltage (derivative of (b) with respect to voltage)

We achieve very low voltage operation of PIN injection modulators by operating the modulator near an optimum charge injection point. The presence of optimum charge injection region enabling ultra low voltage operation can be understood by considering the carrier lifetimes in forward biased PIN electro-optic modulator. Figure 4.2.a shows the experimental and simulated IV characteristics of the micro-ring modulator. The injected charge density (dQ/dv) in the waveguide centre is shown in Figure 4.2.b.

We explain the presence of optimum charge injection region via an analytic model supported by electro-optic device simulations matched with measured data. The electro-optic simulations are in-turn validated against steady state and transient performance of the modulator. The injected charge into the PIN diode can be extracted from the non-linear governing equation:

$$V(I) = V_t + IR + \frac{kT}{e\alpha}\log_e\left[\frac{I}{I_0} + 1\right] \tag{1}$$

Where I is the steady state current through the PIN diode, R is the total effective series resistance, k, Boltzmann constant, α the non-ideality coefficient of the diode, I0 is the reverse saturation current. In figure 2, we show the analytical solution of the above equation along with the simulated and measured IV data. The fitting parameters are I0 =90 nA, Vt=0.5 V, α = 0.62, R=250 Ω. The injected charge density can be obtained from the V(I) characteristics following the non-linear governing equation for the steady state injected carrier density:

$$Q = I\tau_{recomb} = I\frac{\tau_0}{1+\left(\frac{Q}{Q_0}\right)^n} \tag{2}$$

Where τ_0 is the carrier life time at low carrier densities, n is the power law dependence of the carrier lifetime with injected carrier density, Q0 is a fitting parameter determined by the dependence of carrier lifetime on the minority carrier concentration in the PIN diode. We found n to be 1, indicating a recombination process that scales proportional to the carrier density [22]. The above equation can be obtained by the differential equation for injected charge in the diode at steady state by setting $dQ/dt = Q(t) - I/\tau_{recomb} = 0$. The results from equations (1) and (2) can be combined to obtain the Q (V) and, dQ/dv shown in figure 2 c.

$$\frac{dQ}{dV} = \frac{dQ}{dI} \cdot \frac{dI}{dV} = G(V) \cdot \frac{\tau_0}{1 + \frac{1+Q}{Q_0}} \qquad (3)$$

Where, G(V) is the conductance of the diode obtained from (1). The calculated and simulated charge densities show excellent agreement to verify our assumptions. By biasing the modulator at high injection efficiency points (near the maxima of (3)), one can exploit the high charge injection (fC/mV) of the device to achieve a low voltage operation of the device.

We simulated the transient carrier dynamics of the electro-optic modulator to verify the principle of operation. The electrical modelling was carried out in SILVACO ATLAS device simulation software and the optical modulation was calculated using an optical transmission matrix approach [23]. The software models the internal physics of the device by solving the Poisson equation and the charge continuity equation numerically. We included Shockley Read Hall (SRH), Auger, Direct recombination models. We assumed an interface trap density of $10^{10}/cm^2/eV$ and an interface

recombination rate of 10^4cm/s. The surface recombination rate of silicon is of the order of 10^4 cm/s for un-passivated surfaces and 100 cm/s for passivated surfaces. A detailed treatment of electro-optic modelling is presented in [23]. A good agreement between the measured and simulated waveforms can be observed in figure 4.3.

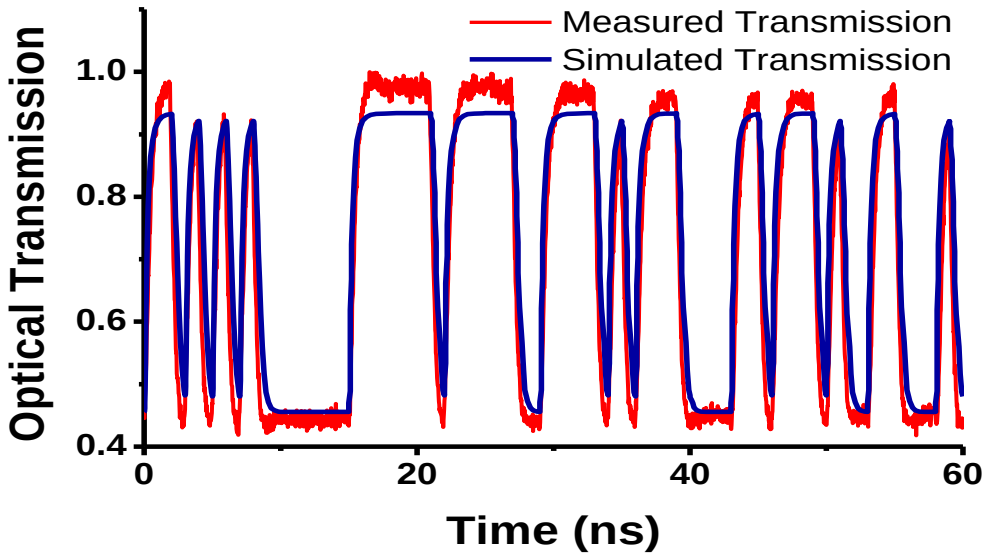

Figure 4.3: Measured and simulated transient electro-optic device characteristics for the proposed operating conditions. The applied voltage is a square wave from 0.96 to 1.11 V.

We demonstrate 1 Gbit/s modulation with a peak-peak drive voltage of only 150 mV. The optical waveform at 1 Gbit/s NRZ is shown in figure 4.4 a. Eye diagrams corresponding to the drive voltage is shown in figure 4.4 b. We drive the electro-optic modulator directly from the pattern generator using a 20 dB attenuator to obtain 150 mV voltage swing. A bias-tee is used to add a variable DC voltage to optimize the optical waveforms. The driving signal is terminated in a 50 ohm termination at the end of the high speed to probes to avoid reflections. A 150 mV voltage swing with a low voltage level

of 960 mV were used to obtain clear waveforms. The optical eye diagram is shown in figure 4.4 b showing an open eye. We observe symmetric rise and fall times of ~ 1 ns corresponding to the recombination life time in silicon waveguides determined predominantly by the surface recombination processes.

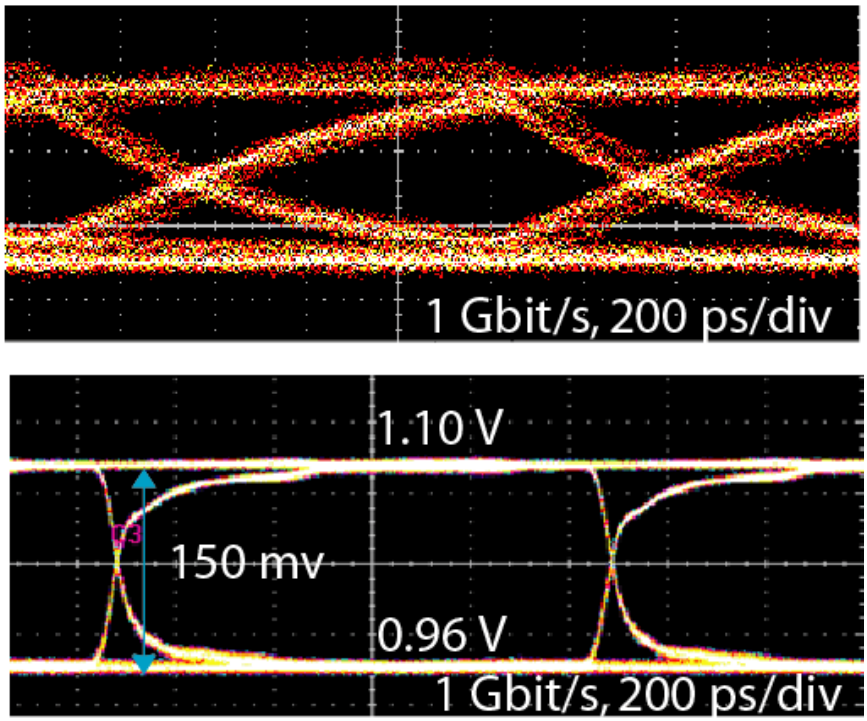

Figure 4.4: Eye diagrams with 150 mV drive voltage at 1 Gbit/s for 2.5 μm micro-ring modulator a) Optical eye diagram b) RF eye diagram with a swing voltage of 150 mV and a bias point at 0.96 V.

We estimate the RF switching power consumed by the device as 7.9 fJ/bit excluding the state hold power. The estimate of the switching power is arrived at as follows: The total charge injection times voltage swing provides the switching energy per injection. However, since 0-0, 0-1, 1-0, 1-1 transitions are all equally likely in a pseudo-random signal, the switching energy per bit is given by 1/4th of the switching energy per transition. The total charge injection for switching is estimated from the optical quality

factor (Q ~ 3000), group index (n_g = 4.262) and modal volume of the cavity (Θ = 1.96 μm^3) and free carrier dispersion in silicon [22]. The refractive index shift required for full optical switching across the ring is obtained from $\Delta n = n_g/Q_{opt} = 1.42X10^{-3}$. This corresponds to an injected charge density of $\varrho = 3.9X10^{17}$ cm^{-3}. Hence the total charge injected is Φ= 251 fC at each 0-1 transition. The energy per injection is therefore 37.7 fJ. However, since 0-0, 0-1, 1-0, 1-1 transitions are all equally likely in a pseudorandom signal [17], the switching energy per bit is given by 7.9 fJ/bit. However, we note that the total energy of the injection modulator is dominated by the DC power consumption given by $V_{on}I_{on} = V_{on}Q/\tau_{recomb}$.

The proposed scheme can enable high speed direct digital logic driven modulators that can be operated with a single stage (or tapered) inverters. We estimated the switching speeds of a scaled single stage digital logic driver for future technology nodes. The maximum switching speed ($f_s = 1/t_s$) for a single stage inverter (Figure 4.5) [26] driven by minimum sized transistors is estimated as:

$$t_{sw} = 3\frac{C_n V_n}{I_n}.\frac{I_{modulator}}{I_n} + 1.5.\frac{C_n V_n}{I_n} \qquad (4)$$

Where C_n,V_n, I_n are the capacitance, voltage and current through minimum sized transistor at a given technology node, $I_{modulator}$ is the peak current through the modulator. We plot the maximum switching speed of the direct logic drive as a function of the drive current for the modulator in figure 5. Gate lengths, voltages and delays are taken from ITRS 2009, Table PIDS2 : High Performance Logic Technology Requirements [27]. One can clearly see

that at 1 mA current levels for the present modulator switching speeds approaching 10 GHz can be realised using direct CMOS digital logic drives.

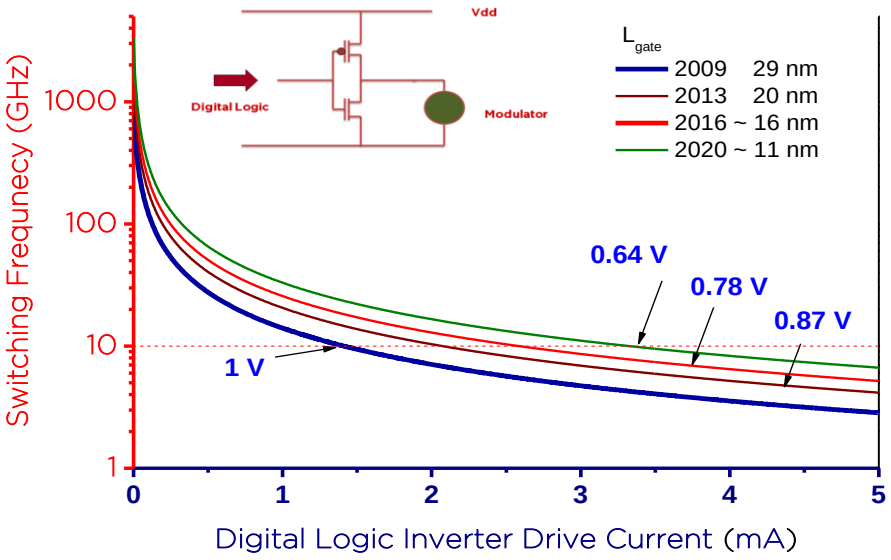

Figure 4.5: Switching frequency of a single staged inverter driven directly with a digital logic level as a function of the drive current.

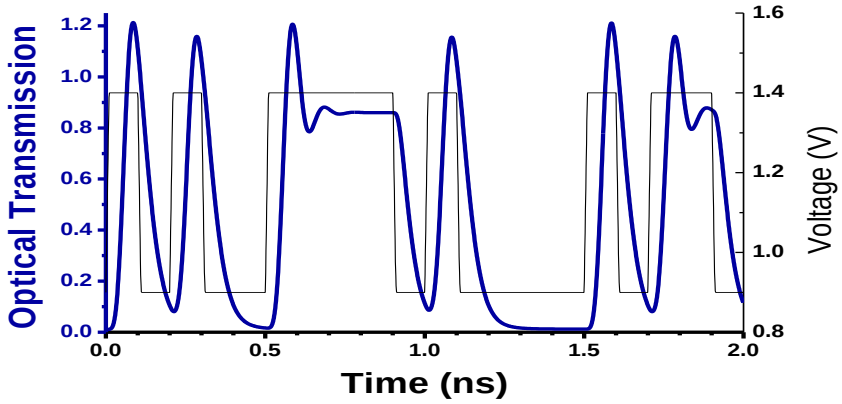

Figure 4.6: Simulation of 10 Gbps electro-optic modulator with 500 mVpp drive voltage. The SRH recombination rate is increased such that the effective carrier lifetime is 100 ps. The diode IV forward bias resistance is 110 ohm. The ring resonator loaded Q is 25,000, corresponding to a modest propagation loss of 17 dB/cm and photon lifetime of 21 ps.

The estimated scaled NMOSFET channel width for a 1 mA drive current is expected to be

$$G_{pmosfet} = G_{node} \cdot \frac{I_{modulator}}{I_{d,sat} \cdot G_{node}} \quad (5)$$

assuming an Id,sat of 664 μA/μm at a 22 nm CMOS technology node [8]. This implies a drive transistor size of 1.5 μm which can scale down with current densities [8]. This reduction in footprint, driver energy, complexity may enable easy integration with CMOS drive electronics. By controlling the carrier lifetime [23], we expect that 10 Gbps, sub 500 mV, direct CMOS digital logic driven modulation will be feasible. In figure 4.6, we show the simulated electro-optic modulation of an electro-optic modulator at 10 Gbps operating with a 500 mV voltage swing. We note that the peak currents were 3 mA, which correspond to a scaled digital inverter cut –off bandwidth of 10 GHz in a 16 nm CMOS node.

In conclusion, we demonstrate ultra-low drive voltage (150 mV) operation of carrier injection micro ring modulators in Gbit/s regime. This low voltage driving scheme allows for direct digital logic driven modulators driven with micron sized transistors. To the best of our knowledge this is the smallest operating voltage (150 mV) for a GHz silicon modulator to date. The mode volume (2 μm^3) & foot-print (~20 μm^2) of the modulator is also the smallest to date for a carrier injection micro-ring silicon modulator. The ability to scale the voltages of modulators down to few 100 mV may enable compatibility with digital CMOS technologies beyond 22 nm.

REFERENCES

1. Young, I.A.; Mohammed, E.; Liao, J.T.S.; Kern, A.M.; Palermo, S.; Block, B.A.; Reshotko, M.R.; Chang, P.L.D.; , "Optical I/O Technology for Tera-Scale Computing," Solid-State Circuits, IEEE Journal of , vol.45, no.1, pp.235-248, Jan. 2010

2. D. A. B. Miller, "Device Requirements for Optical Interconnects to Silicon Chips," Proc. IEEE 97, 1166 - 1185 (2009)

3. A.V. Krishnamoorthy, et al, "The integration of silicon photonics and VLSI electronics for computing systems intra-connect", Proc. SPIE 7220, 72200V (2009).

4. Batten, et al, "Building Manycore Processor-to-DRAM Networks with Monolithic Silicon Photonics," High-Performance Interconnects, Symposium on, pp. 21-30, 16th IEEE Symposium on High Performance Interconnects, 2008.

5. R. Beausoleil, et al, "A Nanophotonic Interconnect for High-Performance Many-Core Computation," in Integrated Photonics and Nanophotonics Research and Applications, (Optical Society of America, 2008), paper ITuD2

6. Shacham, K. Bergman, and L. P. Carloni, "On the Design of a Photonic Network-on-Chip," in Networks-on-Chip (2007), pp. 53-64.

7. Kirman, N.; et al, "Leveraging Optical Technology in Future Bus-based Chip Multiprocessors," Microarchitecture, 2006. MICRO-39. 39th Annual IEEE/ACM International Symposium on , vol., no., pp.492-503, 9-13 Dec. 2006

8. International Technology Roadmap for Semiconductors (ITRS 2009).

9. Y. Q. Shi, C. Zhang, H. Zhang, J. H. Bechtel, L. R. Dalton, B. H. Robinson, and W. H. Steier, "Low (sub-1-volt) halfwave voltage polymeric electro-optic modulators achieved by controlling chromophore shape," Science 288, 119-122 (2000).

10. Y. Enami, C. T. Derose, D. Mathine, C. Loychik, C. Greenlee, R. A. Norwood, R. D. Kim, J. Luo, Y. Tian, A. K. Y. Jen and N. Peyghambarian, "Hybrid polymer/sol-gel waveguide modulators with exceptionally large electro-optic coefficients," Nature Photon. 6, 180-185 (2007).

11. M. Hochberg, T. Baehr-Jones, G. Wang, J. Huang, P. Sullivan, L. Dalton, and A. Scherer, "Towards a millivolt optical modulator with nano-slot waveguides," Opt. Express 15, 8401-8410 (2007)

12. Xuezhe Zheng, Jon Lexau, Ying Luo, Hiren Thacker, Thierry Pinguet, Attila Mekis, Guoliang Li, Jing Shi, Philip Amberg, Nathaniel Pinckney, Kannan Raj, Ron Ho, John E. Cunningham, and Ashok V. Krishnamoorthy, "Ultra-low-energy all-CMOS modulator integrated with driver," Opt. Express 18, 3059-3070 (2010)

13. A.Liu, et al, "A highspeed silicon optical modulator based on a metal-oxide-semiconductor capacitor," Nature 427, 615-618 (2004).

14. L. Zhou and A. W. Poon, "Silicon electro-optic modulators using p-i-n diodes embedded 10-micron-diameter microdisk resonators," Opt. Express 14, 6851-6857 (2006)

15. S. Manipatruni, Q. Xu, B. Schmidt, J. Shakya, and M. Lipson. High speed carrier injection 18 Gb/s silicon micro-ring electro-optic modulator. In Proc. of the IEEE Lasers and Electro-Optics Society, pages 537--538, Lake Buena Vista, FL, October 2007.

16. William M. Green, Michael J. Rooks, Lidija Sekaric, and Yurii A. Vlasov, "Ultra-compact, low RF power, 10 Gb/s silicon Mach-Zehnder modulator," Opt. Express 15, 17106-17113 (2007)

17. S. J. Spector, et al, "CMOS-compatible dual-output silicon modulator for analog signal processing," Opt. Express 16, 11027-11031 (2008)

18. G. Gunn, "CMOS photonicsTM - SOI learns a new trick," in Proceedings of IEEE International SOI Conference Institute of Electrical and Electronics Engineers, New York, (2005), 7-13.

19. A. Liu, et al, "High-speed optical modulation based on carrier depletion in a silicon waveguide," Opt. Express 15, 660-668 (2007)

20. Watts, M.R.; Trotter, D.C.; Young, R.W.; Lentine, A.L., "Ultralow power silicon microdisk modulators and switches," Group IV Photonics, 2008 5th IEEE International Conference on , vol., no., pp.4-6, 17-19 Sept. 2008

21. M. S. Nawrocka, T. Liu, X. Wang, and R. R. Panepucci, "Tunable silicon microring resonator with wide free spectral range", Appl. Phys. Lett. 89, 071110 (2006)

22. Lifetime Factors in Silicon, edited by R. D. Westbrook (American Society for Testing and Materials, Philadelphia, PA, 1980).

23. S. Manipatruni, Q. Xu, and Michal Lipson, "PINIP based high-speed high-extinction ratio micron-size silicon electrooptic modulator," Opt. Express 15, 13035-13042 (2007).

24. R. Soref, B. Bennett, "Electrooptical effects in silicon," IEEE J. Quantum Electron., 23, 123- 129 (1987)

25. N. M. Wright, D. J. Thomson, K. L. Litvinenko, W. R. Headley, A. J. Smith, A. P. Knights, J. H. B. Deane, F. Y. Gardes, G. Z. Mashanovich, R. Gwilliam, and G. T. Reed, "Free carrier lifetime modification for silicon waveguide based devices," Opt. Express 16, 19779-19784 (2008)

26. http://www.itrs.net/links/2005itrs/Linked%20Files/2005Files/SystemDrivers%20and%20Design/FO4Writeup.pdf

27. http://www.itrs.net/Links/2009ITRS/2009Chapters_2009Tables/2009Tables_FOCUS_C_ITRS.xls

Chapter 5

1000 GBIT.KM/S TRANSMISSION USING SILICON MICRORING MODULATORS:

Scaling the length of the interconnects

Abstract: We report error free data transmission at 12.5 Gbit/s over 80 km distance using silicon micro-ring modulators. We present the resulting power penalties for varying propagation distances, induced chromatic dispersions, and bandwidth-distance products. These results may enable silicon photonic interconnects for next-generation high-performance chip multi-processors, datacom and telecom optical transmission.

5.1 Introduction

Silicon photonics is emerging as solution for bandwidth and energy challenges of future interconnect applications [1-7]. Compatibility with existing CMOS fabrication processes [1, 3, 8, 9], possibility for large scale photonic-electronic integration [1, 3], ultra small foot-prints [10-12] and low power consumption [9-12] can make silicon photonics the platform of choice for high performance computing, datacom and multimedia applications. Recently, several high performance silicon photonic interconnect devices such as modulators [9-19], switches [11, 20-22], and Ge integrated photo-detectors [1, 23-32] have been demonstrated. However, the functionalities of silicon photonics for medium and long-haul optical communications remain largely unexplored [33-35]. Hence, it is of great interest to study the suitability of silicon photonic components for medium and long-haul optical communications.

In this work, to the best of our knowledge, we present the first experimental demonstration of error free, long-haul (80 km) transmission using high speed (12.5 Gbit/s) silicon micro-ring modulator (6 μm radius) with a bandwidth X distance product of 1000 Gbit.km/s. We show 1 dB dispersion power penalty at 600 Gbit.km/s comparable to telecom class modulators. We also measure the bit error rates and present the resulting power penalties for varying propagation distances, induced chromatic dispersions, and bandwidth-distance products.

We also compare the performance of the micro-ring modulators with state-of-the-art commercial modulators. Towards this goal, we demonstrate, for the first time to our knowledge, error-free operation of a silicon micro-ring resonator electro-optic modulator for modulation rates up to 12.5 Gb/s, and draw a comparison of this device with a commercial lithium Niobate ($LiNbO_3$) Mach-Zehnder electro-optic modulator. Since, all silicon photonic network-on-chip architectures proposed to date have employed silicon micro-ring resonator modulators [1, 3-7]; these measurements may enable more accurate physical layer models for optically connected high performance computers [36, 37].

5.2 Bit Error Rate Performance of Silicon Micro-ring Modulators

We fabricated a silicon micro-ring modulator formed by a high quality silicon micro-ring surrounded by a PIN carrier injection device [14]. The device comprises a micro-ring resonator with a 12-μm diameter coupled to a straight waveguide, which has input and output ports (Figure. 1d). The waveguides are 450-nm wide and 260-nm tall. The waveguide of the micro-

ring has a 50-nm slab that is doped to form the PIN diode structure, with nickel silicide for the electrical contacts. The silicon micro-ring resonator electro-optic modulator discussed here was fabricated using electron-beam lithography and reactive-ion etching. For details of the exact fabrication process used please see [38]. The non-return-to-zero (NRZ) on-off-keyed (OOK) modulation signal is encoded onto a wavelength channel by an incoming continuous wave (CW) source passing in and out of resonance of the micro-ring resonator. This resonance shift is caused by the plasma-dispersion effect from injecting and extracting electrical carriers through the PIN diode. To achieve high modulation rates that are typically limited by carrier lifetimes, the modulator is driven using a pre-emphasis method [1, 14].

We first evaluate the silicon microring modulator at varying modulation rates by examining the output modulation temporal response (Figure. 5.2a–d). The experimental setup is depicted in Figure. 5.1a and described in the Methods section. This is accomplished by setting the clock rate to 5, 7.5, 10, and 12.5 GHz, electrically driving the microring modulator with 5-, 7.5-, 10-, and 12.5-Gb/s Non Return to Zero (NRZ) data. The electro-optic response of the microring modulator then encodes the incoming light with the electrical data. Once that data signal leaves the chip, the eye diagrams of the optical signals are measured (Figure. 5.2a–d). The resulting eye diagrams show clear openings, and degrade as we drive the modulator at higher modulation rates, resulting from electrical carrier lifetime limitations and transient response of the micro-ring resonator and the closing of the temporal window. The pre-emphasis circuit to enable carrier injection and extraction has been optimized for each modulation rate.

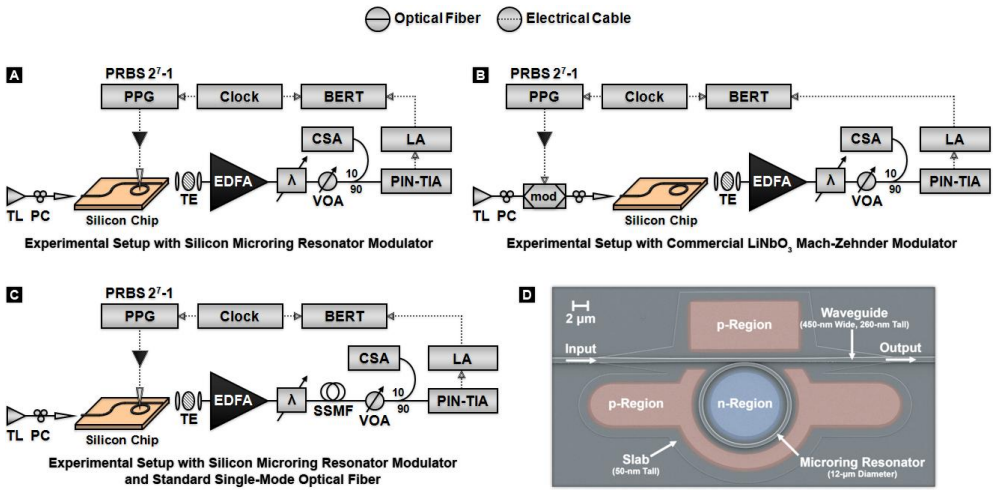

Figure 5.1 Experimental setup diagrams using the silicon microring resonator electro-optic modulator and commercial LiNbO3 Mach-Zehnder electro-optic modulator. a, Text. b, Text. c, Text. d, Top-view scanning-electron-microscope (SEM) image of the microring modulator.

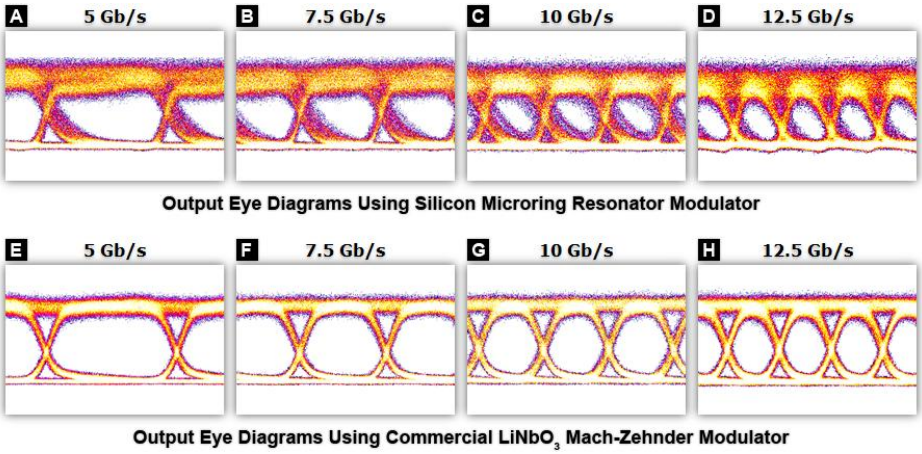

Figure 5.2 | Experimentally-measured temporal responses of varying modulation rates for the silicon microring resonator electro-optic modulator and commercial LiNbO3 Mach-Zehnder electro-optic modulator. Output eye diagrams for the a, 5-Gb/s; b, 7.5-Gb/s; c, 10-Gb/s; and d, 12.5-Gb/s modulation rate using the microring modulator, and e, 5-Gb/s; f, 7.5-Gb/s; g, 10-Gb/s; and h, 12.5-Gb/s modulation rate using the Mach-Zehnder modulator.

For each modulation rate configuration of the silicon microring modulator, we perform bit-error-rate (BER) measurements of the resulting optical data signal leaving the chip (Figure. 5.3a). We first observe error-free operation (defined as having BERs less than 10-12) for each modulation rate. Subsequently, BER curves are recorded for the 5-, 7.5-, 10-, and 12.5-Gb/s modulation rates. The experimentally-measured BER curves confirm the signal integrity degradation as the modulation rate is increased.

5.3 BER Performance Comparison with State of The Art LiNbO3 Mach-Zehnder Modulator

We compare the performance of the micro-ring modulator with a commercial $LiNbO_3$ Mach-Zehnder modulator at varying modulation rates (Figure. 5.2e–h). The experimental setup is depicted in Figure. 5.1b and described in the Methods section. This is accomplished by setting the clock rate to 5, 7.5, 10, and 12.5 GHz, electrically driving the Mach-Zehnder modulator with 5-, 7.5-, 10-, and 12.5-Gb/s data. The electro-optic response of the Mach-Zehnder modulator then encodes the incoming light with the same data. The optical data signal is then inserted into the silicon chip, bypassing the microring resonator. Once the data signal leaves the silicon chip, the eye diagrams of the optical signal are evaluated (Figure. 5.2e–h). The resulting eye diagrams show clear openings, and degrade as we drive the modulator at higher modulation rates, resulting mostly from the closing of the temporal window. The modulation bias is optimized for each configuration. For each modulation rate configuration of the $LiNbO_3$ Mach-Zehnder modulator, we perform bit-error-rate (BER) measurements of the resulting optical data signal leaving the silicon chip (Figure. 5.3a). We

observe error-free operation (defined as having BERs less than 10^{-12}) for each modulation rate, and subsequently record BER curves for the 5-, 7.5-, 10-, and 12.5-Gb/s modulation rates. Again, the experimentally-measured BER curves confirm the signal integrity degradation as the modulation rate is increased.

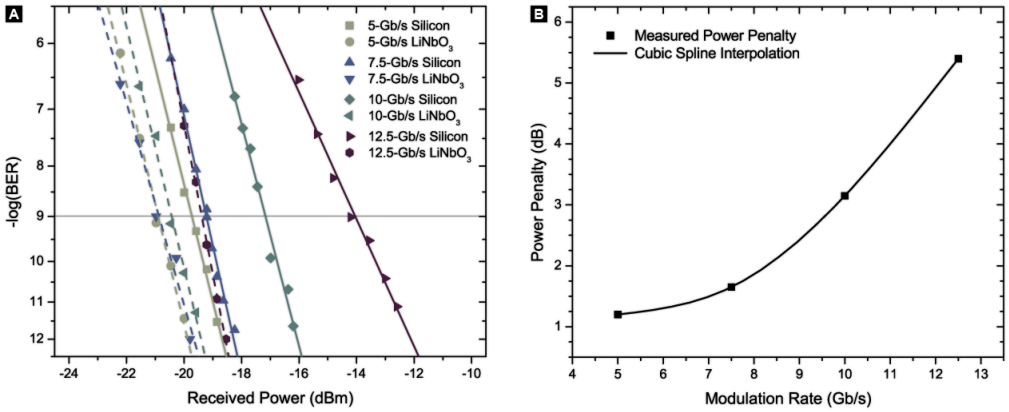

Figure 5.3 | Experimentally-measured BER curves for up to 12.5-Gb/s modulation rate using silicon microring resonator electro-optic modulator and commercial LiNbO3 Mach-Zehnder electro-optic modulator. a, BER curves for 5-, 7.5-, 10-, and 12.5-Gb/s modulation rates using both the microring modulator and Mach-Zehnder modulator. b, Resulting power penalty associated with operation of the microring.

To draw a system-level functional comparison between the two modulators, the BER curves measured for the $LiNbO_3$ Mach-Zehnder modulator are set as the back-to-back cases for the BER curves measured for the silicon microring modulator. The resulting power penalties of the operation of the microring modulator compared to the Mach-Zehnder modulator are 1.2, 1.65, 3.15, and 5.4 dB for 5-, 7.5-, 10-, and 12.5-Gb/s modulation rates, respectively (Figure. 5.3b). Much of these power penalties may be improved with more optimal pre-emphasis configurations for each

modulation rate.

5.4 Long Haul Data Transmission using Silicon Micro-ring Modulators

We study the signal integrity degradation induced by dispersion effects in varying propagation lengths of SSMF, resulting from the induced chirp in the microring modulator. The experimental setup is depicted in Figure. 5.1c and described in the Methods section. We first transmit a 10-Gb/s modulated signal through SSMF lengths of 0, 1, 2, 5, 10, 15, 40, 60, and 80 km, inducing proportional amounts of chromatic dispersion. The eye diagrams of the resulting optical signals are evaluated for each configuration (Figure. 5.4a–i). The eye diagrams show clear openings, and remain relatively unchanged for optical fiber lengths of up to 15 km (Figure. 5.4a–f). The eye diagrams subsequently begin to lose temporal window and display increased noise after 40-km propagation distances, as dispersion effects become more distinct (Figure. 5.4g), displaying noticeable degradation at 60 and 80 km (Figure. 5.4h,i). To evaluate this dependence of the signal integrity degradation on modulation rate, the silicon modulator is subsequently evaluated at a 12.5-Gb/s modulation rate for the 0- and 80-km optical fiber lengths (Figure. 5.4j,k). After this 80-km transmission, the eye diagram of the resulting optical signal is evaluated (Figure. 5.4k). Once again, the eye diagram shows noticeable degradation from the induced chromatic dispersion.

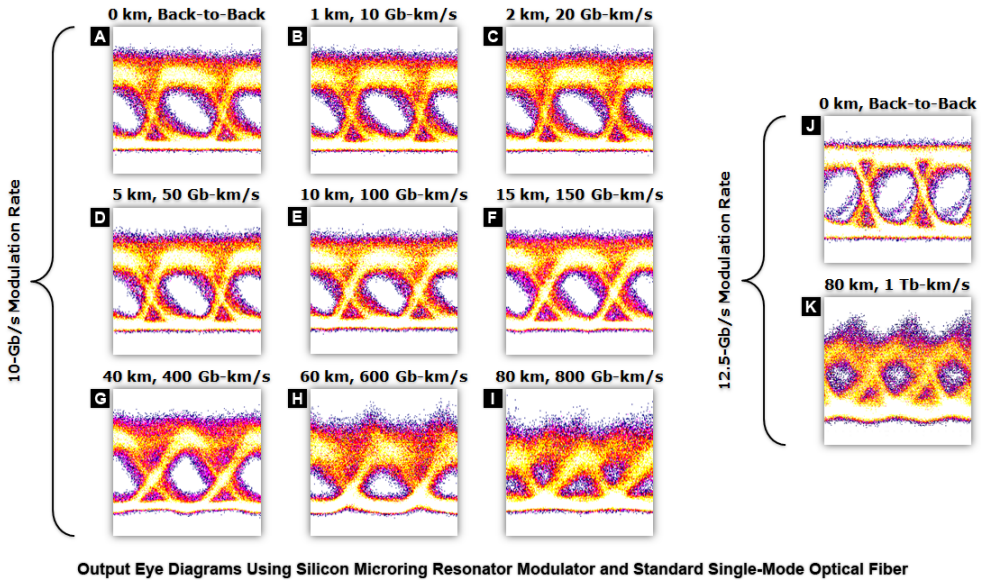

Figure 5.4 | Experimentally-measured temporal responses of varying propagation lengths through SSMF using the silicon microring resonator electro-optic modulator. Output eye diagrams for the a, 0-km; b, 1-km; c, 2-km; and d, 5-km; e, 10-km; f, 15-km; g, 40-km; h, 60-km; and i, 80-km propagation lengths for 10-Gb/s modulation rate using the microring resonator, and j, 0-km; and k, 80-km propagation lengths for 12.5-Gb/s modulation rate using the microring resonator.

We quantify the chromatic dispersion effects due to long distance propagation using BER measurements at varying propagation distances over a SSMF fiber. We perform BER measurements at the 10-Gb/s modulation rate for each propagation distance configuration (Figure. 5.5a). For each configuration, error-free operation is initially observed. BER curves are then recorded for the 0-, 1-, 2-, 5-, 10-, 15-, 40-, 60-, and 80-km propagation distances (Figure. 5.5a). Setting the configuration bypassing the SSMF as the back-to-back case, the measured power penalty is recorded for each propagation length (Figure. 5.5b). Compared to the 0-km propagation distance, the measured power penalties remains constant at 0 dB for all propagation distances up to 40 km, and are 0.6- and 2.5-dB for propagation

distances of 60 and 80 km, respectively (Figure. 5.5b). Using the chromatic dispersion for a given propagation length characteristic of the SSMF employed in these measurements, which is about 17 ps/(nm-km) at the 1565-nm operating wavelength, the measured power penalties remain constant at 0 dB for all induced chromatic dispersions up to 680 ps/nm, and are 0.6 and 2.5 dB for induced chromatic dispersions of 1020 and 1360 ps/nm, respectively. We then record BER curves at the 12.5-Gb/s modulation rate for the 0- and 80-km propagation distances (Figure. 5.3a). Once again, setting the configuration bypassing the SSMF as the back-to-back case produces a 2.5-dB power penalty.

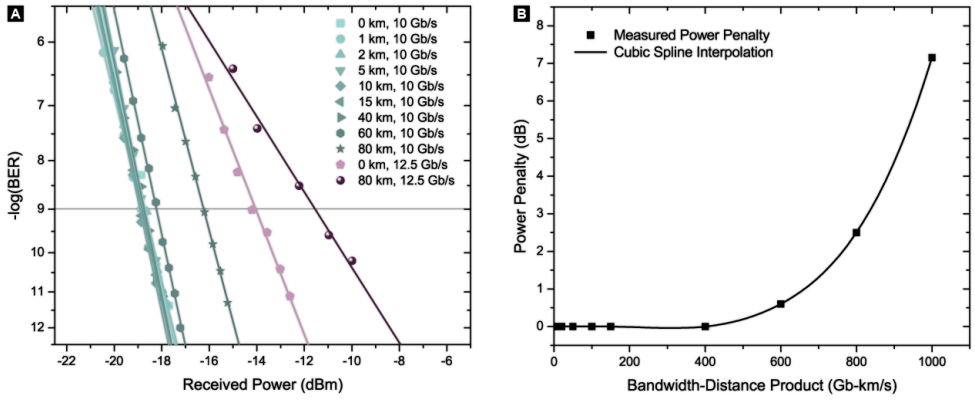

Figure 5.5 | Experimentally-measured BER curves of varying propagation lengths through SSMF for up to 12.5-Gb/s modulation rate using silicon microring resonator electro-optic modulator. a, BER curves for 0-, 1-, 2-, 5-, 10-, 15-, 40-, 60-, and 80-km propagation lengths for 10-Gb/s modulation rate, and 0- and 80-km propagation lengths for 12.5-Gb/s modulation rate, using the microring modulator. b, Resulting power penalty for the varying propagation lengths.

The measured power penalty for each bandwidth-distance product configuration is then determined, producing power penalties that, for the 10-Gb/s modulation rate, remain constant at 0 dB for all bandwidth-distance

products up to 400 Gb-km/s, and are 0.6 and 2.5 dB for bandwidth-distance products of 600 and 800 Gb-km/s, respectively. For the 12.5-Gb/s modulations rate, the data signal incurs a 2.5-dB power penalty for the 1 Tb-km/s bandwidth-distance product.

5.5 Conclusion

In conclusion, we demonstrate error-free transmission of silicon micro-ring modulated signals with a bandwidth distance capacity of 1Tbit.km/s (propagation distances up to 80 km at 12.5 Gbit/s). We show 1 dB dispersion power penalty for 10 Gbit/s signals propagating over 60 km in a standard SMF fiber. We also report the resulting power penalties for varying propagation distances, induced chromatic dispersions, and bandwidth-distance products. The demonstrated performance of this silicon modulator can enable longhaul and datacom range optical interconnects using silicon photonics [33].

We also benchmarked the error rates of silicon microring modulators with a commercial LiNbO3 Mach-Zehnder electro-optic modulator. Quantifiable performance metrics extracted from silicon photonic devices aid in determining the functionality that these devices perform in large-scale chip-chip as well as on chip photonic network architectures [36, 37]. As system level demonstrations mature in silicon photonics [3], the results presented here may enhance the design of short range photonic networks using accurate physical layer models [37].

5.6 Methods

The experimental setup for the silicon microring modulator (Figure. 5.1a) involves a tunable laser (TL) source generating a CW 1565-nm lightwave that is coupled on chip using a tapered fiber. The lightwave is then modulated on chip by the microring resonator, driven by a pulse pattern generator (PPG) generating a 2^7-1 pseudo-random bit sequence (PRBS), followed by a pre-emphasis circuit. Off chip, the signal passes through an erbium-doped fiber amplifier (EDFA), a tunable grating filter (λ), and a variable optical attenuator (VOA). The signal is received by a high-speed PIN photodiode and transimpedance amplifier (PIN-TIA) receiver followed by a limiting amplifier (LA), and is evaluated using a BER tester (BERT). Both the PPG and BERT are synchronized to the same clock. Using a power tap, a communications signal analyzer (CSA) is used to examine the temporal response of the signal before the receiver. Polarization controllers (PCs) are used throughout the setup.

The experimental setup for the $LiNbO_3$ Mach-Zehnder electro-optic modulator is similar to the aforementioned experimental setup, except the modulation occurs off chip using the Mach-Zehnder modulator, before the optical signal is coupled on chip (Figure. 5.1b). Once on chip, this modulated signal passes by the silicon microring resonator off resonance.

The experimental setup for the silicon microring modulator and SSMF utilizes the microring modulator to modulate an incoming CW light from a TL source (Figure. 5.1c). The lightwave is coupled on chip using a tapered fiber to inverse-tapered waveguide, and is subsequently modulated by the

microring resonator, which is driven by a PPG generating a 2^7-1 PRBS, followed by the pre-emphasis circuit. Once off chip, the signal passes through an erbium-doped fiber amplifier (EDFA) and a tunable grating filter (λ) before passing through varying lengths of SSMF, set to 1-, 2-, 5-, 10-, 15-, 40-, 60-, and 80-km lengths, as well as the 0-km back-to-back case bypassing the optical fiber. After leaving the optical fiber, the signal travels through a VOA, is received by a high-speed PIN-TIA receiver followed by a LA, and is evaluated using a BERT. Both the PPG and BERT are synchronized to the same clock, which is set to either 10 or 12.5 GHz. Using a power tap, a CSA is used to examine the temporal response of the signal before the receiver. PCs are used throughout the setup. The pre-emphasis circuit is optimized for each modulation rate, and is then kept constant for the varying transmission configurations of propagation distance.

REFERENCES

1. Young, I.A.; Mohammed, E.; Liao, J.T.S.; Kern, A.M.; Palermo, S.; Block, B.A.; Reshotko, M.R.; Chang, P.L.D.; , "Optical I/O Technology for Tera-Scale Computing," Solid-State Circuits, IEEE Journal of , vol.45, no.1, pp.235-248, Jan. 2010

2. D. A. B. Miller, "Device Requirements for Optical Interconnects to Silicon Chips," Proc. IEEE 97, 1166 - 1185 (2009)

3. Krishnamoorthy, A.V.; Ron Ho; Xuezhe Zheng; Schwetman, H.; Jon Lexau; Koka, P.; GuoLiang Li; Shubin, I.; Cunningham, J.E.; , "Computer Systems Based on Silicon Photonic Interconnects," Proceedings of the IEEE , vol.97, no.7, pp.1337-1361, July 2009

4. Christopher Batten, et al. "Building Manycore Processor-to-DRAM Networks with Monolithic Silicon Photonics." IEEE Micro, 20(4):8-21, July/August 2009.

5. R. Beausoleil, et al, "A Nanophotonic Interconnect for High-Performance Many-Core Computation," in Integrated Photonics and Nanophotonics Research and Applications, (Optical Society of America, 2008), paper ITuD2

6. Shacham, K. Bergman, and L. P. Carloni, "On the Design of a Photonic Network-on-Chip," in Networks-on-Chip (2007), pp. 53-64.

7. Kirman, N.; et al, "Leveraging Optical Technology in Future Bus-based Chip Multiprocessors," Microarchitecture, 2006. MICRO-39. 39th Annual IEEE/ACM International Symposium on , vol., no., pp.492-503, 9-13 Dec. 2006

8. A. Narasimha, et al "A 40-Gb/s QSFP optoelectronic transceiver in a 0.13 _m CMOS silicon-on-insulator technology," in Optical Fiber Communication/National Fiber Optic Engineers Conf., Feb. 24–28, 2008, pp. 1–3.

9. X. Zheng, J. Lexau, Y. Luo, H. Thacker, T. Pinguet, A. Mekis, G. Li, J. Shi, P. Amberg, N. Pinckney, K. Raj, R. Ho, J.E. Cunningham, and A.V.

Krishnamoorthy, "Ultra-low-energy all-CMOS modulator integrated with driver," Opt. Express 18, 3059-3070 (2010)

10. B. Schmidt, Q. Xu, J. Shakya, S. Manipatruni, and M. Lipson, "Compact electro-optic modulator on silicon-on-insulator substrates using cavities with ultra-small modal volumes," Opt. Express 15, 3140-3148 (2007)

11. Watts, M.R.; Trotter, D.C.; Young, R.W.; Lentine, A.L., "Ultra low power silicon microdisk modulators and switches," Group IV Photonics, 2008 5th IEEE International Conference on , vol., no., pp.4-6, 17-19 Sept. 2008

12. S. Manipatruni, L. Chen, K. Preston, and M. Lipson, "Ultra Low Power Electro-Optic Modulator on Silicon: Towards Direct Logic Driven Silicon Modulators," in Conference on Lasers and Electro-Optics/International Quantum Electronics Conference, OSA Technical Digest (CD) (Optical Society of America, 2010), paper CThJ6.

13. L. Liao, A. Liu, D. Rubin, J. Basak, Y. Chetrit, H. Nguyen, R. Cohen, N. Izhaky, and M. Paniccia, "40 Gbit/s silicon optical modulator for highspeed applications," Electron. Lett. 431196-1197 (2007).

14. S. Manipatruni, Q. Xu, B. Schmidt, J. Shakya, and M. Lipson, "High Speed Carrier Injection 18 Gb/s Silicon Micro-ring Electro-optic Modulator," LEOS 2007, IEEE LEOS 2007 Annu. Meeting, Paper WO2, 537-538 (2007).

15. L. Zhou and A. W. Poon, "Silicon electro-optic modulators using p-i-n diodes embedded 10-micron-diameter microdisk resonators," Opt. Express 14, 6851-6857 (2006)

16. G. Gunn, "CMOS photonicsTM - SOI learns a new trick," in Proceedings of IEEE International SOI Conference Institute of Electrical and Electronics Engineers, New York, (2005), 7-13.

17. P. Dong, S. Liao, D. Feng, H. Liang, D. Zheng, R. Shafiiha, C.-C. Kung, W. Qian, G. Li, X. Zheng, A. V. Krishnamoorthy, and M. Asghari,

"Low Vpp, ultralow-energy, compact, high-speed silicon electro-optic modulator," Opt. Express 17(25), 22484–22490 (2009).

18. J. Zhang, T.-Yang Liow, G.-Qiang Lo, and Dim-Lee Kwong, "10 Gbps monolithic silicon FTTH transceiver without laser diode for a new PON configuration," Opt. Express 18, 5135-5141 (2010)

19. Y. Goebuchi, T. Ka, and Y. Kokubun, "Fast and Stable Wavelength-Selective Switch Using Double-Series Coupled Dielectric Microring Resonator," IEEE Photon. Technol. Lett. 18(3), 538–540 (2006).

20. M.A. Popović, T. Barwicz, F. Gan, M.S. Dahlem, C.W. Holzwarth, P.T. Rakich, H.I. Smith, E.P. Ippen and F.X. Kärtner, "Transparent wavelength switching of resonant filters," presented at Conference on Lasers and Electro-Optics (CLEO), Baltimore, MD, May 10, 2007, postdeadline paper CPDA2

21. Hugo L. R. Lira, Sasikanth Manipatruni, and Michal Lipson, "Broadband hitless silicon electro-optic switch for on-chip optical networks," Opt. Express 17, 22271-22280 (2009)

22. "Low-power, 2×2 silicon electro-optic switch with 110-nm bandwidth for broadband reconfigurable optical networks," J. Van Campenhout, W. M. J. Green, S. Assefa, and Y. A. Vlasov, Optics Express 17(26), 24020-24029, 2009

23. G. Dehlinger, S. J. Koester, J. D. Schaub, J. O. Chu, Q. C. Ouyang, and A. Grill, "High-speed Germanium-on-SOI lateral PIN photodiodes," IEEE Photon. Technol. Lett. 16, 2547-2549 (2004)

24. M. Jutzi, M. Berroth, G. Wöhl, M. Oehme, and E. Kasper, "Ge-on-Si vertical incidence photodiodes with 39-GHz bandwidth," IEEE Photon. Technol. Lett. 17, 1510-1512 (2005)

25. J. Liu, D. D. Cannon, K. Wada, Y. Ishikawa, S. Jongthammanurak, D. Danielson, J. Michel, and L. C. Kimerling, "Tensile strained Ge p-i-n photodetectors on Si platform for C and L band telecommunications," Appl. Phys. Lett. 87, 011110-1-3 (2005).

26. M. Rouvière, M. Halbwax, J-L. Cercus, E. Cassan, L. Vivien, D. Pascal, M. Heitzmann, J-M. Hartmann, and S. Laval, "Integration of germanium waveguide photodetectors for intrachip optical interconnects," Opt. Eng. 44, 75402-75406 (2005)

27. L. Colace, G. Masini A. Altieri, and G. Assanto, "Waveguide photodetectors for the near-infrared in polycrystalline germanium on silicon," IEEE Photon. Technol. Lett. 18, 1094-1096 (2006).

28. D. Ahn, C. Hong, J. Liu, W. Giziewicz, M. Beals, L. C. Kimerling, J. Michel, J. Chen, and F. X. Kärtner, "High performance, waveguide integrated Ge photodetectors," Opt. Express 15, 3916-3921 (2007).

29. L. Vivien, M. Rouvière, J. Fédéli, D. Marris-Morini, J. Damlencourt, J. Mangeney, P. Crozat, L. Melhaoui, E. Cassan, X. Roux, D. Pascal, and S. Laval, "High speed and high responsivity germanium photodetector integrated in a Silicon-On-Insulator microwaveguide," Opt. Express 15, 9843-9848 (2007).

30. T. Yin, R. Cohen, M. Morse1, G. Sarid, Y. Chetrit, D. Rubin, and Mario J. Paniccia, "31GHz Ge n-i-p waveguide photodetectors on Silicon-on-Insulator substrate," Opt. Express 15, 13965-13971 (2007).

31. Long Chen, Po Dong, and Michal Lipson, "High performance germanium photodetectors integrated on submicron silicon waveguides by low temperature wafer bonding," Opt. Express 16, 11513-11518 (2008)

32. "CMOS-integrated Germanium Photodetector with Ultra-low Capacitance", S. Assefa, F. Xia, S. Bedell, Y. Zhang, T. Topuria, P. M. Rice, and Y. Vlasov Optics Express 18(5), 4986-4999, 2010

33. Lin Zhang; Yunchu Li; Jeng-Yuan Yang; Muping Song; Beausoleil, R.G.; Willner, A.E.; , "Silicon-Based Microring Resonator Modulators for Intensity Modulation," Selected Topics in Quantum Electronics, IEEE Journal of , vol.16, no.1, pp.149-158, Jan.-feb. 2010

34. Biberman, N. Ophir, K. Bergman, S. Manipatruni, L. Chen, and M. Lipson, "First Demonstration of 80-km Long-Haul Transmission of 12.5-Gb/s Data Using Silicon Microring Resonator Electro-Optic Modulator,"

inOptical Fiber Communication Conference, OSA Technical Digest (CD) (Optical Society of America, 2010), paper JWA28.

35. W. A. Zortman, A. L. Lentine, M. R. Watts, and D. Trotter, "Power Penalty Measurement and Frequency Chirp Extraction in Silicon Microdisk Resonator Modulators," in Optical Fiber Communication Conference, OSA Technical Digest (CD) (Optical Society of America, 2010), paper OMI7.

36. Scott Beamer, Chen Sun, Yong-Jin Kwon, Ajay Joshi, Christopher Batten, Vladimir Stojanovic, and Krste Asanovic. "Re-Architecting DRAM Memory Systems with Monolithically Integrated Silicon Photonics." International Symposium on Computer Architecture (ISCA-37), June 2010.

37. J. Chan, G. Hendry, A. Biberman, and K. Bergman, "Architectural Exploration of Chip-Scale Photonic Interconnection Network Designs Using Physical-Layer Analysis," Journal of Lightwave Technology (2010).

38. S. Manipatruni, L. Chen, and M. Lipson, "50 Gbit/s wavelength division multiplexing using silicon microring modulators," in Proceedings of 6th IEEE International Conference on Group IV Photonics (IEEE 2009), pp. 244–246.

Chapter 6
WIDE TEMPERATURE RANGE OPERATION OF SILICON MICRORING MODULATORS:
Scaling the operating range

Abstract: We demonstrate high bit rate electro-optic modulation in a resonant micron-scale silicon modulator over a temperature range of 15 K. We show that low error bit rates can be achieved by varying the bias current through the device to counteract the temperature changes. We demonstrate operation of the silicon ring over a 15 K temperature range.

6.1 Introduction

High speed electro-optic modulation in silicon is a crucial requirement for integration of silicon photonics with microelectronics. High speed Gbit/s modulators have been demonstrated recently using either resonant structures [1-3] or Mach-Zehnder interferometers [4-6]. Resonant electro-optic modulators are ideally suited for large scale optical networks on chip due to their compact size, high extinction ratio per unit length and low power consumption. However, resonant electro-optic modulators suffer from temperature sensitivity due to the relatively large thermo-optic effect in silicon [7].

In this paper, we demonstrate that the effect of thermal variations on resonant electro-optic modulators can be locally compensated by adjusting the bias current passing through the device. The bias current through the device is varied to compensate for changes in the ambient temperature

which affect the resonator. We show that modulation can be maintained over a temperature range of 15 K. Robustness in the presence of environmental conditions such as thermal variation for integrated silicon photonic devices can enable wide variety of applications in low cost CMOS systems.

The device we demonstrate is a silicon electro-optic ring modulator fabricated on a Silicon-on-Insulator (SOI) substrate. The modulator is formed by building a P-I-N junction around a ring resonator with a quality factor (Q) of 4000 and a diameter 10 μm. The schematic of the electro-optic device is shown in Figure. 6.1(a) and 1(b). The SEM picture of the resonator is shown in Figure. 6.1(c). The transmission spectrum of the ring for quasi-TM polarized light (major electric field component aligned perpendicular to the plane of silicon) is shown in Figure. 6.2 (a).

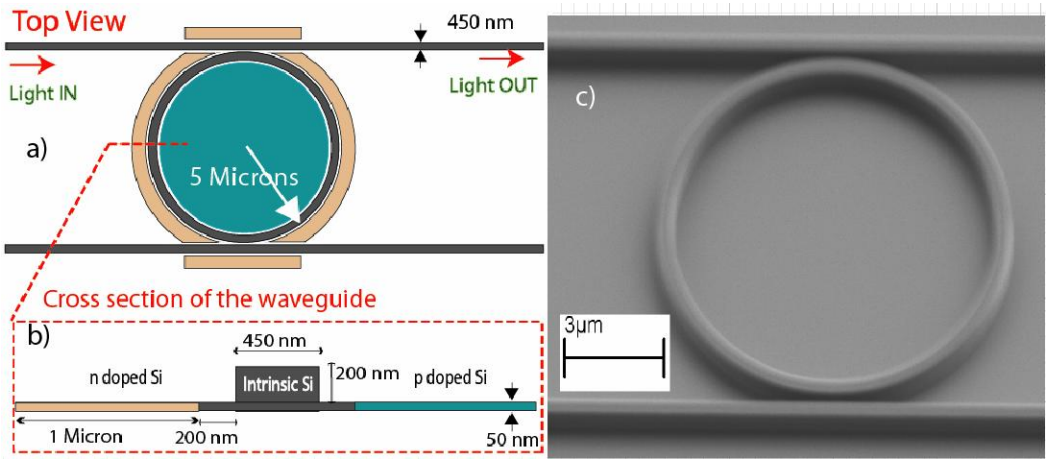

Figure. 6.1. a) Schematic of the electro-optic ring device b) Cross section of the waveguide embedded in a PIN junction c) Electron microscope image of the ring resonator before the formation of electrical device.

At constant temperature, the optical transmission through the ring is modulated using a non-return-to-zero bit sequence at 1 Gbit/s. The refractive index of the ring is modulated by active carrier injection and extraction using the PIN junction. The modulated output waveform and eye diagram at 1 Gbit/s at nominal temperature of operation (298 K) is shown in Figure. 6.2 (b). An On/Off extinction ratio of 5 dB is measured in accordance to the transmission spectral characteristics with a $\pm$ 4 V applied voltage. The high applied voltage is attributed to a large contact resistance of the device (1.7 kΩ) which can be greatly reduced by varying the implant conditions, doping profile and contact metallization [8]. The power consumption is estimated as 4.52 pJ/bit with an estimated carrier lifetime of 500 ps and injection level of $5X10^{17}$ cm^{-3} and taking into account both the switching and state holding power.

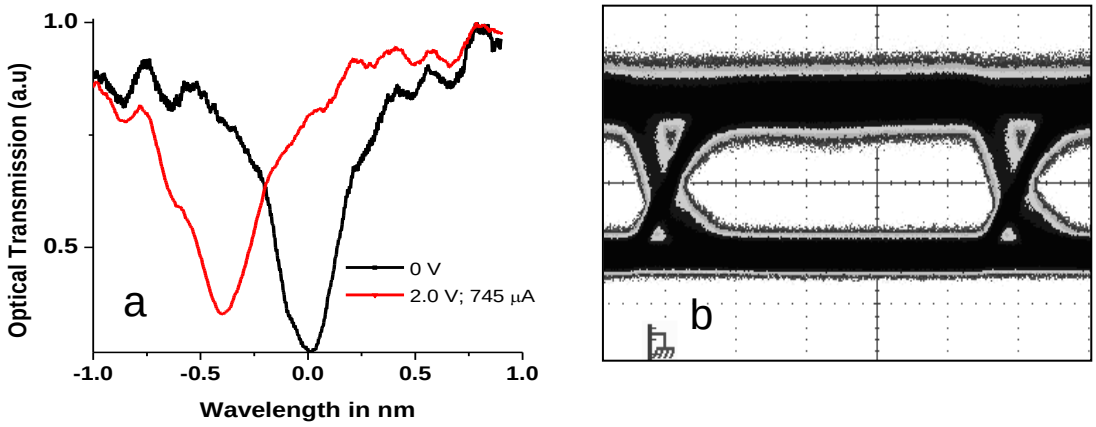

Figure. 6.2 a) Transmission spectrum of the electro-optic modulator under DC bias voltage b) Modulated waveform at 1 Gbit/s. Both measurements were performed at at nominal operating temperature (ΔT= 0 K)

6.2 Thermal effects

We analyzed the effect of temperature shift on the silicon electro-optic modulator over a temperature range of 15 K. The thermo-optic effect of silicon is given by $\Delta n/\Delta T = 1.86\times10^{-4} K^{-1}$ which leads to a resonance shift of ~0.11 nm/K from the base resonant wavelength. The sign and approximate value of the thermo-optic coefficient of silicon can be estimated using the temperature dependence of the band-gaps of silicon [9-11]. The net effective index change in the modulator results from a combination of the thermo-optic effects in both silicon and the surrounding oxide. Figure. 6.3 a shows the spectral shift as the temperature of the chip is varied over 4 K. Figure. 6.3 b shows the distorted eye diagrams under a 2 K temperature shift. We also compare the effect of thermal shift on the modulated waveforms with electro-optic computer simulations and show a good match between simulation and experiment, as shown in Figure. 6.4 (a).

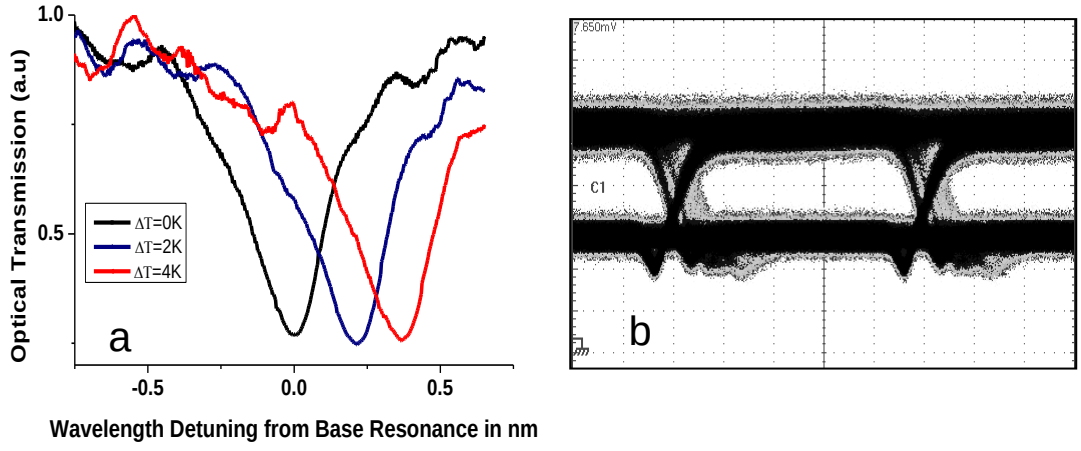

Figure. 6.3 a) Transmission spectra with temperature changes with no current through the device b) Distorted eye diagram at ΔT= 2 K., 1Gbit/s

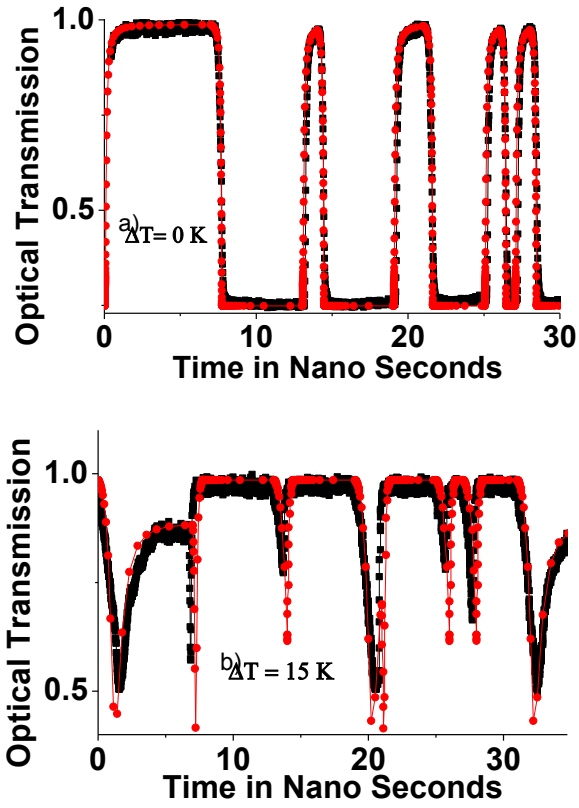

Figure. 6.4 Simulation of the waveform distortion due to thermal effects. a) Baseline simulations at ΔT= 0 K b) Distorted wave forms at ΔT= 15 K, with the red lines showing the electro-optic device computer simulations and the black lines showing the measured wave forms.

6.3 Electro-optic and thermo-optic modeling

A description of the electrical modeling is presented elsewhere [12]. The optical modeling assumes that the ring resonator is a unidirectional single mode traveling-wave cavity coupled to the waveguides with a loaded quality factor of 4000. The changes in refractive index and absorption of silicon are modeled via free carrier dispersion [13, 14]. The simulated and measured waveforms with a 15 K shift in temperature are shown in Figure. 6.4 (b).

6.4 Controlling the waveguide temperature for error free operation

In order to enable wide temperature operation of resonant silicon electro-optic modulators, we propose and implement local thermal control of the waveguide temperature by changing the bias current through the device. Using a DC bias current we first set the nominal operating condition of modulator, and as the ambient temperature varies we vary the DC bias current to maintain the local temperature of the device at the original value. As we vary the bias current of the PIN junction, the heat generated in the waveguides allows control over the local temperature of the waveguide forming the resonator. We emphasize that this method is fundamentally different from using a free-carrier electro optic phase shift associated with carrier injection to obtain wide temperature operation.

Using this control technique, we experimentally demonstrate wide temperature range, 15 K, operation of the resonant silicon electro-optic modulator. To control the DC bias current through the device, we add the high speed RF signal to a DC current source using a bias tee. A capacitor of 20 nF avoids the loading of the bit pattern generator by the DC bias supply, and an inductor of 1 mH isolates the DC source from the bit pattern. The DC bias current is varied to counter the effect of the temperature change for retrieving the bit pattern. The base operating condition was set with a 1.36 mA DC current through the device with a 0.2 V bias voltage. The current was reduced to 345 μA (with a 2.2 V bias voltage) in order to maintain the modulation when the ambient temperature was raised by 15 K. Note that the current measured by the current meter is the averaged extraction current during the reverse bias of the device. Note that even though the bias current

produces an index change due to the injected carriers in the ON state, the effect of carrier dispersion due to the bias current is absent in the OFF state. Hence, the bias current is contributing only in regulating the temperature of the waveguides. The temperature of the heat sink is controlled through an external temperature controller with feedback. The Joule thermal power consumption for maintaining the base operating condition is estimated as 3.1 pJ/bit and 0.20 pJ/bit at ΔT =15 K.

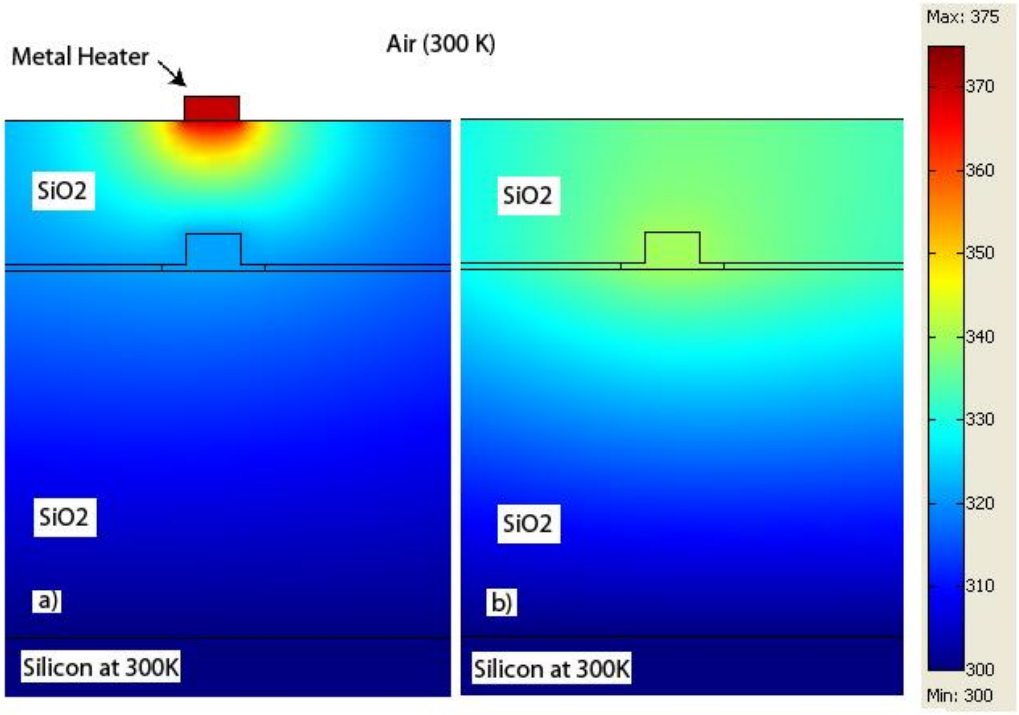

Figure 6.5 Temperature profiles using a) metal strip heater and b) direct localized waveguide heating. The color bar indicates the temperature scale in K.

We compare the power efficiency of the proposed local temperature control method with the commonly used metal strip heater method. We use two dimensional heat flow which takes into consideration conduction of

heat to the substrate and the radiative heat loss though the top surface of the chip. The thermal modeling was carried out in COMSOL. The loss through the top surface is modeled via the Stefan-Boltzman law with emissivity factors of 0.94 for SiO_2 and 0.33 for the smooth metal layer. We assumed that the bottom of the wafer is the heat sink and is maintained at 300 K (T_{amb}). We also assumed a 3 μm buried oxide layer and 1 μm top cladding oxide. The top cladding layer is chosen to be 1 μm so that the heating due to the metal layers is optimal while limiting the optical losses due to mode overlap with metal [16].

We show that the direct localized heating inside the waveguide is significantly more efficient than a metal heater on top of the device for tuning resonances. The two dimensional thermal simulations show that the temperature difference produced by direct localized heating using the PIN structure is significantly larger than metal-strip-heater method (see Figure. 6.7). We assumed a heat source of 1 $mW/\mu m^3$ localized within the metal layer of the waveguide to compare the efficiency of both methods. We also assumed that the metal heaters were perfectly aligned with the waveguides for optimal heating. We compared the temperature difference ($\Delta T = T_{local} - T_{amb}$) at the center of the waveguide produced by both methods. The direct localized heating using PIN structure produces $\Delta T = 40.1$ $K/(mW/\mu m^3)$ – Figure. 6.6 (b) - while a metal heater positioned on top produces $\Delta T = 21.3$ $K/(mW/\mu m^3)$ – Figure. 6.6 (a). Hence, the simulations show that the direct localized heating method is approximately twice as efficient as the metal heater. An added advantage of using the direct localized heating method technique is that it requires fewer fabrication steps as it makes use of the

existing structure (i.e. the contacts of the PIN device) to achieve thermal tuning.

6.5 Wide temperature range operation

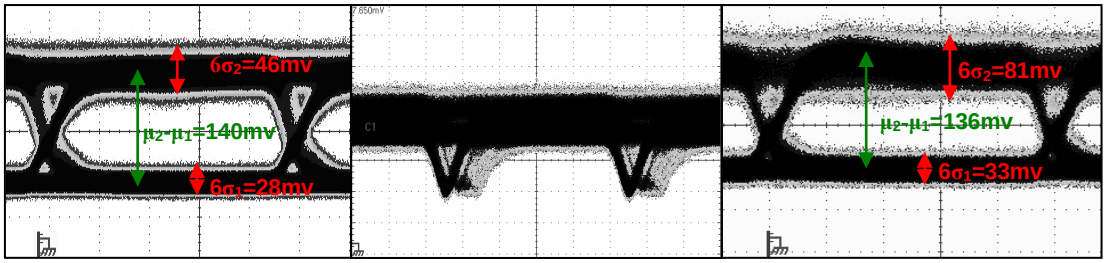

a) Eye Diagram at ΔT=0 K **b) Degraded at ΔT= 15 K** **c) Retrieved at ΔT= 15 K**

Figure. 6.6 Optical transmission eye diagrams of the electro-optic modulator at various thermal and bias current conditions (applied AC modulated voltage was kept constant)

We show open eye diagrams with clear eye opening over 15 K by controlling the DC bias current to maintain the local temperature of the ring at the original operating condition as shown in Figure. 6.6. We estimate the quality factor of the eye diagrams $Q = |\mu_2 - \mu_1| / (\sigma_2 + \sigma_1)$ to be 11.35 at the nominal operating temperature. The retrieved quality factor at ΔT= 15 K is 7.15. These Q values are sufficient for a BER of 10^{-12} [15]. A 2^{10}-1 Non-Return-to-Zero (NRZ) Pseudo Random Bit Sequence (PRBS) was used for these experiments. The predicted thermal time constants are of the order of μs (T_c). Hence the effect of the length longest sequence of ones or zeros will be significant for PRBS signals with more than (T_c /Bit period) consecutive 1s or 0s. Note that this limitation becomes less stringent as the bit rate is increased. For example, with a bit rate of 1 Gbit/s and a time constant of 1000 ns the PRBS length is limited to 100's of consecutive bits. However at 20 Gbit/s, the PRBS number can be extended to 20 times longer sequences

since the bit period is significantly lower.

6.6 Conclusion

In summary, we have shown wide temperature range operation of resonant micron scale modulators while ensuring high speed operation. We demonstrated waveform restoration over a 15 K range while maintaining a bit rate of 1 Gbit/s. In light of the recent demonstration of high extinction, high speed (> 18 Gbit/s, 10 dB) modulators [17], the wide temperature range operation of resonant compact electro-optic modulators has significant impact for the large scale integration of compact modulators for on chip optical networks.

REFERENCES

1. Q. Xu, B. Schmidt, S. Pradhan, and M. Lipson, "Micrometre-scale silicon electro-optic modulator", Nature, Vol. 435, pp. 325-327, 2005.

2. B. Schmidt, Q. Xu, J. Shakya, S. Manipatruni, and M. Lipson, "Compact electro-optic modulator on silicon-on-insulator substrates using cavities with ultra-small modal volumes", Opt. Express 15, 3140-3148 (2007).

3. L. Zhou and A. W. Poon, "Silicon electro-optic modulators using p-i-n diodes embedded 10-micron-diameter microdisk resonators," Opt. Express 14, 6851-6857 (2006).

4. A. Liu, R. Jones, L. Liao, D. Samara-Rubio, D. Rubin, O. Cohen, R. Nicolaescu and M. Paniccia, "A high-speed silicon optical modulator based on a metal-oxide-semiconductor capacitor," Nature 427, 615-618 (2004).

5. F. Gan and F. X. Kärtner, "High-Speed Electrical Modulator in High-Index-Contrast (HIC) Si-Waveguides," in Conference on Lasers and Electro-Optics, Technical Digest (CD) (Optical Society of America, 2005), paper CMG1.

6. W. M. J. Green, M. J. Rooks, L. Sekaric, and Y. A. Vlasov, "Optical modulation using anti-crossing between paired amplitude and phase resonators," Opt. Express 15, 17264-17272 (2007).

7. M. Lipson, "Compact Electro-Optic Modulators on a Silicon Chip," IEEE J. Selected Topics in Quantum Electron, 12, 1520-1526 (2006).

8. Wen Luh Yang, Tan Fu Lei, and Chung Len Lee. "Contact Resistivities of Al and Ti on Si Measured by a Self-aligned Vertical Kelvin Test Resistor Structure", Solid-State Electronics, Vol. 32, No. 1 1, pp.997-1001, 1989.

9. Y. P. Varshni, "Temperature dependence of the energy gap in semiconductors," Physica 34, 149-154 (1967).

10. T.S. Moss, "Optical Properties of Semiconductors", Butterworth (1959), p.48.

11. Francesco G. Della Corte, Maurizio Esposito Montefusco, Luigi Moretti, Ivo Rendina, and Giuseppe Cocorullo, "Temperature dependence analysis of the thermo-optic effect in silicon by single and double oscillator models", J. Appl. Phys. 88, 7115 (2000).

12. S. Manipatruni, Q. Xu, and M. Lipson, "PINIP based high-speed high-extinction ratio micron-size silicon electrooptic modulator," Opt. Express 15, 13035-13042 (2007). B. Jalali, O. Boyraz, D. Dimitropoulos, and V. Raghunathan, "Scaling laws of nonlinear silicon nanophotonics" Proc. SPIE, 5730, 41-51 (2005).

13. R. Soref, B. Bennett, "Electrooptical effects in silicon," IEEE J. Quantum Electron., 23, 123- 129 (1987)

14. H. C. Huang, S. Yee, and M. Soma, "Quantum calculations of the change of refractive index due to free carriers in silicon with non parabolic band structure," J. Appl. Phys. 67, 2033-2039 (1990).

15. Ippei Shake, Hidehiko Tikara, and Satoki Kawanishi "Simple Measurement of Eye Diagram and BER Using High-Speed Asynchronous Sampling", Journal of Lightwave Technology, vol 22, No. 5 , May 2004.

16. Gan, F.; Barwicz, T.; Popovic, M. A.; Dahlem, M. S.; Holzwarth, C. W.; Rakich, P. T.; Smith, H. I.; Ippen, E. P.; and Kartner, F. X., "Maximizing the Thermo-Optic Tuning Range of Silicon Photonic Structures," Photonics in Switching, 2007 , vol., no., pp.67-68, 19-22 Aug. 2007.

17. Manipatruni, Sasikanth; Xu, Qianfan; Schmidt, Bradley; Shakya, Jagat; and Lipson, Michal, "High Speed Carrier Injection 18 Gb/s Silicon Micro-ring Electro-optic Modulator," Lasers and Electro-Optics Society, 2007. LEOS 2007. The 20th Annual Meeting of the IEEE , vol., no., pp.537-538, 21-25 Oct. 2007

Chapter 7
TUNABLE SLOW AND FAST LIGHT ON A SILICON MICROCHIP USING MICRORINGS

Abstract: We demonstrate superluminal propagation in a silicon micro photonic device by creating an all-optical analogue to electromagnetically induced absorption in a solid state room temperature device of tens of microns dimensions allowing easy integration with high bandwidth room temperature systems. We achieve tunable negative delays up to 85 ps and effective group indices tunable between -1158 and -312.

7.1 Introduction

Controlling the speed of propagation of optical pulses is an important requirement for high performance optical information technology. In particular, superluminal propagation has been experimentally demonstrated within the causal limits of information transfer using electromagnetically induced absorption [6], gain doublet in specific material systems [7-10] coherent population oscillations [11] and bulk photonic components [12]. However, these techniques suffer fundamentally from low bandwidth [1-4] and/ or are constrained severely in temperature and operating wavelengths making their integration on-chip challenging [1-10].

7.2 Operating Principle

To demonstrate fast light on a silicon chip, we use the concept of electromagnetically induced absorption (EIA) from atomic physics, where

coherent interaction between optical fields and electronic energy states gives rise to a sharp absorption feature in a broader transmission spectrum [13]. The sharp spectral features in EIA systems are associated with negative group indices and fast light. Hence, by designing an optical device with a transmission spectrum that emulates the optical spectrum of an EIA system one can demonstrate fast light in a micro-photonic platform. We show here that such a device is realisable in a micro photonic platform.

7.3 Device Description

To demonstrate an optical analogue to EIA on a micro photonic platform, we designed and fabricated a photonic structure formed by two interacting optical resonators. Earlier works have suggested an optical analogue to EIA in coupled macro scale optical cavities [14]. The top view microscope image of the device is shown in Figure 7.1.

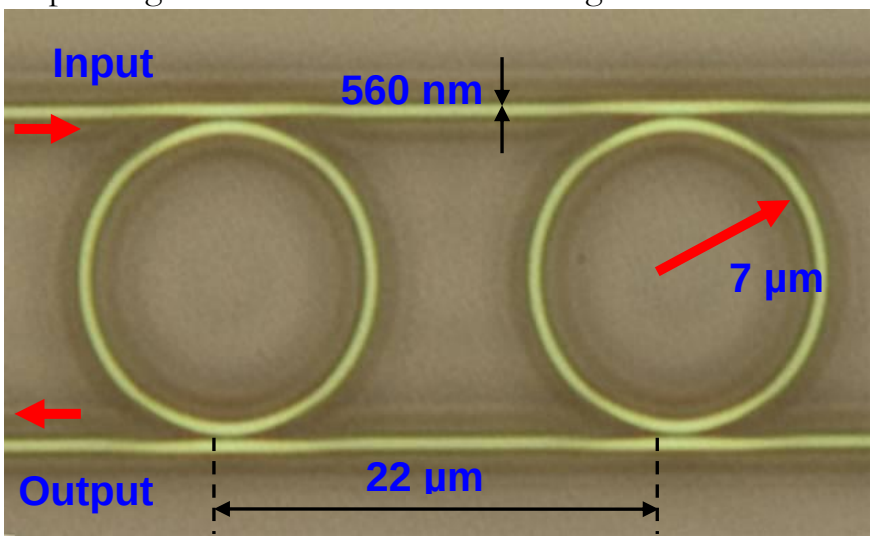

Figure 7.1: Top view microscope image of the device

The present optical device works similar to a Fabry- Perot (FP) cavity but with two salient distinctions: a) the mirrors forming the FP cavity are frequency sensitive which as we show later leads to the tunability of fast light

b) the reflection from the mirrors is routed into second waveguide which allows for the formation of a super mode. In, figure 7.2, the resonators A and B can be understood as frequency selective mirrors. Light is confined in the waveguide region between the mirrors similar to an FP cavity as shown by the mode profile. However, the device is designed such that the light rerouted to the Port A is coherently interfered with the light leaking out of the super-mode cavity producing a sharp absorption like feature (figure 7.3 a). The bandwidth of this absorption feature is determined by the bandwidth of the cavity formed by the two reflectors. Moreover, the loaded bandwidth of the spectral feature, and therefore the bandwidth in which the pulse advancement occurs can be controlled externally by tuning the reflectivity of the resonators.

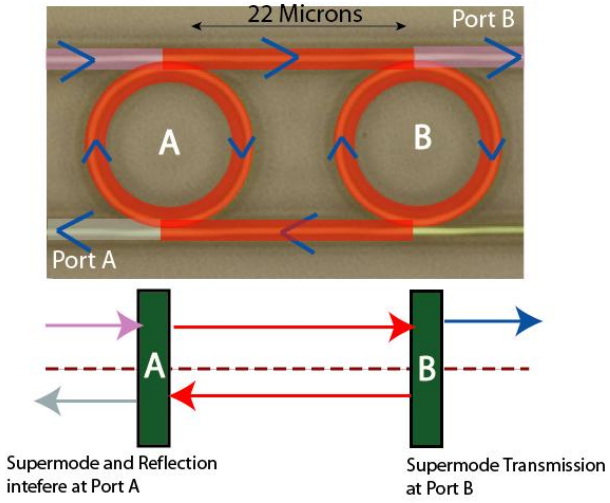

Figure 7.2: Formation of an all optical analog to electromagnetically induced absorption spectral feature line at Port A.

We fabricated the device on silicon on insulator platform. The waveguides forming the ring and the straight sections have a width of 560 nm and height of 250 nm. The rings have a radius of 7 microns. A small difference (8 nm)

in perimeter of one of the rings is used to produce a wavelength detuning between the rings. The centre-to-centre distance of the rings is 22 microns. The waveguides and rings are patterned on silicon using electron-beam lithography followed by reactive ion plasma etching. The resulting structure is clad by a 3 micron thick SiO_2 layer deposited by plasma enhanced chemical vapor deposition.

7.4 Measurement of optical delay and advance

We measured a pulse advance of 85 ps at the output port at the absorption-like spectral range (see Figure 7.3 b). The experimental setup to measure the optical advance is shown in Figure 7.4. A continuous wave light from a tunable laser source modulated at RF frequency (500 MHz) is coupled into the device. We estimate the relative group delay by comparing the probe and the output in the time domain. The time advance of the optical signal can be tuned by tuning the absorption-like spectral feature. The bandwidth can be tuned by shifting the resonance condition of one or both of the resonators. This may be accomplished through either thermal [15] or electrical [16] mechanisms. In this demonstration, we thermally tune one of the rings using an argon laser [17]. Using an optical fiber, green argon laser light (514.5 nm) in the mW power range is incident on one of the rings. As silicon absorbs the incident power, the temperature of the ring is locally modified to produce a red shift in the resonance through thermo-optic effect. As the incident argon laser intensity is increased, the absorption super-mode quality factor is modified. As shown in Figure 7.5 a, the

bandwidth of the EIA spectral feature is modified as the power of the incident laser is increased.

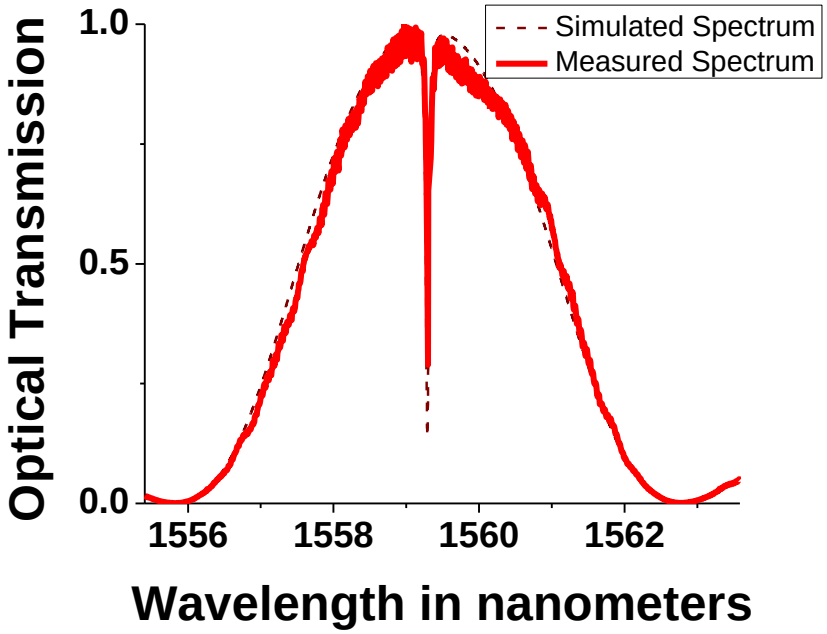

Figure 7.3. a All Optical Analog to Electromagnetically Induced Absorption: An optical analog to EIA is created when light from the super mode formed between the reflectors coherently cancels the light coupled into the port A (in Figure. 7.2). The sharpness of the spectral feature is controlled by the bandwidth of the super mode which is limited only by the intrinsic quality factor in Silicon

The measured optical pulse advance is shown in Figure 7.5 b, where the pulse advance is tuned from 85 ps to 23 ps corresponding to an effective group index range of -1158 to -312. Note that the maximum pulse advance is limited only by the maximum Q of the cavities, which in turn is limited by the fabrication process. However, the bandwidth-delay limit still applies to the system limiting the achievable fractional advance of the signals.

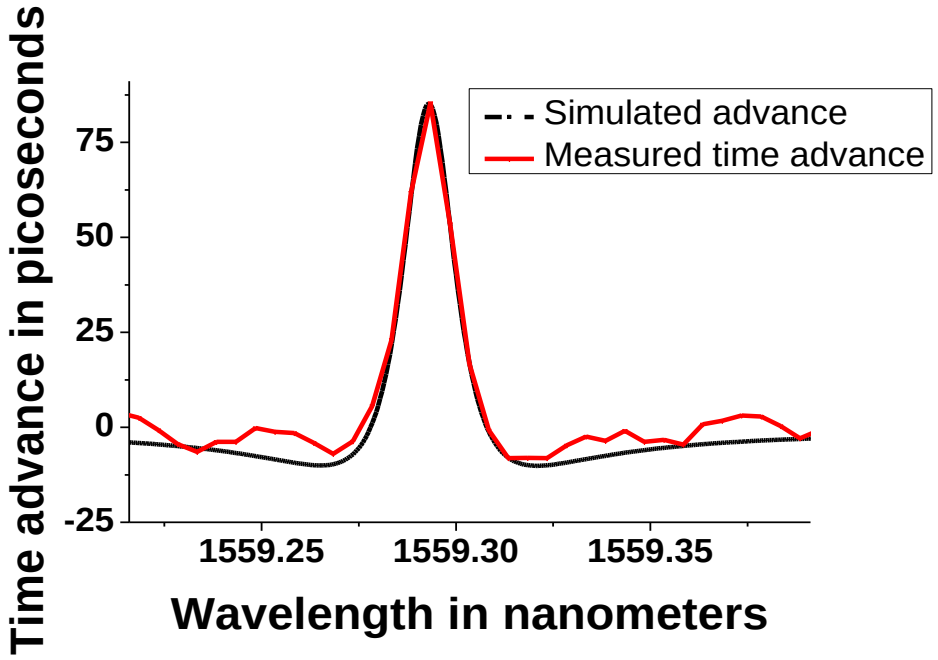

Figure 7.3 b Optical advance through the device measured at the EIA spectral feature

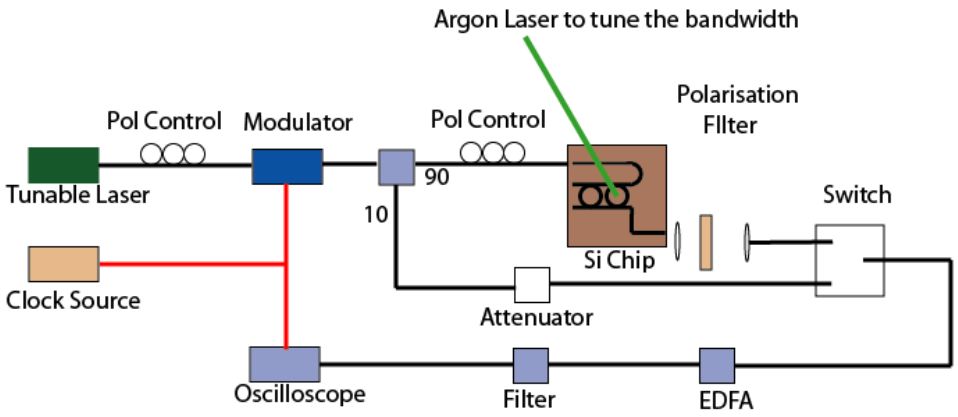

Figure. 7.4. Experimental setup. The black lines represent optical fiber and red lines represent coaxial cables for modulator RF input and oscilloscope trigger input. High speed electro optic modulator generates a sinusoidal probe beam of 500 MHz. Light is coupled to the device and compared with a reference arm to determine the delay or advance. An argon laser beam at 514.5 nm is used to thermally tune the structure to vary the bandwidth of the EIA feature.

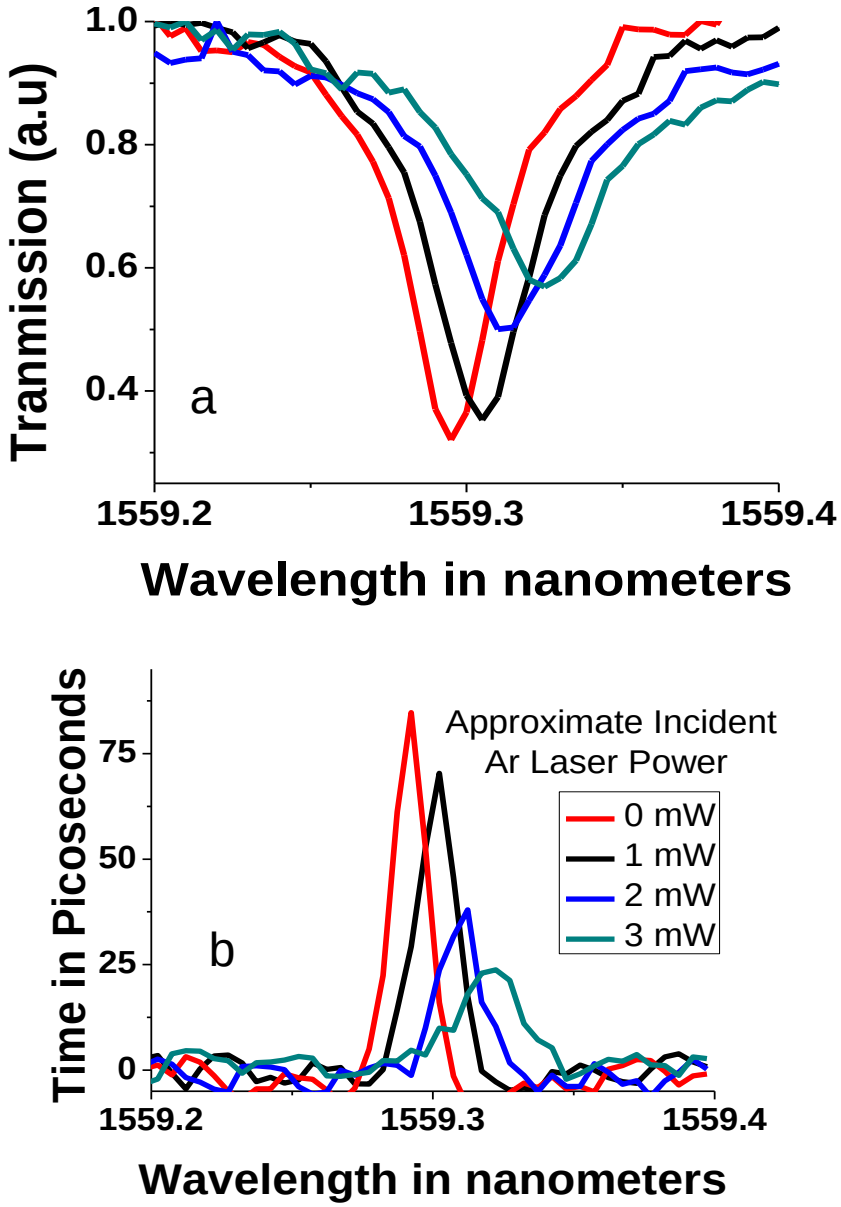

Figure. 7.5. Measured tunable optical advance through the device. The reflectivity of the mirrors is frequency sensitive and can be controlled by the tuning of one or both the reflectors. The tunable bandwidth of the spectral feature is shown in (a). The measured tunable optical pulse advance is shown in (b). The tuning of the reflectors was done here using a 514.5 nm argon laser incident on the device.

In contrast to the traditional methods, the nominal operating temperature for the above technique can span 100s of Kelvin, corresponding to 100s nm tuning range of the nominal operating wavelength. The nominal operating temperature can be designed to be between a few K to ~700 K, limited only by the thermally generated free carrier concentration. The nominal operating wavelength can be chosen to be anywhere in the 1300 nm-5500 nm region of transparency in silicon. The operating bandwidth and the maximum pulse advance can be chosen by controlling the quality factor of the optical cavity which can be designed with quality factors between 10^2 and 10^6 by controlling the losses arising from bending radius, scattering losses and surface conditions [18]. Note that even though the fractional advancement of the pulses is comparable to earlier methods, the operating bandwidth is fundamentally higher than earlier methods which are constrained by the material electronic energy states [1-9].

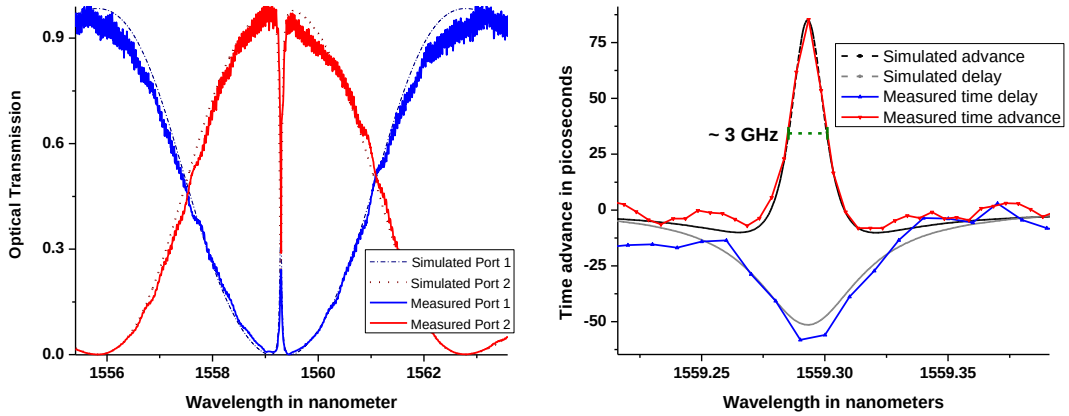

Figure. 7.6. Measured tunable delay and optical advance through the device.

In conclusion, we have shown tunable superluminal propagation on a silicon substrate using coherent interaction between optical micro-cavities.

We demonstrate generation of 85 ps time advanced signals. We also show that the negative group index can be tuned between –1158 and -312. In contrast to the earlier approaches [1-12] the proposed technique does not require gain media or specific energy levels and works at room temperature in an integrated silicon micro-scale device. The ability to advance optical pulses in a solid state highly scalable silicon micro-scale system could open up a wide array of control techniques for high performance micro optical information technology .

REFERENCES

1. A. M. Akulshin, S. Barreiro, and A. Lezama,. Steep anomalous dispersion in coherently prepared Rb vapor. Phys. Rev. Lett. **83**, 4277– 4280 (1999).

2. A. M. Steinberg, and R. Y. Chiao, Dispersionless, highly superluminal propagation in a medium with a gain doublet. Phys. Rev. A **49**, 2071–2075 (1994).

3. L. J. Wang, A. Kuzmich, and A. Dogariu, Gain-assisted superluminal light propagation Nature **406**, 277 (2000)

4. M. D. Stenner, D. J. Gauthier, and M. A. Neifeld, "The speed of information in a 'fast- light' optical medium," Nature **425**, 695-698 (2003)

5. H. He, Z. Hu, Y. Wang, L. Wang, and S. Zhu, "Superluminal light propagation assisted by Zeeman coherence," Opt. Lett. 31, 2486-2488 (2006)

6. Luc Thévenaz, "Slow and fast light in optical fibres", Nature Photonics 2, 474 - 481 (2008) doi:10.1038/nphoton.2008.147

7. M. S. Bigelow, N. N. Lepeshkin, and & R. W. Boyd, Superluminal and slow light propagation in a room-temperature solid. Science **301**, 200–202 (2003).

8. S. Longhi, M. Marano, P. Laporta, and Belmonte, M. Superluminal optical pulse propagation at 1.5 μm in periodic fiber Bragg gratings, Phys. Rev. E **64**, 055602(R) 1–4 (2001)

9. A. Lezama, S. Barreiro, and A. M. Akulshin, "Electromagnetically induced absorption," Phys. Rev. A **59**, 4732-4735 (1999)

10. A. Naweed, G. Farca, S. I. Shopova, and A.T. Rosenberger, "Induced transparency and absorption in coupled whispering-gallery micro resonators Phys. Rev. A **71**, 043804 (2005)

11. Q. Xu, J. Shakya, and M. Lipson, "Direct measurement of tunable optical delays on chip analogue to electromagnetically induced transparency," Opt. Express **14**, 6463-6468 (2006);

12. S. Manipatruni, C.B. Poitras, Q. Xu, and M. Lipson, "High Speed Electro-Optic Tuning of the Optical Quality Factor of a Silicon Micro-cavity," Optics Letters Vol. **33**, No. 14

13. J. Pan, Y. Huo, K. Yamanaka, S. Sandhu, L. Scaccabarozzi, R. Timp, M. L. Povinelli, S. Fan, M. M. Fejer, and J. S. Harris, "Aligning microcavity resonances in silicon photonic-crystal slabs using laser-pumped thermal tuning," Appl. Phys. Lett. 92, 103114 (2008)

14. M. Borselli, High-Q Microresonators as Lasing Elements for Silicon Photonics. Thesis, California Institute of Technology, Pasadena (2006).

Chapter 8
ELECTRO-OPTICALLY TUNABLE SLOW-LIGHT ON SILICON

Abstract: We demonstrate, for the first time, an electro-optically tunable delay element on a silicon micro-chip. We show tunable delays between 12 ps to -35 ps. We demonstrate electro-optic ultra-fast control of the optical quality factor of an on-chip silicon micro cavity. The micron-size cavity is formed by light confinement between two micro ring resonators acting as frequency selective mirrors. The ring resonators are integrated into PIN junctions enabling ultra-fast injection and extraction of carriers. We show tuning of the cavity quality factor from 20,000 to 6,000 in under 100 ps. We demonstrate both, high Q to low Q, low Q to high Q transitions.

8.1 Introduction

This chapter is an attempt to integrate the electro-optic functionalities developed in the earlier sections with the slow-light elements of the section 7. The ability, to delay and advance optical pulses, was believed to be essential for optical networks on chip leading to a large volume of literature between 2001 and 2007. However, towards 2007, the stringent limitation of slow light due to bandwidth-delay product limit became evident. However, the level of electro-optic integration shown in this work remains the state-of-the-art for silicon slow light integration to date.

First step towards developing a tunable slow light element based on micro-rings is to show electrically tunability of optical bandwidth. The first section, therefore, concentrates on electro-optically tunable optical bandwidth.

8.2 Electro-optic bandwidth tuning

Dynamic tuning of optical micro-resonators has been shown to provide new functionalities for on-chip optical communications and information processing [1-3]. Fast tuning of the optical quality factor (Q) is an important condition for optical processing based on dynamic photonic structures [4, 5]. To date, most approaches have shown only a weak tuning of the Q [6] or used all-optical techniques [7] or slow thermal processes [8, 9]. However, an integrated electro-optic ultra-fast tuning mechanism for the Q will enable important functionalities such as on-chip optical buffers, wavelength converters, reconfigurable switches and filters for high speed planar integrated optics. In this paper, we show strong changes in the Q of a micron size cavity, from 6,000 to 20,000, achieved by in-plane integrated electrooptic tuning in under 100 ps.

8.3 Device Description

The cavity used here consists of two micro-rings which are coupled to a pair of parallel waveguides. An optical cavity is formed by confinement of light between the two resonators which act as reflectors near their resonant wavelengths. By controlling the center wavelength of the resonators, one can change the reflectivity of the mirrors and control the quality factor of the cavity formed. The existence and nature of a super mode formed by

confinement of light between two resonators has been theoretically and experimentally described earlier in detail [10, 11]. The device, as shown in Figure. 8.1 a, consists of two micro-rings each with a diameter of approximately 14 μm which are coupled to a pair of parallel waveguides. In Figure. 8.1 b, we show the transmission spectrum of the device for TE polarized light (dominant electric field parallel to the silicon substrate). The measured transmission spectrum agrees with a time domain model where the optical transmission is calculated iteratively. The coupling coefficient from the waveguides forming the straight sections to the ring is 0.8 % and the propagation loss of the curved waveguide forming the ring is 8.0 dB/cm.

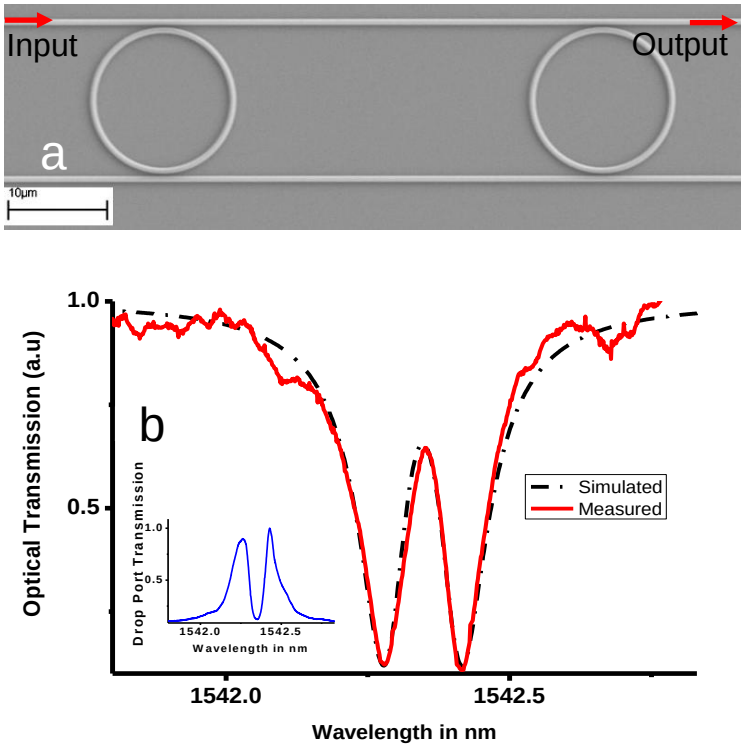

Figure. 8.1. a) SEM image of double ring cavity. b) Transmission Spectrum of the device (the drop port spectrum is shown in the inset)

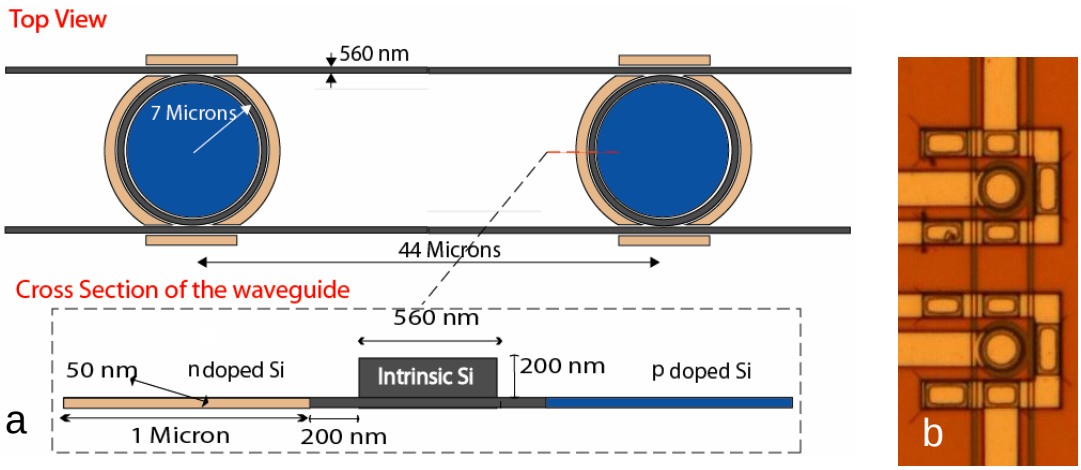

Figure. 8.2. a) Schematic of electro-optically integrated double ring cavity. b) Microscope image of the device

The device is defined on a silicon-on-insulator (SOI) wafer integrated into an electro-optic structure by creating PIN junctions, which allows for the electro-optic tuning of the resonances of the resonators. The coupling waveguides and the rings all have a width 560 nm and a height 250 nm. The center-to-center (CTC) distance between the waveguides forming the rings and the straight waveguides is 720 nm, and the CTC distance between the rings is 44 μm (see Figure. 8.2 a). Concentric p+ and n+ doped regions are defined inside and around the resonating devices to allow for electrical carrier injection and extraction, which modify the index of refraction of the Si and in turn control the spectral position of the resonances. The microscope image of the device with metal pads for electrical probing is shown in Figure 8.2 b.

The PIN junction induces ultra-fast changes in carrier concentrations by active injection and extraction of carriers. The carriers can be extracted in

~10 ps, a value which is limited only by the time taken by the carriers to drift across the waveguide at the saturation velocity of 10^7 cm/s (which is determined by the optical phonon generation rate in silicon). The injection transients can also be as short as ~50 ps [12]. The structure is capable of producing index changes at rates of 10 GHz with relative index change ratio $\delta n/n > 10^{-4}$.

The wave-guiding structures are defined on an SOI substrate using electron beam lithography (e-beam) followed by reactive ion plasma etching. After the definition of the waveguides, the excess Si is etched away but 50 nm to allow for the injection and extraction of carriers from the intrinsic Si waveguide. N^+ and P^+ regions of the diode are each defined with e-beam lithography and implanted with Phosphorus and Arsenic to create concentrations of 10^{19} cm^{-3}. The device is then clad with 1 μm of plasma enhanced vapor deposited SiO_2 and annealed to activate the dopants. Following the activation, e-beam and RIE are used again to define and etch vias through the cladding down to the doped regions for the electrical contacts using nickel. Aluminum contact pads are then defined using e-beam lithography and evaporation followed by lift-off.

8.4 Dynamic electro-optic bandwidth tuning of the device

By controlling the center wavelength of the resonators, one can change the reflectivity of the mirrors and control the super mode quality factor (i.e. the transparency window). Hence, the spectral width of the cavity formed between the two resonators is a strong function of the frequency separation

between the resonant frequencies of the two micro-rings. We measured the transmission spectra of the device for various applied voltages as the central wavelength of the ring 1 (corresponding to center wavelength of 1542.28 nm) is changed by injection of free carriers through the PIN junction. As free carriers are introduced into ring 1, free carrier dispersion [7] leads to change in center wavelength of ring 1 which leads to a change in the spectral width of the super mode resonance. We measured the transmission spectra of the device as applied voltage is varied from 0 V to 1.2 V.

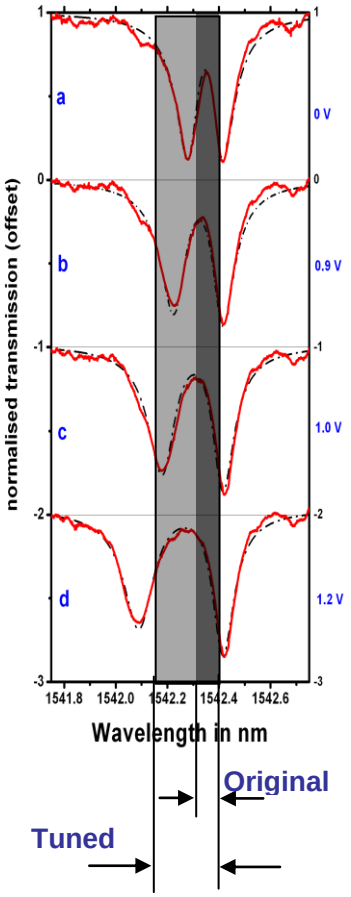

Figure. 8.3. (Color online) Experimental transmission spectra (red, solid line) and theoretical fits (black, dashed lines). The curves correspond to transmission spectra as the applied voltage to one of the resonator is varied from 0 V to 1.2 V. The transmission spectra b-d are vertically offset for clarity.

We can see from the transmission characteristics in Figure. 8.3 (a) that a super mode with a Q of 20,000 is formed when no voltage is applied in the coupled ring device. When a forward bias is applied, the spectral width of the ransparency region is clearly increased indicating a decrease in the cavity Q to 6000 (Figs. 8.3 b-d). Hence, we show that the Q of the transparency window can be electro-optically tuned from 20,000 to 6,000 by controlling the carrier concentration in the device.

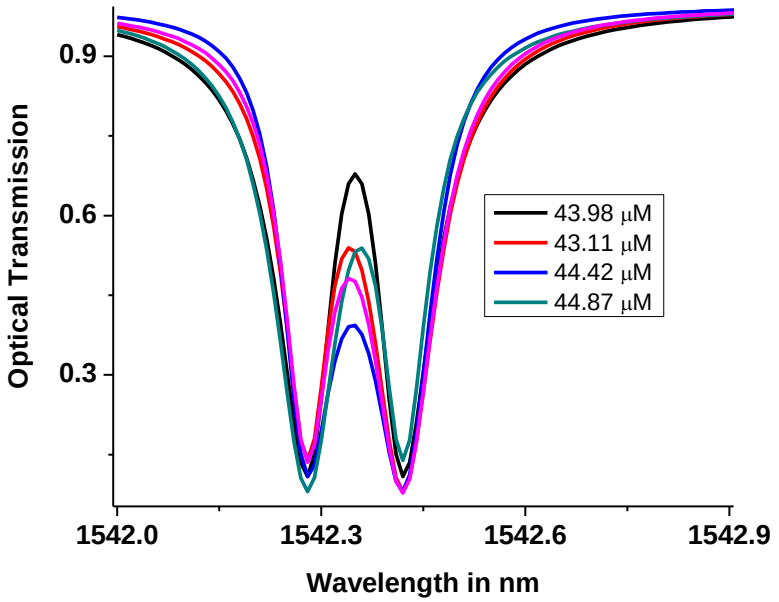

Figure. 8.4 Sensitivity of the super mode transmission to changes in the distance between the coupled cavities. A 1% change in the distance between the cavities shows a 30% change in the transmission of the super mode.

In order to ensure that the effect observed here is due to the presence of the super-mode, and not due to spectral filtering, we simulated the sensitivity of the super mode transmission feature to changes in the cavity length. We show that the super mode transmission spectrum is significantly affected as

the length of the cavity in the model is varied from 43.11 μm to 45.26 μm corresponding to a ± 2 % change in the cavity length (Figure. 8.4). Note that in these simulations the resonance wavelength of the cavities is kept the same.

For example, at 44.42 μm, a 1 % change on the cavity length from the nominal length leads to a 30% change in the super mode peak transmission indicating that the transparency window indeed corresponds to a super mode formed by confinement of light in the cavity formed by the two resonators acting as reflectors. We used a time domain iterative model to calculate the fields in the resonators.

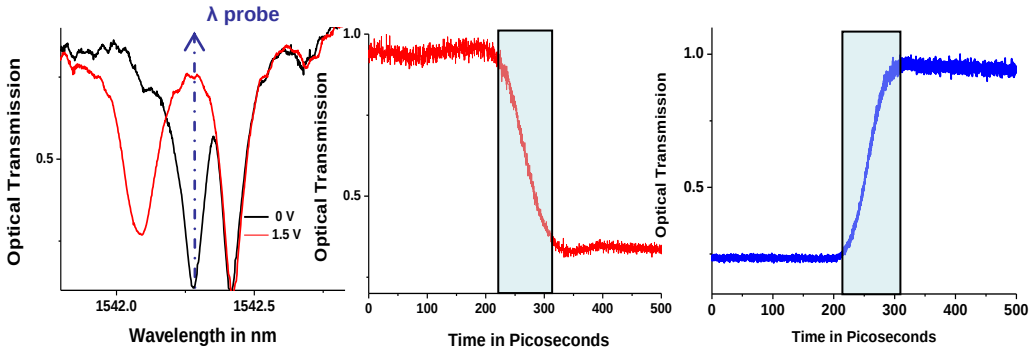

(a) (b) (c)

Figure. 8.5. a) The red line shows the transmission spectrum when a forward bias is applied to the ring corresponding to lower wavelength resonance. The black line shows the transmission of the unperturbed device. b) Time response of the transmission at λ_{probe} as the Q of the device is switched from a low Q to state to a high Q state. c) Time response of the transmission at λ_{probe} as the Q of the device is switched from a high Q to state to a low Q state.

We measured ultra-fast transitions of the *Q* by probing the transmission dynamics through the device at a wavelength where the modulation of Q

leads to a modulation in the amplitude of the transmitted light. We applied a 0.1 GHz repetition rate square wave with a 5 V amplitude and 100 ps fall and rise times. The DC bias voltage was varied between -3.5 V and zero to obtain optimum transitions. Note that no pre-emphasis or pre-distortion of the electrical signals has been used. We use forward bias to inject carriers and reverse bias to actively extract the carriers. In Figure. 8.5 a we show the transmission spectra through the device in a low Q state (injected carriers) and in a high Q state (depleted carriers). We choose a wavelength λ_{probe} on the spectrum where a change in the Q produces a corresponding change in the amplitude of the transmitted light. In Figure. 8.5 b we show the time response of the transmission at λ_{probe} as the Q of the device is switched from a low Q to state to a high Q state and in Figure. 8.5 c as the Q of the device is switched from a high Q to state to a low Q state. One can see that both transitions (low Q to high Q, high Q to low Q) occur within 100 ps.

The demonstrated approach is an order of magnitude faster than the all-optical methods in restoring the cavity to a high Q state (or a low Q state depending on the scheme) after the carriers are injected. The all-optical methods rely on recombination of the carriers to restore the unperturbed cavity condition. In contrast an electrooptic integrated device as shown here can restore the cavity condition by active extraction of free carriers. A fast cyclical modulation of the Q from low to high and high to low states is essential for various optical processing techniques [5, 6]. Novel device structures may be used to induce fast extraction as well as injection of carriers in ~10 ps using high field carrier transport [13].

In summary, we have shown ultra-fast tuning of the optical quality factor in an integrated photonic structure on a silicon chip in 100 ps. Control of the cavity Q in these time scales will enable novel functionalities such as wavelength conversion, pulse compression, fast tunable optical filters, delay lines and light-stopping schemes, previously only demonstrated using all-optical systems [1, 7].

8.5 Electro-optic tuning of the slow-light device

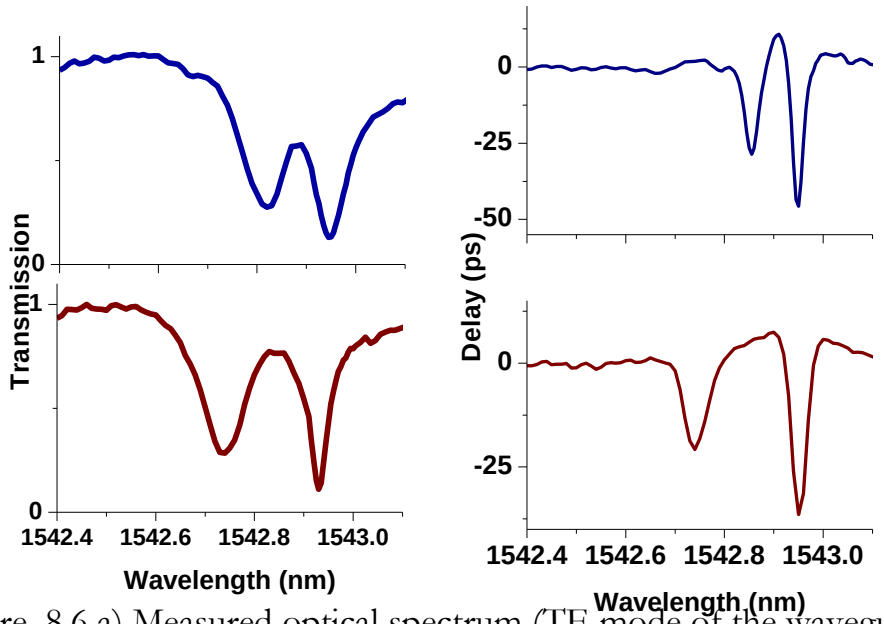

Figure. 8.6 a) Measured optical spectrum (TE mode of the waveguides, Dominant electric field parallel to the plane of the chip). b) Measured delay through the device for 0 V and 1.4 V applied voltage to the left ring.

We measured the tunable delay spectrum at the output port with tunability from 5.51 ps to -28 ps corresponding to group indices index of 37.2 to -190 at 1542.85 nm. We measure a peak delay of 10.5 ps at 1542.91 nm. The experimental setup to measure the optical delay is shown in Figure. 8.2. A continuous wave light from a tunable laser source is polarized and

modulated at 1 GHz, and coupled into the device. A 90-10 splitter is used prior to the input polarization controller for signal comparison during the measurement. A polarization filter is used at the output of the chip to isolate the wanted polarization. The switch is used to acquire and compare the delayed and original signals alternatively. We estimate the relative group delay by comparing the probe and the output in the time domain. The time delay of the optical signal can be tuned by adjusting the spectral features of the device via carrier injection. The measured spectrum for the quasi-TE mode (dominant E-field parallel to the plane of silicon) is shown in Figure. 8.3a. The measured optical delay spectrum is shown in Figure. 8.3b, where the pulse delay is tuned from 5 ps to -28 ps corresponding to an effective group index range of 37.2 to -190. Note that the maximum pulse delay is limited only by the waveguide losses, which in turn are limited by the fabrication process.

In conclusion, we demonstrate an electro-optic tunable delay element with tunable delay between 5.51 ps and -28 ps corresponding to group indices between 37.2 and -190. This device is the demonstration of another important on-chip component to enable optical networks on chip.

REFERENCES

1. Q. Xu, P. Dong, M. Lipson, "Breaking the delay-bandwidth limit in a photonic structure", Nature Phys. 3, 406–410 (2007).

2. S. Preble, Q. Xu, M. Lipson , "Changing the color of light in a silicon resonator", Nature Photonics 1, 293 - 296 (2007)

3. P. Dong, S. F. Preble, J. T. Robinson, S. Manipatruni, M. Lipson, "Inducing Photonic Transitions between Discrete Modes in a Silicon Optical Microcavity", Phys. Rev. Lett. 100, 033904 (2008)

4. M. F. Yanik, S. Fan, "Stopping light all-optically", Phys. Rev. Lett. 92:083901 (2004).

5. M. F. Yanik, S. Fan, "Time reversal of light with linear optics and modulators", Phys.Rev. Lett. 93:173903 (2004).

6. Q. Xu, B. Schmidt, S. Pradhan, and M. Lipson, "Micrometre-scale silicon electro-optic modulator ", Nature, Vol. 435, pp. 325-327, (2005)

7. Y. Tanaka, J. Upham, T. Nagashima1, T. Sugiya, T. Asano, S. Noda, "Dynamic control of the Q factor in a photonic crystal nanocavity", Nature Materials 6, 862 - 865 (2007)

8. M. Popović, "Theory and design of high-index-contrast micro photonic circuits," Ph.D. Thesis, Dept. of Elec. Engineering and Computer Science, Massachusetts Institute of Technology (MIT), Cambridge, Massachusetts, USA, Feb. 2008

9. L. Chen, N. Sherwood-Droz, and M. Lipson, "Compact bandwidth-tunable microring resonators," Opt. Lett. 32, 3361-3363 (2007)

10. Q. Xu, Q, S. Sandhu , M. Povinelli, J. Shakya, S. Fan, M. Lipson, Experimental Realization of an On-Chip All-Optical Analogue to Electromagnetically Induced Transparency, Phys. Rev. Lett., Vol. 96, 123901, 31 Mar. 2006.

11. L. Maleki, A. B. Matsko, A. A. Savchenkov, and V. S. Ilchenko, "Tunable delay line with interacting whispering-gallery-mode resonators," Opt. Lett. 29, 626-628 (2004)

12. S. Manipatruni, Q. Xu, B. Schmidt, J. Shakya, M. Lipson, "High Speed Carrier Injection 18 Gb/s Silicon Micro-ring Electro-optic Modulator," Lasers and Electro-Optics Society, 2007. The 20th Annual Meeting of the IEEE , vol., no., pp.537-538, 21-25 Oct. 2007

13. S. Manipatruni, Q. Xu, and M. Lipson, "PINIP based high-speed high-extinction ratio micron-size silicon electrooptic modulator," Opt. Express 15, 13035-13042 (2007)

14. Y. A. Vlasov, M. O'Boyle, H. F. Hamann, and S. J. McNab, "Active control of slow light on a chip with photonic crystal waveguides," Nature 438, 65-69 (2005)

15. Q. Xu, J. Shakya, and M. Lipson, "Direct measurement of tunable optical delays on chip analogue to electromagnetically induced transparency," Opt. Express 14, 6463-6468 (2006)

16. T. Tanabe, M. Notomi, E. Kuramochi, A. Shinya, and H. Taniyama, "Trapping and delaying photons for one nanosecond in an ultrasmall high-Q photonic-crystal nanocavity," Nature Photon. 1, 49-52 (2007).

17. A. Shacham, K. Bergman, and L. P. Carloni, "On the Design of a Photonic Network-on-Chip," in Proceedings of IEEE International Symposium on Networks-on-Chips (IEEE, 2007), pp. 53-64.

18. R. Soref, B. Bennett, "Electrooptical effects in silicon," IEEE J. Quantum Electron., 23, 123- 129 (1987)

19. S. Manipatruni, C. B. Poitras, Q. Xu, and M. Lipson, "High-speed electro-optic control of the optical quality factor of a silicon microcavity," Opt. Lett. 33, 1644-1646 (2008)

Chapter 9
OPTICAL NON-RECIPROCITY IN OPTOMECHANICAL STRUCTURES

Abstract: In this section, I demonstrate that an optomechanical system where dominant light-matter interaction takes place via linear momentum exchange between light and a mechanical structure, exhibits a non-reciprocal behavior. As an example, I propose a micro-scale optomechanical device that can exhibit a non-reciprocal behavior in a micro photonic platform operating at room temperature. I show that depending on the direction of the incident light, the device switches between a high and low transparency state with more than 20 dB extinction ratio. This section is aimed came out of exploration of new problems that can be solved due to the ability to integrate photonics on a evolved fabrication platform such as silicon photonics. Non-reciprocity is a long standing problem in optics going back to early classical electromagnetism [8, 9]. While several approaches have been attempted, an approach that is suitable for a non-magnetic solid state system has not been found so-far. This is the first time, non-reciprocity has been proposed without relying on the material's electrical or magnetic responses.

9.1 Introduction

Breaking the reciprocity of light on-chip can lead to an important new class of optical devices such as isolators, which are critical for the development of photonic systems. Traditional methods for creating non-reciprocal devices

rely on magneto-optic media, optically-active media or photovoltaic electro-optic crystals[1-4]. Non-reciprocal behaviour has also been studied in time varying media[5-6], bi-anisotropic media[7,8] (such as magneto-electric media), and relativistic moving media[9]. However, the development of non-reciprocal devices for a micro-photonic platform remains a challenge[6]. Hence, it is of great interest to pursue alternative mechanisms to break the reciprocity of light on a micro-scale platform. Here, we show non-reciprocity by exploiting a fundamental difference between forward and back moving light: its momentum. Recent work in optomechanics[10], enabled by advances in optical micro cavities[11] and nano-electro-mechanical systems[12], has shown tremendous potential for a new class of micro-scale devices[13-16] and novel physical phenomena such as optomechanical cooling[17-22]. In this paper, we show that when the dominant light-matter interaction takes place via momentum exchange, optomechanical devices can exhibit non-reciprocal behaviour; since their optical spectral characteristics are strongly dependent upon the direction of the incidence of light. We propose a silicon based micro-opto-mechanical device that exhibits a non-reciprocal behaviour with a contrast ratio > 20 dB.

9.2 Principle of Operation

An example of an optomechanical structure which interacts with light through linear momentum exchange consists of an in-line Fabry Perot (FP) cavity with one movable mirror and one fixed mirror (Figure. 9.1). The emergence of non-reciprocity in such as system can be understood as follows (see Figure 9.1 a): For a left-incident beam at the optical resonance frequency, the net momentum imparted per second on the movable mirror

is -((2η-1) - R) I/c (where η is the power build up factor of the cavity, R is the power reflectivity of the FP cavity, I is the incident power and c the speed of light in vacuum, and the negative sign indicates that the direction of the force is away from the cavity). On the other hand, for a right-incident beam the net momentum imparted per second on the movable mirror is -((2η -1)+ R) I/c. Hence the differential radiation force for left and right incident beams is $2RI/c$ producing a non-reciprocal mechanical response from the mirror leading to non-reciprocal optical transmission spectra.

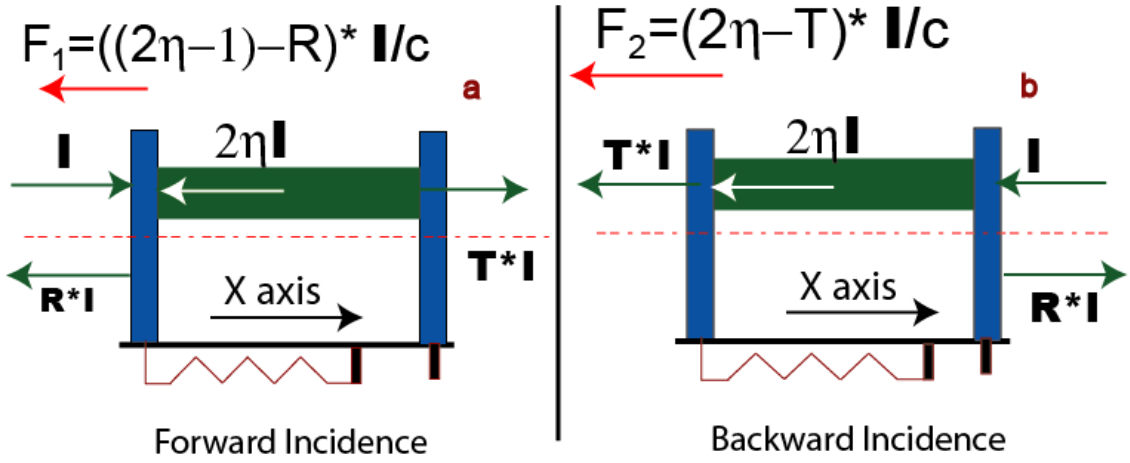

Figure 9.1. Optomechanical Scheme under consideration: Non-reciprocal mechanical response. a) Forward incident light b) backward incident light

9.3 Device Description

To illustrate the non-reciprocal behavior in a realistic micro-optomechanical device we describe a representative device which can be fabricated in a silicon material system. The device (Figure. 9.2) consists of a quasi-1D standing wave cavity formed by two quarter wave Bragg reflectors with one of the mirrors suspended via micro-cantilevers[24]. The mirrors forming the cavity are fabricated in a high index contrast system (the refractive indices of

Si and SiO_2 are approximately 3.5 and 1.5 respectively). Spring constants spanning several orders of magnitude can be achieved (typically from 10^{-5} N m^{-1} to 1 N m^{-1} [24]), by varying the materials, geometry and the arrangement of the cantilevers. We model the movable mirror as a vertical translation plate supported by four beams. Using COMSOL[26] software package we compute the mechanical response of the structure by including material properties and boundary conditions into a Finite Element Method (FEM) based solver. No angular displacement is allowed because the beams are connected to the mirror which remains parallel to the substrate under nominal plate movements. The spring constant associated with four fixed beams is given by $4Ewt^3/l^3$ where E is the young's modulus and w, t, and l are the width, thickness, and length of the silicon beams respectively[25]. In a given material system, the cubic dependence of the spring constant on the aspect ratio (t/l) allows for a wide range of spring constants for this beam geometry. We consider a 10 X 10 μm^2 mirror suspended using micro-cantilevers of thickness 110.5 nm ($\sim\lambda_c/4n_{si}$ where λ_c is 1550.5 nm and n_{si} (3.5) the refractive index of silicon), 10 μm length, and 100 nm width. The mass of the mirror is 165.26 pg. The spring constant for the chosen dimensions is ~0.06 Nm^{-1}. Using the FEM software we calculate the mechanical displacement of the movable mirror for ~666 pN ($2I/c$) applied force corresponding to a net radiation force from a 100 mW beam reflected perfectly from the mirror (see Figure. 9.2) to be on the order of 10 nm. The bandwidth of the optical cavity formed by the mirrors is primarily determined by the reflectivity of the mirrors. We show the optical transmission characteristics of the device in Figure. 9.2 d. We consider quarter wave stacks on either side formed by alternating layers of Si and SiO_2

with 2 layers of deposited silicon and three layers of deposited oxide.

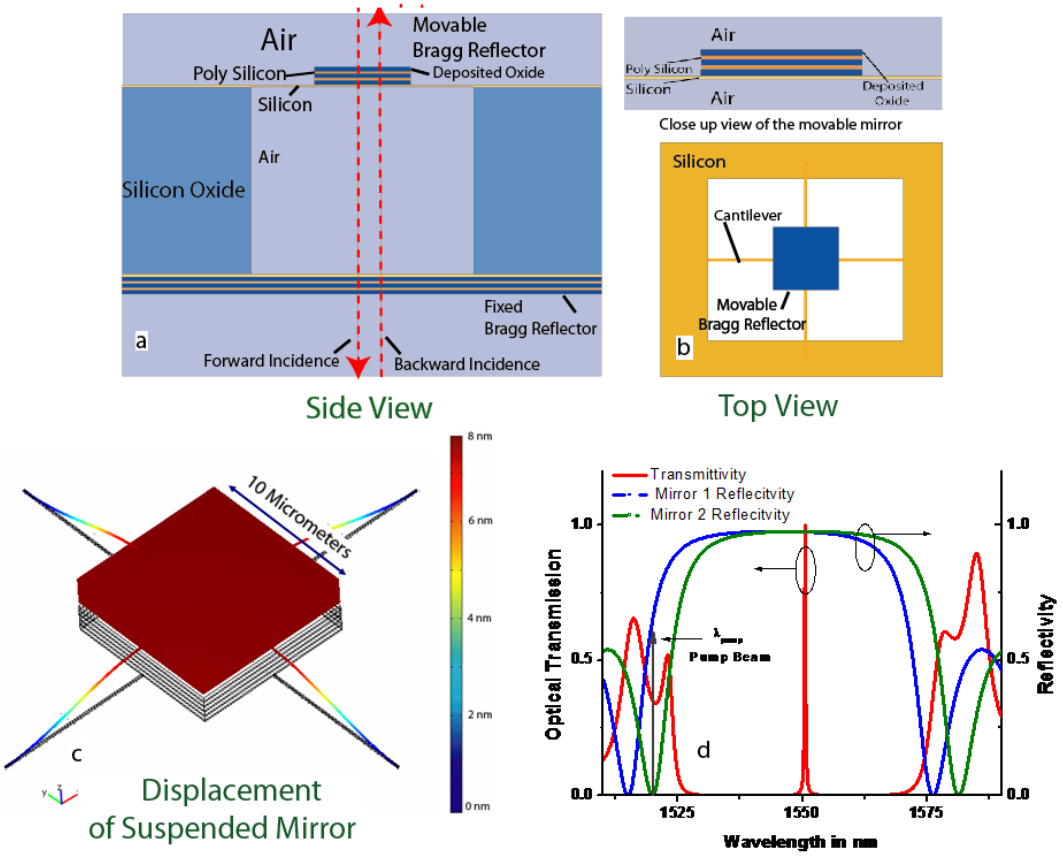

Figure 9.2. Proposed optomechanical device for realizing non reciprocal transmission spectra a) Side View b) Top View c) Mechanical response of the suspended mirror for a radiation force corresponding to 100 mW incident power. C) Optical Transmission through the device for low light intensities. Reflectivity Spectra for the mirrors are shown in dotted lines. Layer thicknesses of the mirrors are slightly offset (5 nm) to allow for a pump-probe measurements. An optional mechanical stop can be added near the movable ring to minimize the insertion losses.

The mirrors form an air filled cavity of length ~$50\lambda_c/2$. The quality factor of the cavity ($Q=\lambda_c/\Delta\lambda$) is ~5200 centred at ~ λ_c=1550.5 nm. The mirror layers have thicknesses of $21\lambda_{mirror1}/4\ n_{si}$, $21\lambda_{mirror2}/4\ n_{si}$.

9.4 Non-reciprocity emerges naturally in a optomechanical system responsive to radiation pressure : Mathematical Modeling

Non-reciprocal behaviour in the proposed structure emerges due to the asymmetry of the radiation pressure on the movable mirror for forward and backward incident light. We model the cantilever dynamics by a driven second order differential system with a non-linear driving function

$$\frac{d^2x}{dt^2}+\frac{b}{m_{eff}}\frac{dx}{dt}+\frac{K}{m_{eff}}x=\frac{F_{RP}(\lambda,x,t)}{m_{eff}} \qquad (1)$$

Where radiation force on the movable mirror is

$$F_{RP}(\lambda,x,t)=\begin{cases} -((2\eta-1)-\mathrm{R}(\lambda,x,t))*\mathrm{I/c} & \text{for forward incidence} \\ -(2\eta-1+\mathrm{R}(\lambda,x,t))*\mathrm{I/c} & \text{for backward incidence} \end{cases} \qquad (2)$$

where I is the power of the incident beam η, R are the intensity build up factor, and reflectivity of the cavity for wavelength λ and movable mirror position x. The position dependent reflectivity $\mathrm{R}(\lambda,x,t)$ is given as a function of displacement x as,

$$\mathrm{R}(\lambda,x,t)=1-\left[\left(\frac{|t_1t_2|}{1-|r_1r_2|}\right)^2\frac{1}{1+4\left(\frac{\sqrt{|r_1r_2|}}{1-|r_1r_2|}\right)^2\sin^2\varphi(x)}\right]^{1/2} \qquad (3)$$

Where $\varphi(x)$ is the phase shift per round trip inside the cavity: $1/2\,\mathrm{Arg}\left[\mathrm{r}_1r_2e^{i\frac{2\pi}{\lambda}(l-x)}\right]$ and r_1, r_2 & t_1, t_2 are the mirror reflectivties and transmittivities; l is the steady state cavity length. We assume a mass of 165.26 pg, spring constant of 0.06 $\mathrm{Nm^{-1}}$ (corresponding to a 10X10 μm^2 Bragg mirror, see Figure.9.2) and a net damping parameter of 10^{-6} $\mathrm{kgs^{-1}}$. The damping mechanisms may include mass damping, stiffness damping,

acoustic leakage at the anchors and thin fluid squeezing[26]. The coupled optomechanical response is calculated at each time step (1 ns ~ $\tau_{mechanical}/1600$) by updating both the optical and mechanical state of the cavity. We also note that the photon life time ($\tau_{photon} = \lambda Q/2\pi c \approx 4.1ps$) is much smaller than the mechanical rise time ($\tau_{mechanical} = b/m \approx 16ns$), which allows for the calculation of the optomechanical response iteratively. We neglect the quantum Langevin noise in calculating the optomechanical response. The transmission spectral characteristics exhibit the classical behaviour of optical bi-stable systems. The transmission spectra of the device for forward and backward incident light are shown in Figure. 9.3. One can see the formation of a non-reciprocal transmission window at 1551.2 nm with a bandwidth of 0.25 nm and a forward to backward incident light extinction ratio of > 16 dB. The transition time for back ward to forward incidence (and vice versa) is on the order of $\tau_{mechanical}$ ($\approx (1/2Q_m) * (\sqrt{K/m_{eff}})$, where Q_m is the mechanical quality factor) given by mechanical design of the movable mirror.

9.5 Optimising the device for low-insertion loss

The insertion loss through the device can be minimized by providing a mechanical stop for the movable mirror. To obtain a unity peak transmission, the FP cavity needs to be perfectly on resonance with the incoming light. However when the cavity is perfectly on resonance, the radiation force on the mirror passes through a maximum leading to instability[13].A mechanical stop allows for peak resonance build up while producing a non reciprocal response. We describe a non-reciprocal optomechanical device to achieve low insertion loss (<0.1 dB), high forward

to backward incidence extinction ratio (>20 dB). In Figure. 9.4, we show the

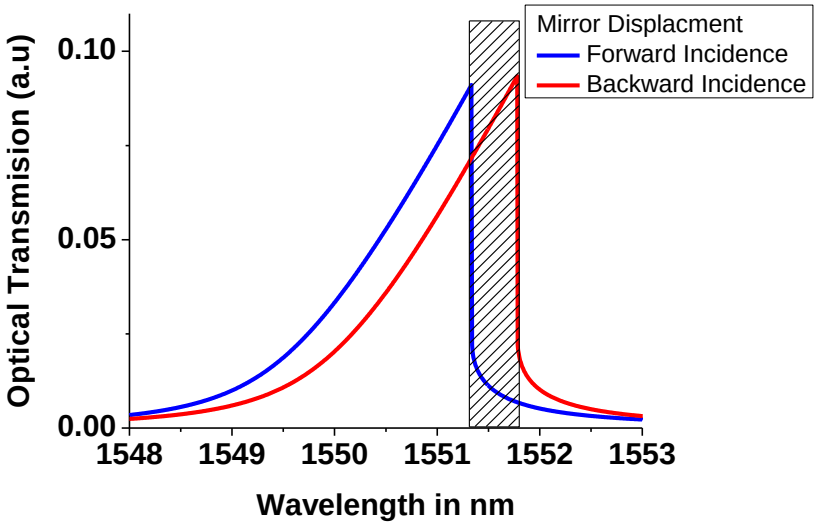

Figure 9.3 a. Transmission spectra of the device for forward and backward incidence of light.

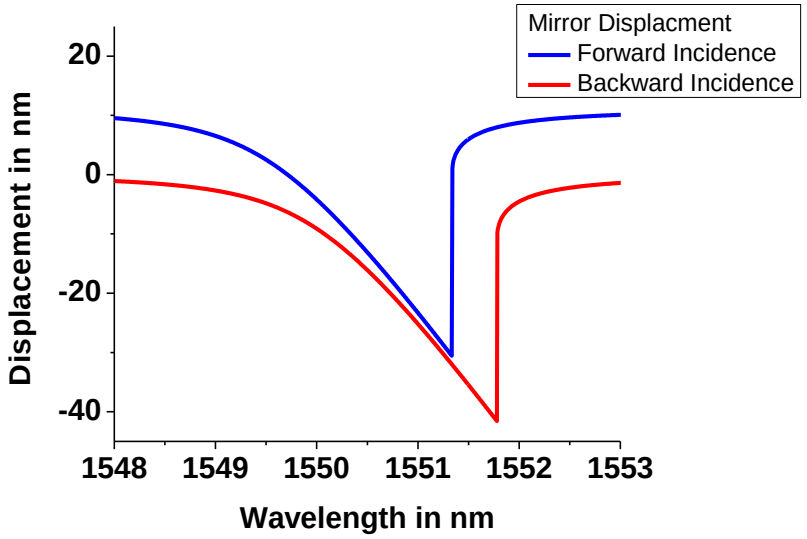

Figure 9.3 b. Steady state displacement of the movable mirror for forward and backward incidence of light.

transmission spectra for forward and back ward incident light of 100 mW power when the mirror is constrained to -30 nm displacement. One can see the formation of a non-reciprocal spectrum with a 0.25 nm bandwidth and a

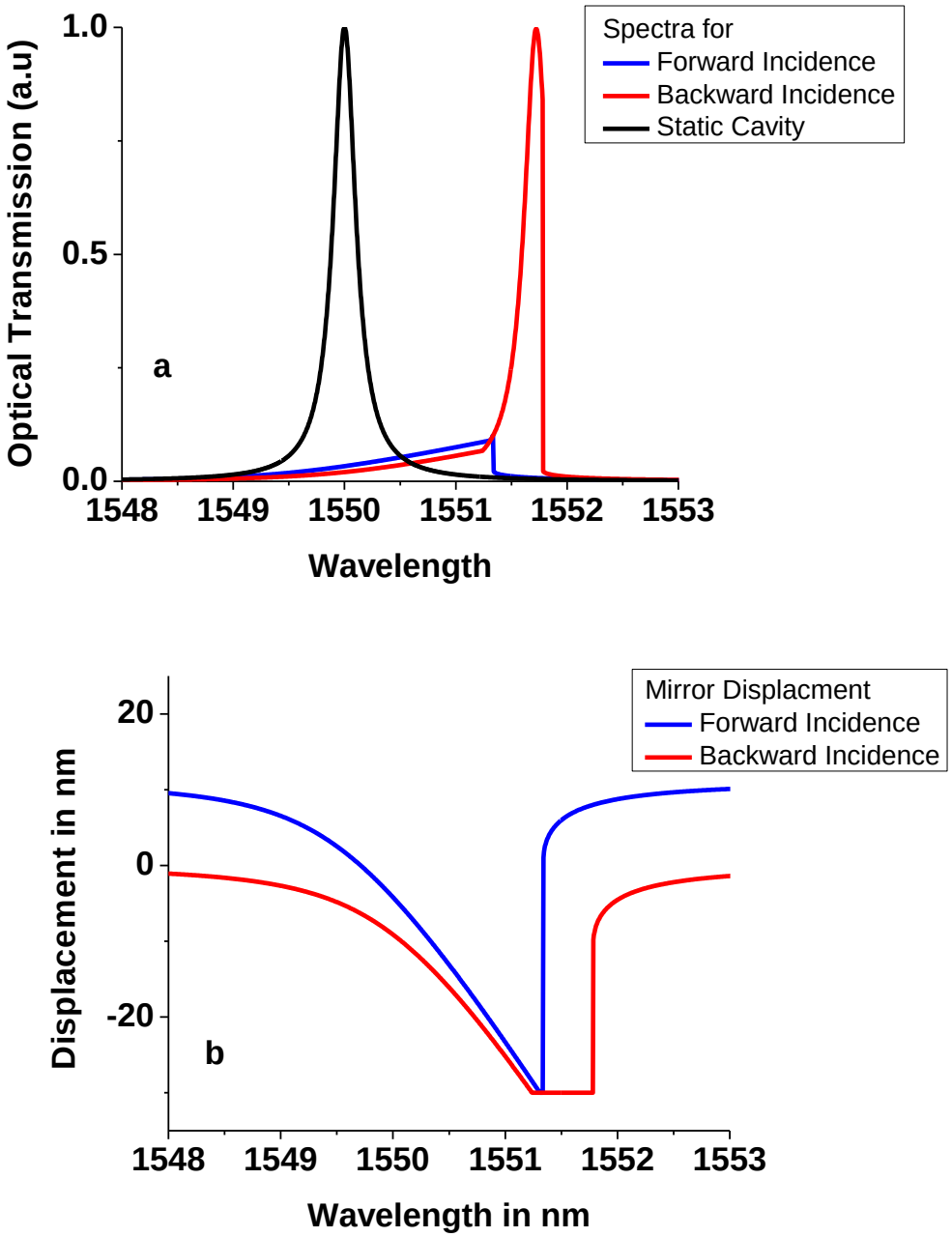

Figure 9.4. a) Transmission spectra of the proposed device for forward and backward incidence of light when the movable mirror is constrained at 30

forward to back ward light extinction ratio > 20 dB. The insertion loss for the backward light is now < 0.1 dB. The bandwidth of the non-reciprocal spectrum can be controlled by choosing the appropriate mirror reflectivity.

We note that an important consideration for a mechanical stop is the affect of stiction force for mechanical objects in close proximity. However earlier works have successfully demonstrated various methods to overcomes this problem[27].

9.6 Effect of thermal noise

The thermal equipartition noise imposes a minimum power condition for observing the non-reciprocal behavior. We estimate the optical power required for the radiation force displacement to exceed the mean square displacement of the mirror for a given spring constant. The minimum optical power required to overcome the thermal position noise is given by $I_{\min} = cK\Delta x$, where $\Delta x_{\min} = \sqrt{kT/K}$, k the Boltzmann constant, K the spring constant, and T=300 K ambient temperature. Following the fluctuation dissipation theorem, this analysis takes into account the Langevin noise[28].
One can see that the net optical power contributing to the non-reciprocal behaviour should be in the range of 10's of mW to overcome the thermal equipartition noise. The optical power I_{min} can be lowered by lowering the spring constant. Even though thermal non-linearity has traditionally been an important constraint to micro-photonic devices[29], we note that the effect of thermal non-linearity will only contribute equally to both directions of incidence. The general principles described here for creating devices with non-reciprocal transmission spectra can be extended to in-plane geometry by employing suspended resonators[30] as frequency selective reflectors[31]. This class of devices with non-reciprocal spectra can enable new functionalities for integrated optical systems.

REFERENCES

1. P. S. Pershan, "Magneto-Optical Effects," *J. Appl. Phys.* 38, 1482 (1967)

2. J. Fujita, M. Levy, R. M. Osgood, Jr., L. Wilkens, and H. Dotsch, "Waveguide optical isolator based on Mach--Zehnder interferometer", *Appl. Phys. Lett.* 76, 2158 (2000)

3. D. C. Jones, G. Cook, "Nonreciprocal transmission through photorefractive crystals in the transient regime using reflection geometry," *Opt. Commun.* 180 391–402 2000

4. R. J. Potton, "Reciprocity in optics," *Rep. Prog. Phys.* 67, 717-754 (2004)

5. D. M. Shupe, "Thermally induced non-reciprocity in the fiber-optic interferometer," Appl. Opt. **19**, 654-655 (1980)

6. Z, Yu, and S. Fan, "Complete optical isolation created by indirect interband photonic transitions," *Nature Photonics* 2009. Advanced online publication doi:10.1038/nphoton.2008.273

7. Bianisotropic media are the most general linear complex media where the constitutive relationships are defined by 4 second rank tensors as $D = \varepsilon_0(\varepsilon.E + \eta_0\xi.H)$, $B = \frac{1}{c_0}(\zeta.E + \eta_0\mu.H)$ where D, E, B and H are the macroscopic electromagnetic fields.

8. J. A. Kong, "Theorems of bianisotropic media," *Proc. IEEE*, Vol. 60, No. 9 September 1972

9. A. Sommerfeld, Electrodynamics. New York: Academic Press, 1952 Page 280

10. T. J. Kippenberg and K. J. Vahala, "Cavity Opto-Mechanics," *Opt. Express* 15, 17172-17205 (2007)

11. K. J. Vahala, "Optical microcavities," *Nature* 424(6950), 839-846 (2003).

12. H. G. Craighead, "Nanoelectromechanical systems," *Science* 290(5496), 1532-1535 (2000).

13. T. Carmon, H. Rokhsari, L. Yang, T. J. Kippenberg, K. J. Vahala, Temporal Behavior of Radiation-Pressure-Induced Vibrations of an Optical Microcavity Phonon Mode , *Phys. Rev. Lett.* 94, 223902 (2005)

14. M. L. Povinelli, J.M. Johnson,M. Loncar, M. Ibanescu, E. J. Smythe, F. Capasso, and J. D. Joannopoulos, "High-Q enhancement of attractive and repulsive optical forces between coupled whispering-gallery-mode resonators," *Optics Express* 13(20), 8286-8295 (2005).

15. M. Eichenfeld, C. Michael, R. Perahia, and O. Painter, "Actuation of Micro-Optomechanical Systems Via Cavity-Enhanced Optical Dipole Forces," *Nature Photonics* 1(7), 416 (2007).

16. P.T. Rakich, M. A. Popovic, M. Soljacic, E. P. Ippen. "Trapping, corralling and spectral bonding of optical resonances through optically induced potentials", *Nature Photonics* 1 (11), 2007, p.658; Wiederhecker, G.S., Chen, L., Gondarenko, A. and Lipson, M., Controlling photonic structures using optical forces, Arxiv 0904.0794v1

17. K. C. Schwab and M. L. Roukes, "Putting mechanics into quantum mechanics," *Physics Today* 58(7), 36-42 (2005).

18. V. B. Braginsky and S. P. Vyatchanin, "Low quantum noise tranquilizer for Fabry-Perot interferometer," *Physics Letters A* 293(5-6), 228-234 (2002).

19. M. D. LaHaye, O. Buu, B. Camarota, and K. C. Schwab, "Approaching the quantum limit of a nanomechanical resonator," *Science* 304(5667), 74-77 (2004).

20. A. Naik, O. Buu, M. D. LaHaye, A. D. Armour, A. A. Clerk, M. P. Blencowe, and K. C. Schwab, "Cooling a nanomechanical resonator with quantum back-action," *Nature* 443(7108), 193-196 (2006).

21. O. Arcizet, P. F. Cohadon, T. Briant, M. Pinard, and A. Heidmann, "Radiation-pressure cooling and optomechanical instability of a micromirror," *Nature* 444(7115), 71-74 (2006).

22. M. Li, W. H. P. Pernice, C. Xiong, T. Baehr-Jones, M. Hochberg, H. X. Tang, *Nature* 456, 480–484 (2008).

23. C. Liu, 'Foundations of MEMS', Pearson. Education Inc., 2006 page 82

24. B. Ilic, H. G. Craighead, S. Krylov, W. Senaratne, C. Ober, P. Neuzil, "Attogram Detection Using Nanoelectromechanical Oscillators", *Journal of Applied Physics*, 95, 3694-3703 (2004)

25. http://www.comsol.com.

26. M. Bao, H. Yang, "Squeeze film air damping in MEMS", *Sensors and Actuators A* 136 (2007) 3–27.

27. Maboudian, R., W.R. Ashurst and C. Carraro, *Tribological challenges in micromechanical systems*. 12 (2002) 95; R. Maboudian and R.T. Howe, Stiction reduction processes for surface micromachines. *Tribol. Lett.* **3** (1997), p. 215.

28. Kubo, R. The fluctuation-dissipation theorem. *Rep. Prog. Phys*. 29, 255–-284 (1966).

29. Carmon, T., Yang, L. & Vahala, K.J. "Dynamical thermal behaviour and thermal self-stability of microcavities". Optics Express 12, 4742 (2004).

30. L. Martinez and M. Lipson, "High confinement suspended micro-ring resonators in silicon-on-insulator," *Opt. Express* 14, 6259-6263 (2006)

31. S. Manipatruni, P. Dong, Q. Xu, and M. Lipson, "Tunable superluminal propagation on a silicon microchip," Opt. Lett. 33, 2928-2930 (2008)

Chapter 10
SYNCHRONIZATION OF OPTOMECHANICAL STRUCTURES

Abstract: We theoretically and numerically demonstrate that long range radiation force mediated mechanical coupling and synchronization arise in optomechanical systems. As an example, we propose a planar micro-scale optomechanical device that exhibits non-linear frequency and phase synchronization of two unlike mechanical resonators. We show frequency and phase synchronization of micro-mechanical systems enabled by radiation force mediated mechanical coupling.

This section is aimed came out of exploration of new problems that can be solved due to the ability to integrate photonics on a evolved fabrication platform such as silicon photonics. The ability to dynamically control the strength, phase and frequency content of mechanical coupling between spatially separated micro-mechanical systems can allow unprecedented flexibility.

10.1 Introduction

Synchronization of time varying systems plays a critical role in a wide range of natural phenomenon[1-3] spanning biological clocks3 to coupled spin transfer nano-oscillators[4-5]. The ability to couple and synchronize distributed nano-scale systems can lead to a new class of chip scale devices with a wide range of applications[1-6]. In particular, controlled synchronization of micro-

mechanical oscillators can enhance signal processing[7-8], sensing[9] and clock distribution[10] using micro scale systems. With the recent advances in meso-scale quantum-electro-mechanics[11-14] and cavity optomechanics[15-21], a direct long range low loss mechanical coupling mechanism may enable a new class of experiments on entanglement[14] and non-locality[22, 23]. However, so far micro-scale mechanical coupling and synchronization between cavities has been limited due to the non-directionality of acoustic radiation, anchor topologies, substrate leakage/material phonon losses as well as restrictions of neighborhood in coupling[6-10].

Here, we propose and study radiation force mediated coupling and synchronization of micro-mechanical resonators. Optically mediated mechanical coupling can enable new level of control due to the ability to manipulate optical modes over a large range of time scales[24] as well as length scales[25] providing a new regime of control on mechanical coupling and mechanical quality factors of micro-mechanical resonators. We show that long range coupling and synchronization between mechanical cavities can be achieved by using optomechanical systems. We show that two dis-similar optomechanical oscillators lock in frequency and phase due to a long range radiation mediated mechanical coupling.

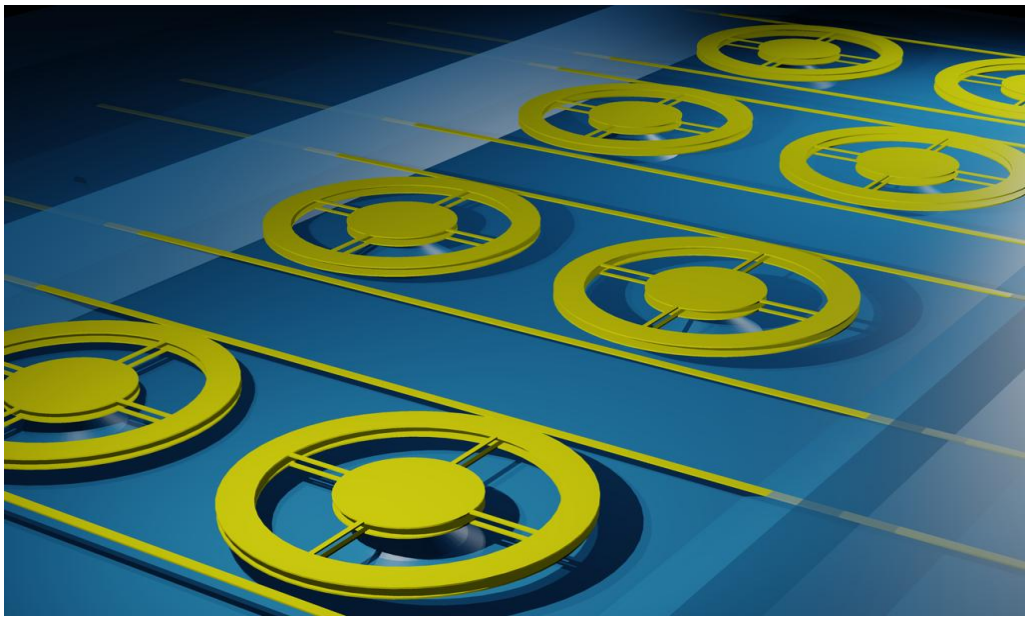

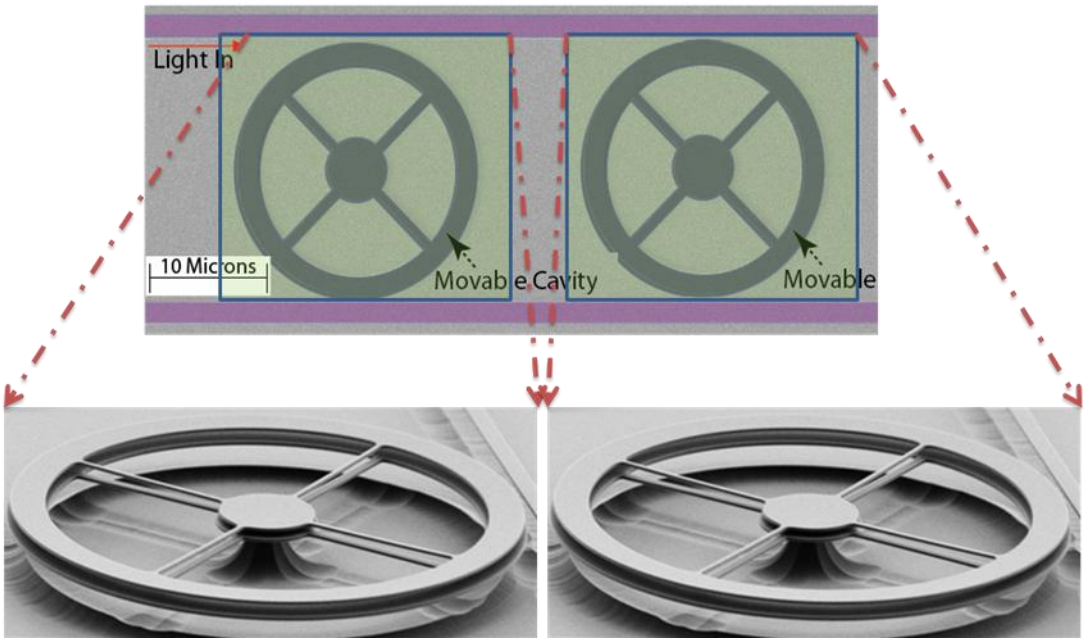

Figure 10.1. Proposed optomechanical device for nonlinear frequency synchronization a) Perspective schematic b) Top View c) The cavities A and B are formed by two evanescent wave optomechanical devices. Waveguides L1 and L2 provide the coupling between the optomechanical devices

10.2 Principle of Operation

We propose novel optomechanical structures which enable mechanical coupling and synchronization of oscillators spread spatially over long length scales. This is enabled by a) Opto-mechanical structures with large coupling ($g_{om} = d\omega/dx$, where ω is the optical resonance frequency and x is the displacement) between the optical and mechanical degrees of freedom b) Strong, long range mechanical coupling mediated via a shared optical mode. Opto-mechanical structures with large coupling can be realized via micromechanical structures with evanescent interactions in a planar integrated device[21, 26]. The long range optical modes spread over 10s μm to cm can be readily achieved in microphotonic platforms using low loss nano-scale wave-guiding systems[27]. In figure 1, we show the schematic of a two cavity optomechanical system where cavities A and B are optomechanical cavities interacting via optical paths L1 and L2 to allow for mutual coupling between the cavities.

We show that optomechanical systems interacting via an optical mode behave as non-linear coupled oscillators with reactive coupling. The governing equations for optomechanical systems driven by radiation pressure can be written as[15, 28]

$$\ddot{x} + 2\Gamma_m \dot{x} + \Omega_m^2 x = -\frac{g_{om}}{m\omega}|\mu|^2 + \chi \tag{1}$$

$$\dot{\mu} = (i\Delta_1 - g_{om}x - \gamma)\mu + \sqrt{\gamma_e}a \tag{2}$$

Where Γ_m is the mechanical mode damping rate, Ω_m the mechanical natural oscillation frequency, $g_{om} = d\omega/dx$ is the optomechanical coupling coefficient, μ is the intra-cavity field normalised such that $|\mu|^2$ is the intra-cavity optical

energy. χ is the white-noise Langevin function representing the noise sources, $\Delta_1 = \omega_p - \omega_0$ represents the frequency detuning of the optical pump field a. The governing equations for two optomechanical cavities with intra-cavity fields μ_a, μ_b coupled through an optical path can be written as

$$\dot{\mu}_a = (i\Delta_{1a} - g_{oma}x_a)\mu_a + \sqrt{\gamma_e}a_{Pump} - (\gamma_e e^{i\varphi}\mu_b + \gamma\mu_a) \tag{3}$$

$$\dot{\mu}_b = (i\Delta_{1b} - g_{omb}x_b)\mu_b + \sqrt{\gamma_e}a_{Pump} - (\gamma_e e^{i\varphi}\mu_a + \gamma\mu_b) \tag{4}$$

where the mechanical displacement of the cavities x_i is driven by the radiation pressure force,

$$\ddot{x}_i + 2\Gamma_{mi}\dot{x}_i + \Omega_{mi}^2 x_i = -\frac{g_{omi}}{m_i\omega_i}|\mu_i|^2 \tag{5}$$

And $e^{i\varphi}$ is the optical phase shift due to time of flight delay for the coupling beams. The subscripts represent the physical constants for the two cavities. The terms $\gamma_e e^{i\varphi}\mu_{b,a} + \gamma\mu_{a,b}$ allow for a mutual coupling between the optomechanical systems similar to a linear coupled oscillator system. For example, when $\varphi = (2n+1)\pi$, $\gamma_e = \gamma/2$, the coupling term reduces to $\gamma_e(2\mu_{a,b} - \mu_{b,a})$, providing a restoring drive force component. Hence, coupled optomechanical systems with radiation force mediated interaction behave similar to a set of coupled non-linear oscillators[29], where the mechanical coupling is mediated through optical fields. We will consider the generalisation to an array of oscillators later[29] in the letter.

10.3 Device Structure

We propose an illustrative optomechanical structure where two optomechanical oscillators produce frequency synchronisation via long range mechanical radiation force mediated coupling. The device is shown in figure

1, where a stacked double micro-ring cavity with evanescent interaction is used as an example optomechanical oscillator. We consider two such optomechanical cavities connected optically[31, 32]. An optical path can be sustained between these cavities to provide the radiation mediated mechanical coupling between the cavities. Each oscillator is formed by a double disc micro-ring cavity with gradient field radiation force to create large optomechanical response. As shown in Figure. 1a, the structure is composed of a pair of vertically stacked micro-rings held by very thin spokes and a pedestal. Earlier works have shown the existance of large optomechanical coefficients[21,26,30] ($g_{om} = d\omega/dx$) and optomechanical oscillations[26] in these cavities mediated by evanescent wave gradient optical forces. We assumed micro-ring optical cavities of radius 15 μm and thickness 190 nm and width 2.5 μm made in a Si3N4 material system. The loaded optical quality factor ($\lambda/\Delta\lambda$) of the double ring cavity is assumed to be Qopt=105 with critical coupling ($\gamma_t = \gamma_{\text{int}} + 2\gamma_{wg}$). The optomechanical cavity is formed by two micro-ring cavities stacked on top of each other separated by an air gap of ~ 600 nm. Due to the relatively small refractive index of Si_3N_4 ($n \approx 2$), strong optical coupling can occur for relatively large gaps between the top and the bottom micro-ring. Figure 2 shows an example of the resonance wavelength splitting for the transverse electric (TE) mode of a 30 μm diameter ring, obtained from numerical simulations. As a result of this coupling, the transverse mode profile splits into symmetric (S, inset A figure 2) and antisymmetric (AS, inset B, figure 2) combinations, leading to two distinct resonant frequencies. One can see that the optical resonance frequnecy of the modes (ω_0) depends exponentially on the separation gap. Such steep gap dependence of the resonant frequencies on the separation

translates into a strong optomechanical constant ($g_{om} = d\omega/dx$) and forcing function for the mechanical oscillator (See Equation 1).

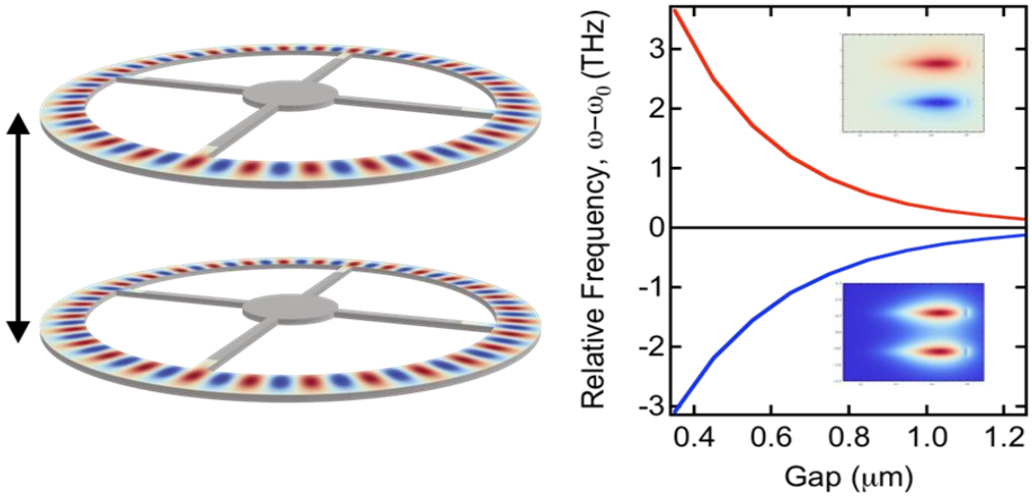

Figure 10.2. Dispersion of the Double ring Optomechanical Cavity for vertical displacement a) Spatial mode profile b) Optical frequency shift of the cavity resonant modes with displacement (Inset A) Anti-symmetric mode B) Symmetric mode)

We show the emergence of synchronization in optomechanical systems where a radiation force mediated coupling is established between the two unlike optomechanical systems. We considered two distinct, dissimilar optomechanical oscillators with optomechanical oscillation frequencies of $\Omega_{OscA} \sim 54.36$ MHz and $\Omega_{OscB} \sim$ 51.88 MHz. The natural mechanical frequencies of the cavities are of $\Omega_{mA} = 50$ MHz and $\Omega_{mB} = 47.5$ MHz with effective masses of 100 pg and mechanical quality factor Qm of 500. The optomechanical coupling constants were assumed to be $k_{omA} = 0.515$, $k_{omB} = 0.617$. The oscillation frequency of the oscillators is higher than the natural frequency due to optical spring effect which produces a non-linear frequency shift in the oscillator frequency. The optical quality factors of the

cavities were Q_{opt1} =10^5, Q_{opt2} =1.2X10^5. We considered both cavities to be critically coupled. The optomechanical cavities were pumped by a single optical source of power Pin= 2 mW centred at ω_p such that, $\Delta_{1a} = \omega_p - \omega_{0a} = \gamma_1/2$, $\Delta_{2a} = \omega_p - \omega_{0b} = \gamma_2/2$. The coupling strength between the cavities decided by the waveguide/optical link loss (α) will be varied to obtain the effect of coupling the optomechanical systems. The optical phase shift due to propagation over the waveguide θ, will also be varied to provide a new level of control of mechanical coupling. The numerical simulations were performed using an ordinary differential equation solver (ode15s) that can handle stiff differential equations. Normalized displacement in nm and energy in mJ were used to convergence. The time step is controlled by the solver to ensure high relative tolerances.

10.4 Frequency Synchronization and controllable Mechanical Coupling

We show controllable frequency locking of optomechanical oscillators interacting via a radiation force mediated coupling. In figure 3 A, we show the frequency content of the mechanical oscillations of the oscillators A and B. We can see the formation of narrow peaks centered at Ω_{OscA} ~54.36 MHz and Ω_{OscB} ~ 51.88 MHz. As we vary the loss through the optical link section, the optomechanical oscillators exhibit a frequency shift due to the optically mediated coupling very similar to a mutual mechanical spring coupling []. As the coupling strength between the oscillators is increased (by controlling the waveguide loss), we can see the locking of frequencies at α=0.18 (corresponding to an optical link loss of -14.9 dB). In figure 3B, we show the frequency content of the mechanical oscillations at α=0.18 showing

identical frequency content. This corresponds to a modest link optical power loss ($20\log 10\alpha$) of -14.9 dB. This corresponds to a distance range of >15 cm in a low loss on chip platform and >100 km using optical fibers, allowing for mechanical coupling and synchronization between objects separated by large distances, with no mechanical interference with other objects in plane.

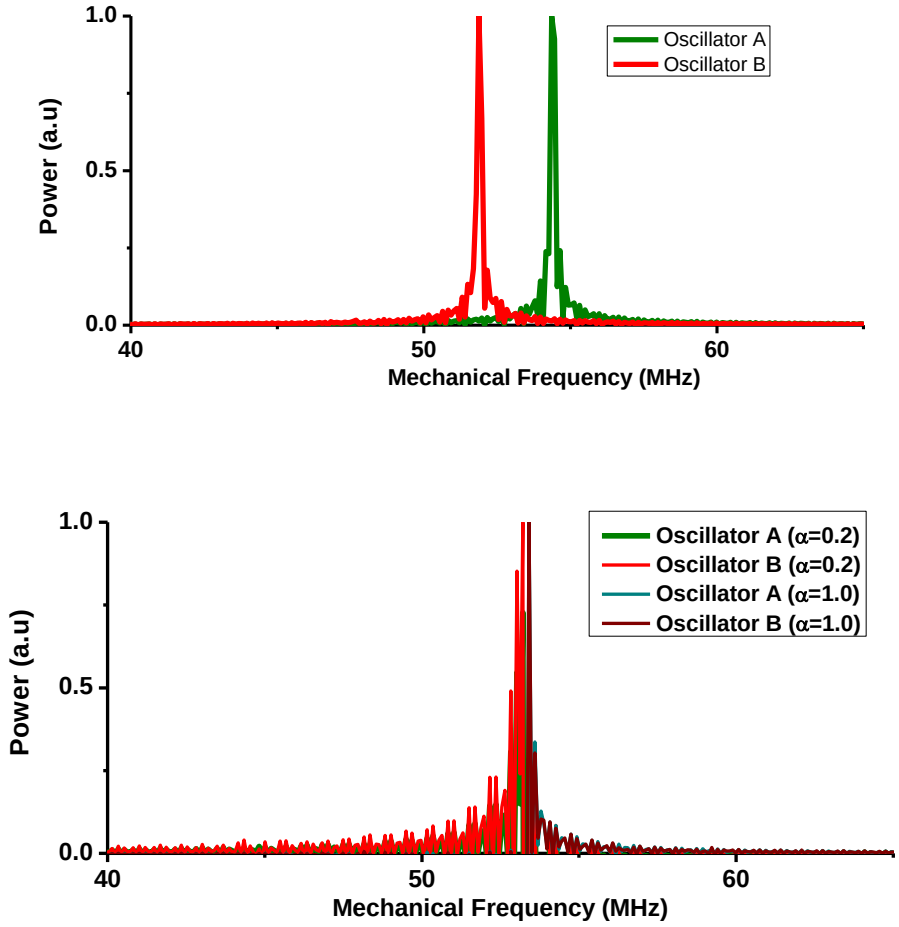

Figure 10.3. Frequency synchronization. A) Frequency content of the oscillations of A & B at zero coupling strength. B) Frequency content of the oscillations of A & B at 0.2 and 1 coupling.

In figure 4, we show the state space diagrams of the system (x1, x2) before frequency synchronization and after synchronization. Figure 4 A shows the

limit cycle in the state space where x1, x2 exhibit un- correlated oscillations. Figure 4B shows the limit cycle at a coupling strengths α =0.18, 1.

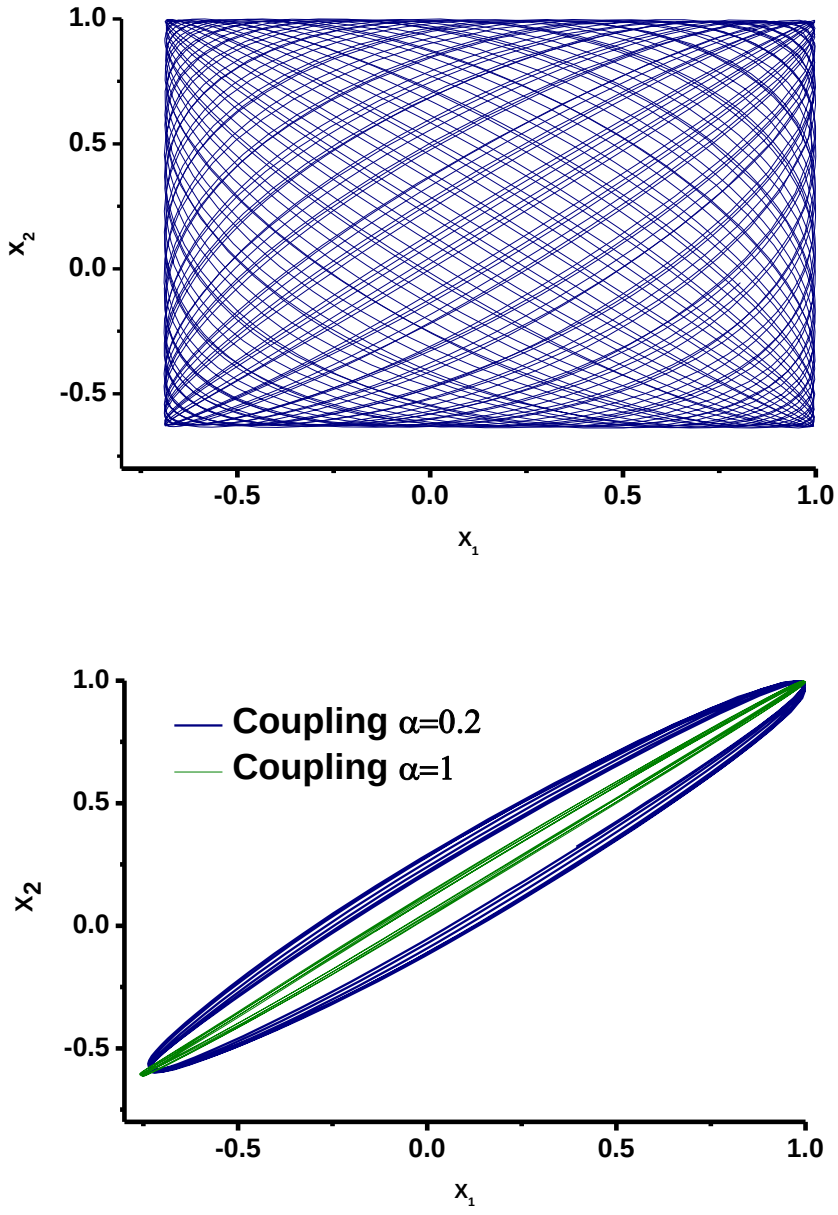

Figure 10.4. Frequency synchronization in state space. A) Limit cycle out of synchronisation B) Limit cycle in synchronisation, near perfect synchronisation with 2.5° residual phase is obtained at strong coupling

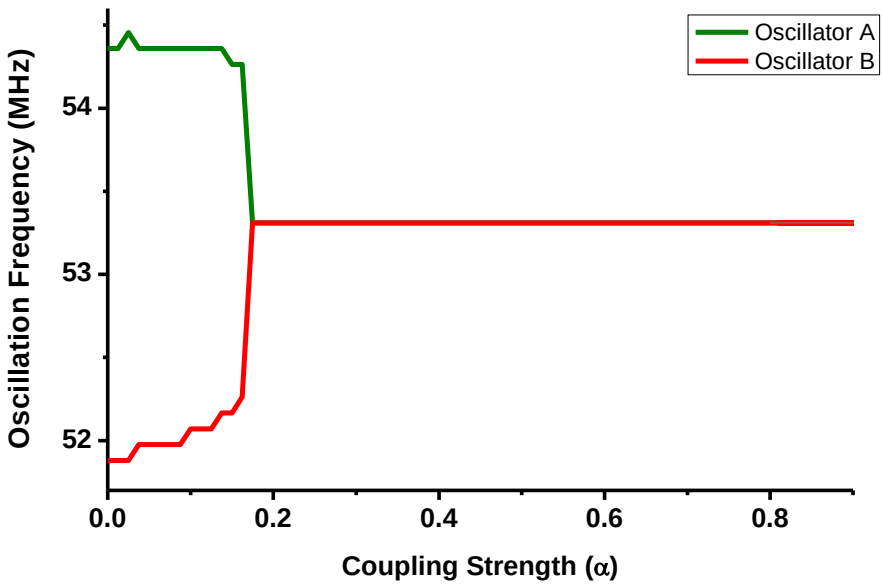

Figure 10.5 A. Frequency Synchronisation of the optomechanical oscillators. At the coupling strength, α=0.18 (optical link insertion loss of -14.5 dB) oscillators A and B lock in frequency. The optical link distance can be as much as 15 cm (for waveguides) and 100 km for fibres.

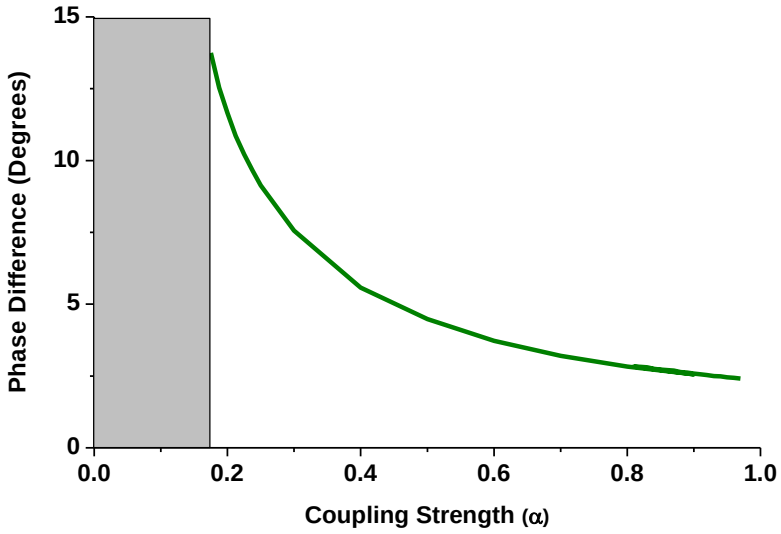

Figure 10.5 B. Phase synchronisation of the optomechanical oscillators. The phase difference approaches 0 asymptotically, as the coupling strength is increased

10.5 Phase Synchronization and controllable Mechanical Coupling Phase

We show controllable phase of mechanical coupling between the synchronized oscillators by varying the phase of the optical link. An analogous dynamical control of the phase of mechanical coupling is infeasible in a micro-platform.

The phase between the mechanical oscillators can be controlled by changing the optical phase of the optical link. In figure 6 A, we show the relative phase between the oscillators for varying optical phase. One can see that arbitrary mechanical coupling phase can be realized between the oscillators. In figure 6 B, we show the state space diagrams of the system (x1, x2) after frequency synchronization while varying the phase term of the optical link. We achieve near phase zero synchronization at $\varphi = (n + 1/3)\pi$, with a controllable phase lag between the oscillations. For a group index of 4, the phase delay corresponds to a control in the optical path length in microns which can also be achieved readily via modern fabrication or tuning techniques.

In Figure 5A, we show the variation of the oscillator frequencies with variable coupling strength (where $20\log 10\,\alpha$ is the optical link loss). In Figure, 5B we show the phase lag between the oscillators as a function of the coupling strength.

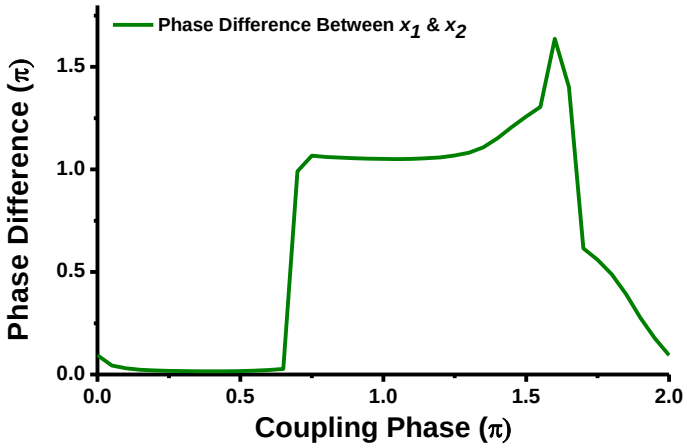

Figure 10.6. A) Optomechanical control on oscillators' relative phase. The phase difference between the oscillators can be controlled optically producing an effect equivalent to controlling the phase of mechanical coupling.

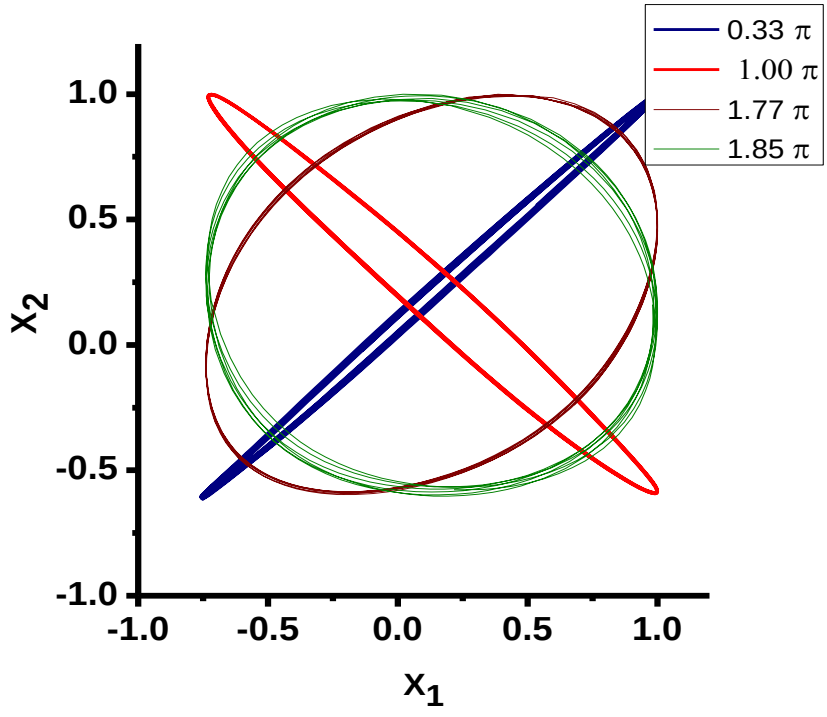

Figure 10.6. B) Relative phase control in state space. Optomechanical control of mechanical coupling phase. oscillators' relative phase can be controlled arbitrarily.

10.6 Synchronization of an array of optomechanical systems

The general principles described here for optomechanical synchronization can be extended to two important problems: a) arrays of micro-mechanical systems coupled through radiation forces b) optomechanical resonators/filters below oscillation threshold. Optomechanical synchronization can be extended for a large array of oscillators by identifying the similarity with a generalized Vander-Pol Duffing oscillator with a saturable gain and a non-linear frequency pulling term[31], as follows:

$$\ddot{x} + 2(\Gamma_m - \Gamma_{om}(x))\dot{x} + (\Omega_m^2 + \Omega_{om}^2(x))x = \chi \tag{6}$$

where $\Gamma_{om}(x) = A\Gamma|\mu|^2\Delta \Big/ \left(\Delta^2 + \frac{\Gamma^2}{4}\right)^2$ is the optomechanical gain , $\Omega_{om}^2(x) = A|\mu|^2\Delta \Big/ \left(\Delta^2 + \frac{\Gamma^2}{4}\right)$ is the non-linear frequency shift induced by radiation pressure, A= $2g^2/\omega m$ and χ the white-noise Langevin function representing the noise sources[28]. Prior theoretical work in non-linear synchronization has shown frequency pulling in nonlinear oscillators assuming a vander-pol like behavior described above[29] as well as the case of pulse coupled oscillators. It was further shown that synchronized oscillators' power scales with N^2 while the noise scales with N^{-2} which may simultaneously enable high power and low noise optomechanical oscillators[32].

10.7 Conclusion

The ability to control the strength, phase and frequency content of mechanical coupling between micro-mechanical structures can enable a new level of control over MEMS structures. The ability of micro-photonics to control the optical modes via electro-optic, thermo-optic means can now be

extended to switch, filter and phase shift the mechanical coupling of MEMS oscillators. Using optically mediated mechanical coupling will allow for coupling mechanical structures spread over a wide region only limited by optical waveguide/fiber losses. Optically mediated mechanical coupling will also remove the restrictions of neighborhood while creating 1D/2D/3D mechanical oscillator arrays. By enabling long range, directional and controllable mechanical coupling; synchronized optomechanical systems may enable a new class of devices in sensing, and signal processing & meso-scale quantum optomechanics.

REFERENCES

1. S. Strogatz, Sync: The Emerging Science of Spontaneous Order (Hyperion, New York, 2003).

2. Buck, J. & Buck, E. Mechanism of rhythmic synchronous flashing of fireflies. Science 159, 1319–1327 (1968)

3. C. S. Peskin, Mathematical Aspects of Heart Physiology (Courant Institute of Mathematical Sciences, New York University, New York, 1975);

4. Kaka, S. et al. Mutual phase-locking of microwave spin torque nano-oscillators. Nature 437, 389–392 (2005).

5. A. Ruotolo, et al Phase-locking of magnetic vortices mediated by antivortices, Nat. Nanotechnol. 4, 528 (2009).

6. Seung-Bo Shim, Matthias Imboden, and Pritiraj Mohanty , "Synchronized Oscillation in Coupled Nanomechanical Oscillators", (6 April 2007) Science 316 (5821), 95.

7. K. L. Ekinci and M. L. Roukes, "Nanoelectromechanical systems", Rev. Sci. Instrum. 76, 061101 (2005); H. G. Craighead, "Nanoelectromechanical systems," Science 290(5496), 1532-1535 (2000).

8. M. K. Zalalutdinov et al, "Two-dimensional array of coupled nanomechanical resonators"Appl. Phys. Lett. 88, 143504 (2006); D. Weinstein, et al, "Mechanical coupling of 2D resonator arrays for MEMS filter applications," IEEE Frequency Control Symposium, Geneva, Switzerland, May 29 - June 1, 2007, pp. 1362-1365.

9. P. A. Truitt, J. B. Hertzberg, C. C. Huang,, Kamil L. Ekinci, and, K.C. Schwab, Efficient and Sensitive Capacitive Readout of Nanomechanical Resonator Arrays, Nano Letters 2007 7 (1), 120-126

10. C. Nguyen: "MEMS Technology for Timing and Frequency Control," IEEE Trans. Ultrason., Ferroelect., Freq. Contr., vol. 54, no. 2,

pp. 251–270, Feb. 2007

11. K.C. Schwab and M. L. Rourkes, Physics Today 58, 7, 36 (2005).

12. A.D. O'Connell, M. Hofheinz, M. Ansmann, R.C. Bialczak, M. Lenander, E. Lucero, M. Neeley, D. Sank, H. Wang, M. Weides, J. Wenner, J.M. Martinis, A.N. Cleland "Quantum ground state and single-phonon control of a mechanical resonator.", Nature 464, 697-703 (2010).

13. Rocheleau, T. et al. Preparation and detection of a mechanical resonator near the ground state of motion. Nature 463, 72–75 (2010)
14. J. D. Jost, J. P. Home, J. M. Amini, D. Hanneke, R. Ozeri, C. Langer, J. J. Bollinger, D. Leibfried , D. J. Wineland, "Entangled mechanical oscillators", Nature 459, 683-685 (4 June 2009)

15. Kippenberg, T. J. & Vahala, K. J. Cavity optomechanics: back-action at the mesoscale. Science 321, 1172–1176

16. T. Carmon, H. Rokhsari, L. Yang, T. J. Kippenberg, K. J. Vahala, Temporal Behavior of Radiation-Pressure-Induced Vibrations of an Optical Microcavity Phonon Mode , Phys. Rev. Lett. 94, 223902 (2005)

17. M. L. Povinelli, J.M. Johnson,M. Loncar, M. Ibanescu, E. J. Smythe, F. Capasso, and J. D. Joannopoulos, "High-Q enhancement of attractive and repulsive optical forces between coupled whispering-gallery-mode resonators," Optics Express 13(20), 8286-8295 (2005).

18. P.T. Rakich, M. A. Popovic, M. Soljacic, E. P. Ippen. "Trapping, corralling and spectral bonding of optical resonances through optically induced potentials", Nature Photonics 1 (11), 2007, p.658;

19. M. Eichenfeld, C. Michael, R. Perahia, and O. Painter, "Actuation of Micro-Optomechanical Systems Via Cavity-Enhanced Optical Dipole Forces," Nature Photonics 1(7), 416 (2007).

20. Mo Li , W. Pernice, C. Xiong, T. Baehr-Jones, M. Hochberg, H. Tang , "Harnessing optical forces in integrated photonic circuits.", Nature ,

456, 480(2008)

21. Wiederhecker, G.S., Chen, L., Gondarenko, A. and Lipson, M., Controlling photonic structures using optical forces, Nature

22. Mancini, S., et al, Entangling macroscopic oscillators exploiting radiation pressure. Phys. Rev. Lett. 88, 120401 (2002); Santamore, D. H., et al, Quantum nondemolition measurements of Fock states of mesoscopic mechanical oscillators. Phys. Rev. B 70, 144301 (2004); Vitali, D. et al. Optomechanical entanglement between a movable mirror and a cavity field. Phys. Rev. Lett. 98, 030405 (2007); Giovannetti, V., Mancini, S. & Tombesi, P. Radiation pressure induced Einstein–Podolsky–Rosen paradox. Europhys. Lett. 54, 559–565 (2001)

23. Marshall, W., Simon, C., Penrose, R. & Bouwmeester, D. Towards quantum superpositions of a mirror. Phys. Rev. Lett. 91, 130401

24. S. Manipatruni, et al, "High speed carrier injection 18 Gb/s silicon micro-ring electro-optic modulator," IEEE Proceedings of Lasers and Electro-Optics Society, 537–538 (2007); P. Dong, et al, Phys. Rev. Lett. 100, 033904 (2008); V. R. Almeida, et al, "All-optical control of light on a silicon chip," Nature 431, 1081-1084 (2004).

25. K. J. Vahala, "Optical Microcavities", Nature 424, 839-846

26. Q. Lin, J. Rosenberg, D. Chang, R. Camacho, M. Eichenfield, K. J. Vahala, and O. Painter, "Coherent mixing of mechanical excitations in nano-optomechanical structures," Nature Photonics, vol. 4, pg. 236-244, April 2010

27. M. Lipson, "Guiding, Modulating, and Emitting Light on Silicon -- Challenges and Opportunities". Journal of Lightwave Technology 23: 4222–4238. (2005).

28. Kubo, R. The fluctuation-dissipation theorem. Rep. Prog. Phys. 29, 255–-284 (1966).

29. M. C. Cross, A. Zumedieck, A. Lifshitz, J. L. Rogers, Phys. Rev. Lett. 93, 224101 (2004).

30. G. S. Wiederhecker, S. Manipatruni, and M. Lipson, "Giant optomechanical tuning of optical cavities," in Conference on Lasers and Electro-Optics/International Quantum Electronics Conference, OSA Technical Digest (CD) (Optical Society of America, 2010), paper CThJ6.

31. A. E. Kaplan, "Single-particle motional oscillator powered by laser," Opt. Express 17, 10035-10043 (2009) ; I. S. Grudinin, H. Lee, O. Painter, and K. J. Vahala, Phys. Rev. Lett. 104, 083901 (2010).

32. A. Pikovsky, M. Rosenblum, and J. Kurths, Synchronization: A Universal Concept in Nonlinear Science (Cambridge University Press, Cambridge, 2001); T. V. Duzer and C. W. Turner, Superconductive Devices and Circuits (Prentice-Hall, Upper Saddle River, NJ, 1999).

33. Feng, X. L., White, C. J., Hajimiri, A. & Roukes, M. L. A self-sustaining ultrahigh-frequency nanoelectromechanical oscillator. Nature Nanotech. 3, 342–346 (2008); M. Hossein-Zadeh, H. Rokhsari, A. Hajimiri, and K. J. Vahala, Phys. Rev. A 74, 023813 (2006).